

Department of Physics and Astronomy

University of Heidelberg

Master thesis

in Physics

submitted by

Fabrizio Napolitano

born in Rome (Italy)

2016

Optimized identification of hadronic W , Z , Higgs
bosons and top quark decays through novel jet mass
observables with the ATLAS detector

This Master thesis has been carried out by

Fabrizio Napolitano

at the

Kirchhoff Institut für Physik

under the supervision of

Priv.-Doz. Oleg Brandt

Abstract:

This thesis presents the development of a new technique for the jet mass reconstruction with the ATLAS detector, designed for an improvement of the resolution at very high transverse momenta. The track-assisted mass, m^{TA} , is a mass variable able to achieve a better resolution of the jet mass measurement; it combines the information coming from the tracker system and the calorimeter on a jet-by-jet basis. The track-assisted mass for the sub-jets, m^{TAS} is the variable developed and presented in this thesis. It combines the information of the two sub-detectors using substructure technique. The results and achievements of this variable are presented and compared to the traditional calorimeter-based jet mass definition.

Zusammenfassung:

Diese Masterarbeit stellt die Entwicklung einer neuen Technik zur verbesserten Rekonstruktion der Jet-Masse bei extrem hohen Longitudinalimpulsen mit dem ATLAS Detektor vor. Die bereits entwickelte spurassistierte Masse m^{TA} ist eine neue Variable, die zu einer Verbesserung der Auflösung führt; sie kombiniert für jeden Jet die Informationen der Spurdetektorsysteme und der Kalorimetersysteme. In dieser Masterarbeit wird die Variable m^{TAS} , die spurassistierte Subjet-Masse, entwickelt. Sie kombiniert die Informationen der zwei genannten Subdetektoren mit Substruktur-Techniken für Jets. Die Ergebnisse dieser neuen Variable werden in dieser Arbeit präsentiert und mit der traditionellen Definition der Kalorimetermasse verglichen.

*Beauty is truth, truth beauty, - that is all
Ye know on earth, and all ye need to know.*

Dilige et quod vis fac
Per Martina.

Preface

This thesis “Optimized identification of hadronic W , Z , Higgs bosons and top quark decays through novel jet mass observables with the ATLAS detector”, has as a basis an intensive and exciting research period from November 2015 to October 2016 which I engaged with the ATLAS group of the Kirchhoff Institut für Physik in Heidelberg, and which included few conferences and an actual detector operation experience as Run Control in summer during data taking period. It concerns the development of new techniques for a more precise measurement of one of the most powerful observables used for physical searches, the jet mass.

The research and the purposes were challenging, but conducting scientifically a series of studies and investigations has allowed to understand the main issues and, after what I would call very formative failures, find the key points which are presented here.

I would hence like to thank a series of people who helped me during this work providing their input, comments, suggestions and support: first of all my supervisor Oleg Brant for the excellent guidance, the contagious excitement for research, and the almost 24h/7 disponibility to answer my queries; the team comprised of Sascha Dreyer, Daniel Narrias Villar, Merve Sahinsoy, Stanislav Suchek and Philipp Kühnl for the availability and help; all the people of the ATLAS KIP which were always ready for any kind of help and the finally the researcher with whom I collaborated from the Jet Substructure and jet-by-jet tagging ATLAS group, in particular Benjamin Nachman from Lawrence Berkeley National Laboratory, Nurfikri Bin Norjoharuddeen and Michael Nelson from Oxford.

Last but not least, I would like to thank my family for the unconditional support, patience and for always believing in me.

Contents

1	Theoretical Background	1
1.1	The Standard Model	1
1.2	Fundamental Particles and Forces	1
1.3	Gauge Symmetries and Interactions	3
1.3.1	Gauge Theories	5
1.3.2	Quantum Chromodynamics (QCD)	6
1.3.3	Electroweak Symmetry Breaking	7
1.4	Beyond the SM: W' , Z' Bosons and Extra Dimensions	9
1.4.1	W' -boson	9
1.4.2	Z' -boson	10
1.4.3	Extra Dimensions and the Graviton	11
2	The ATLAS Experiment at the LHC	13
2.1	The Large Hadron Collider	13
2.2	The ATLAS Experiment	14
2.2.1	Magnets	16
2.2.2	Inner Detector	17
2.2.3	Calorimeters	19
2.2.4	Muon Spectrometer	24
2.2.5	Trigger System	25
2.2.6	Luminosity Measurement	26
3	Monte Carlo Simulation	28
3.1	Event Generation	28
3.2	Detector Simulation	28
3.2.1	MC Sample	29

4	Jet Reconstruction	31
4.1	Jet Phenomenology	31
4.1.1	Parton Showering	31
4.1.2	Hadronization	32
4.1.3	Jet Reconstruction	33
4.2	Basics of Calibration and Uncertainties	36
4.2.1	Responses Jet Energy Scale and Resolution	36
4.2.2	Calibration	36
4.2.3	Uncertainties	38
4.3	Jets in the <i>Boosted</i> Regime	39
4.3.1	Large- R jets	40
4.3.2	Pile-Up and Underlying Event	41
4.4	Substructure: Grooming Techniques	41
4.4.1	Trimming	42
5	Optimization of Large-R Jet Mass Reconstruction	44
5.1	Calorimeter Mass	44
5.2	Track Mass	44
5.3	Performance Figure of Merit (FoM)	46
5.3.1	Gaussian Fit	46
5.3.2	InterQuantile-Range	48
5.4	Track-Assisted Mass (m^{TA})	48
5.4.1	Advantages and Limitation of m^{TA}	50
5.5	The Track-Assisted Sub-jet Mass (m^{TAS})	53
5.5.1	Observable Definition: Inputs	54
5.5.2	Observable Definition: Procedure	55
5.5.3	Performance in $W \rightarrow q'\bar{q}$ Decays	56
5.5.4	Performance in $t \rightarrow q'\bar{q}b$ Decays	57
5.5.5	Performance in $h \rightarrow b\bar{b}$ Decays	57
5.5.6	Performance in QCD Multijet Events	58
5.5.7	Performance in Massive $\tilde{W} \rightarrow q'\bar{q}$ Decays with $m_{\tilde{W}} = m_t$	59
5.6	Other Stability Quantifiers	59
5.7	Sub-jet Calibration	60
5.7.1	Preliminary Studies on Sub-jet Calibration	61
5.7.2	Limitation of m^{TAS}	63
5.7.3	Alternative Observable Definitions	64

5.8	Combined Track and Calorimeter Mass	66
5.8.1	Combination $m^{TA} - m^{calo}$	67
5.8.2	Combination $m^{TAS} - m^{calo}$	67
5.8.3	Performance in $W \rightarrow q'\bar{q}$ Decays	69
5.8.4	Performance in $t \rightarrow q'\bar{q}b$ Decays	69
5.8.5	Performance in $h \rightarrow b\bar{b}$ Decays	70
6	Conclusion and Outlook	72
6.1	Conclusion	72
6.2	Outlook	73
6.2.1	Calibration	73
6.2.2	Uncertainties	73
	Bibliography	75
A	List of Tables and Figures	79
A.1	List of Figures	79
A.2	List of Tables	80
B	ATLAS Detector: Further Details	81
B.1	Muon subdetectors	81
B.1.1	RPC	81
B.1.2	TGC	81
B.1.3	MDT	81
B.1.4	CSC	82
B.2	L1	82
B.3	HLT	82
B.4	Luminosity Measurement	83
C	Parton Shower and Hadronization Details	84
C.1	Parton Shower	84
C.2	Hadronization	86
D	Topo-Clustering and Local Calibration Weighting	88
E	Pile-Up and Underlying Event	90
F	Additional Grooming Techniques	92
F.1	Split-Filtering	92
F.2	Pruning	93

G	Limitation of the m^{TAS}	94
H	Jet Mass Observable Distribution	95
H.1	m^{TAS} distributions, boosted W/Z	105
H.2	m^{TAS} distributions, boosted tops	117
H.3	m^{TAS} distributions, boosted higgs	128
H.4	m_{TAS}^{comb} response distributions, boosted W/Z	139
H.5	m_{TAS}^{comb} response distributions, boosted tops	142
H.6	m_{TAS}^{comb} response distributions, Higgs	145
I	Erklärung:	148

1. Theoretical Background

1.1. The Standard Model

The Standard Model of particle physics (SM) is a quantum field theory which describes the behavior of particles. It was developed throughout the last 50 years to model the phenomena that were discovered experimentally those years. The first step was the formulation of the electroweak theory in 1961 from Sheldon Glashow, in which he managed to combine the electromagnetic and the weak force. Years later, in 1967, Steven Weinberg and Abdus Salam incorporated the Higgs mechanism in the electroweak theory. The SM acquired then its modern form in the early '70s, when the theory was unified with the strong interaction. Its main predictions were the discovery of the neutral current caused by Z boson exchange in 1973, which led to the Nobel Prize in Physics for Glashow, Salam and Weinberg in 1979 and the discovery of the W^\pm and the Z in 1983. After the discovery of the Higgs boson in 2012, which was the last missing piece of the SM, the theory is now complete.

Although being one of the most successful models in the history of science, the SM leaves some questions open, but overall the theory provides a good starting point for the physical processes in particle physics so far understood.

1.2. Fundamental Particles and Forces

The SM is a relativistic quantum field theory which describes the strong, weak and electromagnetic interactions (which are all the known forces with the exception of gravity). It tells that all the matter is made out of bosons, which are the mediators of interactions, and fermions, with their corresponding anti-particle (in some cases the two are the same). Fermions are elementary particles with half integer spin and obey the Fermi-Dirac statistics, while bosons have integer spin and obey the Bose-Einstein statistic. Those particles are summarized in Figure 1.1.

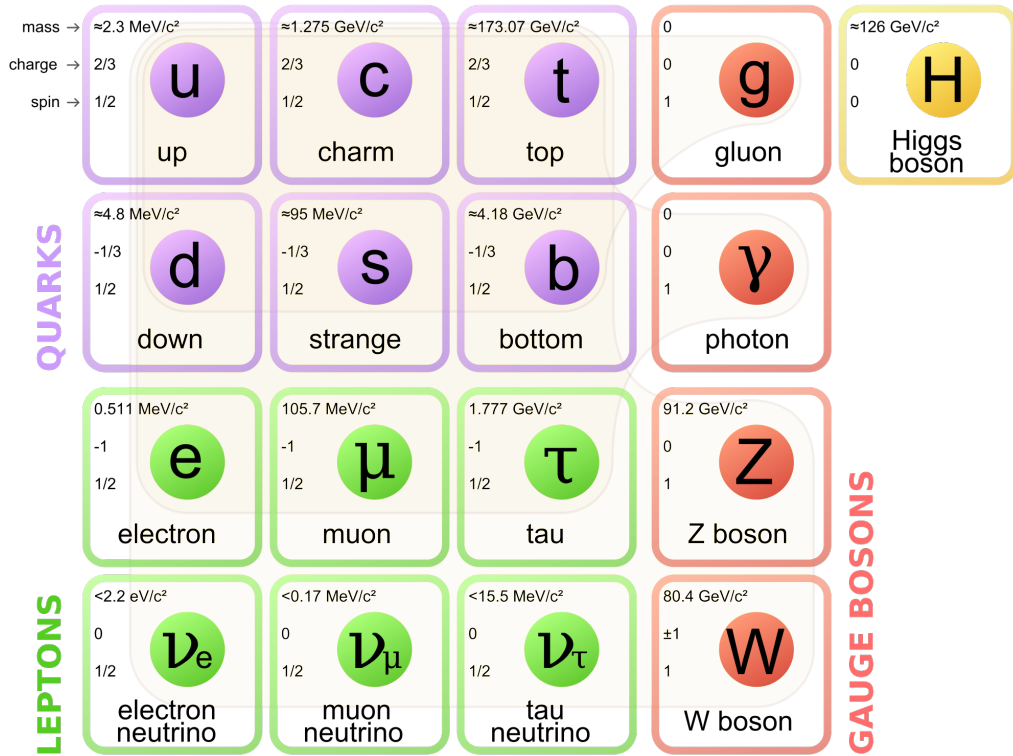


Figure 1.1: Particles in the Standard Model

Bosons

Five bosons are considered in the SM. Four of them are so called *gauge bosons* with spin 1 which act as carriers of the strong, weak and electromagnetic forces. The gauge bosons are described below:

- The photon (γ). It is the mediator of the electromagnetic force. It interacts with all the particles which have electric charge different from zero. It has no electric charge and no mass. As a consequence of the latter, the electromagnetic interaction is a long range interaction. It was the first one to be discovered.
- The two W^\pm bosons and the Z boson. They mediate the weak interaction. Both the W and the Z bosons have large mass with respect to most of the other particles (80.385 ± 0.015 GeV [1] and 91.1876 ± 0.0021 GeV [1] correspondingly). As a consequence, the weak interaction is a short range interaction. The W^\pm have also an electromagnetic charge of ± 1 . The W^\pm and Z bosons interact not only with quarks and leptons, but also with themselves.
- The gluon (g). It mediates the strong interaction. Gluons are mass-less and have no electric charge, carry color charge and can interact with all fermions

carrying color charge and also with other gluons. Eight type of gluons exist with different color charge combinations.

The fifth boson is the Higgs boson. It has a mass of 125.7 ± 0.4 GeV [1], zero electric charge and spin (first fundamental scalar particle to be discovered and it gives mass to the other elementary particles); it results from the spontaneous electroweak symmetry breaking, discussed further in Section 1.3.3. Its discovery was announced in 2012.

Fermions

Fermions are the fundamental building blocks of the visible matter. They are divided in two different types: quarks and leptons, both having spin of $1/2$. They are further divided into three generations with increasing masses and decreasing lifetimes (as again shown in 1.1), while keeping the other properties the same.

- Leptons are either electrically charged and sensitive to weak and electromagnetic interactions (e^\pm , μ^\pm and τ^\pm) or electrically neutral and sensitive to weak interaction only ($\bar{\nu}_e$, $\bar{\nu}_\mu$ and $\bar{\nu}_\tau$). The charged lepton masses are $0.510998928 \pm 0.000000011$ MeV (e), $105.6583715 \pm 0.00000035$ MeV (μ) and 1776.82 ± 0.16 MeV (τ) [1]. Neutrino masses are assigned to be zero in the SM, but experimental observations of neutrino oscillation show that the neutrinos have a non-zero mass.
- Quarks are subdivided again in *up-type* and *down-type*, which differ in electric charge: $2/3$ and $-1/3$ correspondingly, while anti-quarks have opposite electric charge. Their masses are very different from generation to generation: $2.3_{-0.5}^{+0.7}$ MeV (up), 1.275 ± 0.025 GeV (charm) and $173.21 \pm 0.51(\text{stat}) \pm 0.71(\text{syst})$ GeV (top) for the *up-type* quarks and $4.8_{-0.3}^{+0.5}$ MeV (down) to 95 ± 5 MeV (strange) to 4.18 ± 0.03 GeV (bottom) for the *down-type* quarks [1].

1.3. Gauge Symmetries and Interactions

In the SM the interaction between particles originates from the invariance of the Lagrangian of the free fermions with respect to local gauge symmetries.

Electromagnetism

If we consider as a simple example a free electron, its Lagrangian is given by:

$$\mathcal{L} = i\bar{\psi}\gamma_\mu\partial^\mu\psi - m\bar{\psi}\psi$$

where ψ is the spinor field, a 4-component objects, which is defined by means of the γ -matrices. The γ -matrices fulfill the anti-commutation relation $\{\gamma_\mu, \gamma_\nu\} = 2g_{\mu,\nu}$. In the Weyl representation (sometimes called chiral) they are defined by the Pauli matrices:

$$\gamma_0 = \begin{pmatrix} 0 & \mathbb{1}_2 \\ \mathbb{1}_2 & 0 \end{pmatrix} \quad \gamma_i = \begin{pmatrix} 0 & \sigma^i \\ -\sigma^i & 0 \end{pmatrix}$$

The adjoint spinor $\bar{\psi}$ is defined as $\bar{\psi} = \psi^\dagger\gamma^0$. This Lagrangian is invariant under the constant phase transformation:

$$\psi \rightarrow \psi' = e^{i\alpha}\psi, \quad \bar{\psi} \rightarrow \bar{\psi}' = e^{-i\alpha}\bar{\psi}$$

This kind of symmetry is referred to global “gauge” U(1) symmetry. If we assume a symmetry transformation where phase α is no longer constant, but instead is $\alpha(x)$, i.e.

$$\psi \rightarrow \psi' = e^{i\alpha(x)}\psi$$

the Lagrangian is no longer invariant. In fact, there is an additional derivative term:

$$\partial_\mu\psi \rightarrow e^{i\alpha(x)}\partial_\mu\psi + e^{i\alpha(x)}\psi\partial_\mu\alpha(x)$$

To restore the invariance of the Lagrangian under local transformations, we need to use a special derivative which transforms like the field ψ . Let’s call this D_μ such that:

$$D_\mu\psi \rightarrow e^{i\alpha(x)}D_\mu\psi$$

The way to restore the invariance of the Lagrange is to introduce another field, which has a gauge transformation like the electromagnetic four-vector potential, $A^\mu = (\phi, \vec{A})$ where ϕ and \vec{A} are the scalar and vector potentials. The transformation is in fact:

$$A^\mu(x) \rightarrow A^\mu(x) - \frac{1}{e}\partial_\mu\alpha(x)$$

with this relation we can now define D_μ :

$$D_\mu = (\partial_\mu + ieA_\mu)\psi$$

It is called “covariant” derivative because the derivated field $D_\mu\psi$ transforms the same way as ψ .

Writing explicitly in the Lagrangian, one obtains:

$$\begin{aligned} \mathcal{L} &= i\bar{\psi}\gamma_\mu D_\mu\psi - m\bar{\psi}\psi \\ &= \bar{\psi}(i\gamma_\mu\partial_\mu - m)\psi + e\bar{\psi}\gamma_\mu A_\mu\psi \end{aligned} \tag{1.1}$$

where the last term describes the coupling of the electron with the electromagnetic field, with coupling constant e . Adding the kinetic term for the gauge field, the Lagrangian reads:

$$\mathcal{L} = \bar{\psi}(i\gamma_\mu\partial_\mu - m)\psi + e\bar{\psi}\gamma_\mu A_\mu\psi - \frac{1}{4}F^{\mu\nu}F_{\mu\nu}$$

where the kinetic term is

$$F^{\mu\nu} = \partial^\mu A^\nu - \partial^\nu A^\mu$$

This is the well known Lagrangian of the Quantum Electrodynamics. We can notice that the mass term for the gauge field, $\frac{1}{2}m^2 A^\mu A_\mu$ breaks the gauge invariance and is then forbidden, making the (photon) gauge field massless.

1.3.1. Gauge Theories

As the SM is a gauge theory, the corresponding gauge invariant Lagrangian should be introduced. The symmetry groups of the SM are $SU(3)_c \times SU(2)_L \times U(1)_Y$, where $SU(n)$ is the group of unitary $n \times n$ matrices with determinant 1. Any $M \in SU(n)$ can be specified by $n^2 - 1$ real generators.

The $SU(3)_c$ group determines the QCD (Quantum Chromodynamics) sector and has 8 generators, which are the eight gluons. The $SU(2)_L \times U(1)_Y$ group determines the electroweak sector and has 3 + 1 generators, which represent the electroweak bosons W^\pm , Z^0 and the photon γ which is massless. However, in a similar manner to the QED considered above, as mass terms are forbidden since they break the symmetry, the resulting generators of the groups are then massless at this stage. The electroweak symmetry breaking is the process which will introduce mass terms and is discussed in details in Section 1.3.3.

Fermion fields in the SM are divided into left and right chiral components, which are treated by the gauge interaction in a different way:

$$\psi_L = \frac{1}{2}(1 - \gamma^5)\psi, \quad \psi_R = \frac{1}{2}(1 + \gamma^5)\psi$$

where γ^5 is defined as $\gamma^5 = i\gamma^0\gamma^1\gamma^2\gamma^3$ and anti-commutes with all the other γ -matrices.

The left-handed fermions are doublets in the $SU(2)_L$ representation and the right-handed fermions are singlets. There are then three fermion doublets and three fermion singlets representing the three generations; moreover, there is no right-handed neutrino and no left-handed anti-neutrino present in the theory. They are represented as:

$$\begin{pmatrix} \nu_e \\ e \end{pmatrix}_L \quad \begin{pmatrix} \nu_\mu \\ \mu \end{pmatrix}_L \quad \begin{pmatrix} \nu_\tau \\ \tau \end{pmatrix}_L, \quad e_R \quad \mu_R \quad \tau_R$$

for the leptons, and

$$\begin{pmatrix} u \\ d' \end{pmatrix}_L \quad \begin{pmatrix} c \\ s' \end{pmatrix}_L \quad \begin{pmatrix} t \\ b' \end{pmatrix}_L, \quad u_R \quad d_R \quad c_R \quad s_R \quad t_R \quad b_R$$

for the quarks. However the primed (') quarks are here weak eigenstates rather than mass eigenstates, being in fact superposition of mass eigenstates. The Cabibbo-Kobayashi-Maskawa (CKM) matrix describes the transition from weak to mass eigenstates:

$$\begin{pmatrix} d' \\ s' \\ b' \end{pmatrix} = V_{CKM} \begin{pmatrix} d \\ s \\ b \end{pmatrix}, \quad V_{CKM} = \begin{pmatrix} V_{ud} & V_{us} & V_{ub} \\ V_{cd} & V_{cs} & V_{cb} \\ V_{td} & V_{ts} & V_{tb} \end{pmatrix} = \begin{pmatrix} 0.974 & 0.255 & 0.004 \\ 0.255 & 0.973 & 0.041 \\ 0.009 & 0.040 & 0.999 \end{pmatrix}$$

In the same way as used in the electromagnetism (Section 1.3.1), one can write the covariant derivative, which will be different for right- and left-handed particles (the right-handed do not participate in the weak interactions):

$$\begin{aligned} D_\mu \psi_L &= \left(\partial_\mu + i \frac{g}{2} W_\mu^i \sigma^i + i \frac{g'}{2} B_\mu \right) \psi_L \\ D_\mu \psi_R &= \left(\partial_\mu + i \frac{g'}{2} B_\mu \right) \psi_R \end{aligned} \tag{1.2}$$

where g and g' are the coupling constants of $SU(2)_L$ and $U(1)_Y$ correspondingly (Y is the weak hypercharge defined via $Q = I_3 + \frac{Y}{2}$ with Q being the electric charge and I_3 third component of the weak isospin) and with B_μ and W_μ^i the gauge fields of the electroweak theory. The Lagrangian of the electroweak theory can then be written as:

$$\mathcal{L}_{EW} = \bar{\psi}_L \gamma^\mu D_\mu \psi_L + \bar{\psi}_R \gamma^\mu D_\mu \psi_R - \frac{1}{4} W_{\mu\nu}^i W_i^{\mu\nu} - \frac{1}{4} B_{\mu\nu} B^{\mu\nu}$$

where the kinetic term $-\frac{1}{4} W_{\mu\nu}^i W_i^{\mu\nu}$ contains a self interaction of the gauge fields arising from the non-abelian structure of the $SU(2)$: $W_{\mu\nu}^i = \partial_\mu W_\nu^i - \partial_\nu W_\mu^i - g \epsilon_{ijk} W_\mu^j W_\nu^k$, (ϵ_{ijk} is the anti-symmetric tensor and also the structure constant of the $SU(2)$).

1.3.2. Quantum Chromodynamics (QCD)

As stated in the previous section, QCD is based on the non-abelian symmetry group $SU(3)_c$, which has eight generators, associated with the gluons, the carriers of the

strong interaction. They carry color and anti-color. The Lagrangian which describes the strong interaction is given by:

$$\mathcal{L}_{QCD} = \bar{\psi}_i (i(\gamma^\mu D_\mu)_{ij} - m\delta_{ij})\psi_j - \frac{1}{4} G_{\mu\nu}^a G_a^{\mu\nu}$$

where, $D_{ij}^\mu = \partial^\mu \delta_{ij} + g_s t_{ij}^a A_a^\mu$, with $i, j = 1, \dots, 3$ being the color indices (red, green and blue), A_a^μ with $a = 1, \dots, 8$ the eight gluon fields, ψ_i the (colored) quark field and t_{ij}^a the generators of SU(3) group. In the Lagrangian, the field strength tensor, $G_{\mu\nu}^a$ is defined as

$$G_{\mu\nu}^a = \partial_\mu A_\nu^a - \partial_\nu A_\mu^a + g_s f^{abc} A_\mu^b A_\nu^c$$

It is important to note again the self-interaction term arising, as in the electroweak case, from the non abelianity (here f^{abc} is the structure constant).

An important difference with the electroweak theory is that no free quarks have been observed yet, leading to the assumption that bound states only exist as color singlet states. Inside the protons and neutrons, quarks and gluons act as free-like particles. The first effect is known as *confinement*, the second one as *asymptotic freedom* and both are described in terms of running coupling constant $\alpha_S = \frac{g_S^2}{4\pi}$. The running coupling constant obeys the renormalization group equation:

$$\alpha_S = \frac{\alpha(\mu_R^2)}{1 - \beta_0 \alpha(\mu_R^2) \ln(Q^2/\mu_R^2)}$$

where μ_R is an unphysical renormalization scale, Q is the momentum transfer of the process and β_0 is a constant known as 1-loop beta function and depends on the number of quarks N_f : $\beta_0 = (2N_q - 33)/12\pi$. β_0 is therefore negative, meaning that at higher energy scale the theory is weakly coupled. The dependence of α_S as a function of Q is shown in Figure 1.2. The behavior of the coupling constant leads two regimes: as long as the coupling is sufficiently small ($\mathcal{O}(0.1)$), perturbation theory can be used, but if the coupling becomes larger at lower momentum transfer, phenomenological models are used to describe quarks and gluons.

1.3.3. Electroweak Symmetry Breaking

The electroweak symmetry breaking (sometimes just ESB or Brout-Englert-Higgs mechanism) is the way by how the massless weak bosons and the fermions acquire masses. In fact, simply adding a mass term to the Lagrangian, i.e. something like $m\bar{\psi}\psi = m(\bar{\psi}_L\psi_R + \bar{\psi}_R\psi_L)$ will violate the gauge invariance of the SU(2)_L group. Instead, if we introduce an additional scalar field, ϕ , as complex scalar SU(2)_L doublet

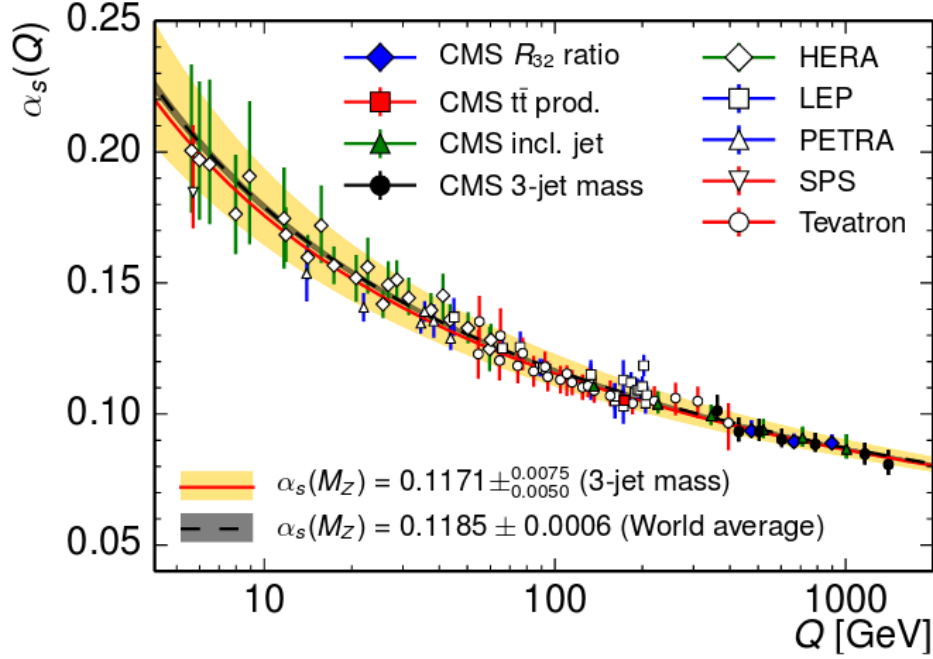


Figure 1.2: Comparison of the $\alpha_s(Q)$ evolution as determined in a three-jet mass CMS analysis with (solid curve with light grey uncertainty band; color version: red curve with yellow uncertainty band) to the world average (dashed curve with dark grey uncertainty band). An overview of measurements of the running of the strong coupling $\alpha_s(Q)$ from electron-positron, electron-proton, and proton-(anti)proton collider experiments is also presented. The results cover a range in values of the scale Q up to 1.4 TeV [13].

and with an ad-hoc choice of the scalar potential, it will give rise to the spontaneous breaking of the $SU(2)_L \times U(1)_Y$ symmetry. Writing down the Lagrangian for the Higgs sector and the potential:

$$\mathcal{L}_H = (D_\mu \phi)^\dagger (D^\mu \phi) - V(\phi), \quad V(\phi) = -\mu^2 \phi^\dagger \phi + \lambda (\phi^\dagger \phi)^2$$

with the usual definition of the covariant derivative, and with $\mu^2, \lambda > 0$.

Now the minimum of the potential is at $|\phi_0| = \sqrt{\frac{\mu^2}{2\lambda}}$, since the potential has the shape of a Mexican Hat or double well. Choosing any particular ground state breaks the symmetry $SU(2)_L \times U(1)_Y$ while the Lagrangian remains invariant. In fact, taking the minimum as

$$\phi = \frac{1}{\sqrt{2}} \begin{pmatrix} 0 \\ \nu \end{pmatrix}$$

with $\nu = \sqrt{\mu^2/\lambda}$ and considering a small perturbation around that,

$$\phi = \frac{1}{\sqrt{2}} \begin{pmatrix} 0 \\ \nu + H \end{pmatrix}$$

Inserting in the Lagrangian of the Higgs sector, mass terms will rise for the Higgs field and, because of the covariant derivative, for the W^\pm and Z^0 , while the photon will stay massless. The weak bosons masses are: $m_W = \frac{gv}{2}$ and $m_Z = \frac{\sqrt{g^2+g'^2}}{2}\nu$. The mass of the Higgs will be $m_H = \sqrt{2\lambda\nu}$.

1.4. Beyond the SM: W' , Z' Bosons and Extra Dimensions

During the research performed which is presented in this thesis, particles of theories beyond the Standard Model, such as W' and Z' were used for performance studies. This section briefly describes these models, since they are not only sources of final states with extreme relativistic regimes, but they are also subject of searches in high energy particle physics, and specifically in ATLAS [4] and CMS experiments [5].

1.4.1. W' -boson

The W' boson is a massive, hypothetical particle of charge ± 1 and spin 1, predicted in several extended gauge models and other extensions of the SM. The Lagrangian describing the interaction of a W'^+ with fermions has the form:

$$\frac{W'^+}{\sqrt{2}} [\bar{u}_i (C_{qij}^R P_R + C_{qij}^L P_L) \gamma^\mu d_j + \bar{\nu}_i (C_{lij}^L P_R + C_{lij}^L P_L)]$$

where u , d , ν and e are SM fermions in the mass eigenstate; $i, j = 1, 2, 3$ are the fermion generations and $P_{R,L}$ are the projection operators. The coefficients C 's are complex dimension-less parameters. This Lagrangian reduces to the SM when $C_q^L = gV_{CKM}$, $C_l^L = g$ and $C_q^R = C_l^R = 0$. On the other hand, the $W'WZ$, $W'W'Z$ and the W' coupling to the Higgs or the Z' are model dependent.

The simplest extension of the electroweak gauge group which includes W' is $SU(2)_1 \times SU(2)_2 \times U(1)$. A generic property of these gauge theories is that they often include the Z' boson.

Other important models are e.g. ‘‘left-right symmetric gauge group’’ $SU(2)_R \times SU(2)_R \times U(1)_{B-L}$, with the SM fermions that couple to the W boson transforming as doublets under $SU(2)_L$, and the other ones transforming as doublets under $SU(2)_R$.

In this model the W' boson couples primarily to right-handed fermions and its coupling to left-handed fermions arises solely due to $W' - W$ mixing.

Constraints to these models can be put because of the $W' - W$ mixing which would shift the SM values of $W - Z$ mass ratio and the couplings of SM W .

There are many more models based on $SU(2)_1 \times SU(2)_2 \times U(1)$ gauge symmetries, and gauge groups that embed the electroweak symmetry, such as $SU(3)_W \times U(1)$ or $SU(4)_W \times U(1)$ also include one or more W' [6].

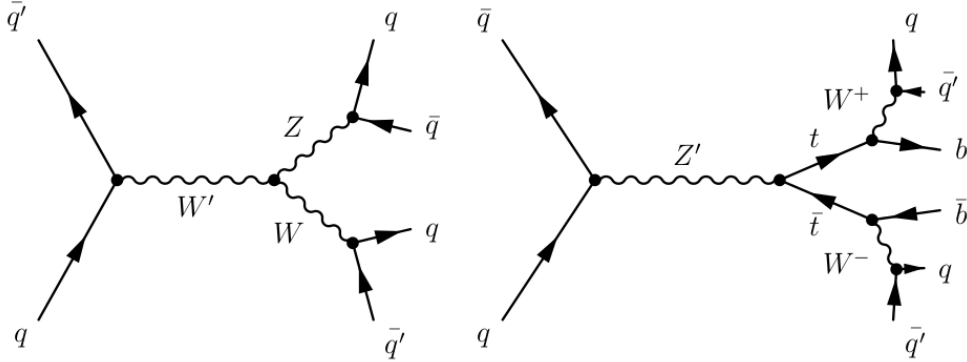


Figure 1.3: Example of Feynman diagrams considered in this thesis, with a W' decaying to a pair of electroweak bosons on the left, and a Z' decaying to a top and an anti-top quark. In both cases the final state considered is the fully hadronic.

1.4.2. Z' -boson

The Z' boson is a massive, hypothetical particle of charge 0 and spin 1, and as the W' , predicted in several extension of the SM.

The coupling of a Z' to fermions is given by these terms in the Lagrangian:

$$Z'_\mu (g_u^L \bar{u}_L \gamma^\mu u_L + g_d^L \bar{d}_L \gamma^\mu d_L + g_u^R \bar{u}_L \gamma^\mu u_R + g_d^R \bar{d}_L \gamma^\mu d_R + \\ + g_\nu^L \bar{\nu}_L \gamma^\mu \nu_L + g_e^L \bar{e}_L \gamma^\mu e_L + g_e^R \bar{e}_L \gamma^\mu e_R)$$

Where u , d , ν and e are SM fermions in the mass eigenstate; $i, j = 1, 2, 3$ are the fermion generations and the coefficients g 's are complex dimension-less parameters. They are promoted to matrices if the coupling of the Z' depends on the fermion generation.

Here the simplest extension of the SM which introduces a Z' boson is a new $U(1)'$ symmetry. Many different charges are possible, even with a free parameter; e.g. the $U(1)_{B-xL}$ has a charge proportional to the baryon number minus x times the lepton

number. In the particular case $x = 0$ or $x \gg 1$ we would have a leptophobic or quak-phobic Z' respectively.

The Z' may also arise from larger groups, as in $SU(2)_2 \times U(1)_Y \times SU(2)'$ or may be embedded in the electroweak group, e.g. in $SU(3)_W \times U(1)$. If the electroweak gauge bosons propagate in extra dimensions, then their *Kaluza-Klein* (KK) excitations include a series of Z' boson pairs. Other main models are E_6 models, *topcolor* and *Little Higgs* [7].

1.4.3. Extra Dimensions and the Graviton

The idea to add additional dimensions was already introduced in the 20's mainly through the work of Kaluza and Klein, in attempt to unifying the forces of nature. Already here, the extra dimensions were supposed to be compactified at a scale close to the Planck scale.

In 1999, Randall and Sundrum found a new possibility using a warped geometry, with a five-dimensional Anti-de Sitter (AdS) space-time

$$ds^2 = e^{-2kr_c\phi} \eta_{\mu\nu} dx^\mu dx^\nu + r_c^2 d\phi^2$$

where k is a scale of the order of Planck scale, x^μ are the usual coordinates for the four-dimensional space, but now $0 < \phi < \pi$ is the coordinate for the additional extra dimension, whose size is set by r_c . Randall and Sundrum showed that this metric is a solution to Einstein's equation in a simple set-up with two 3-branes and appropriate cosmological terms [8].

In the warped dimension, only gravity is assumed to propagate and the origin of the smallness of the electroweak scale versus the Planck scale (*hierarchy*) is explained by the gravitational redshift factor $e^{-2kr_c\phi}$, as also depicted in Figure 1.4. The model predicts a tower of Kaluza Klein graviton states with a TeV scale masses [9], which couples to the standard model particles; the decay of a graviton to two Higgs bosons

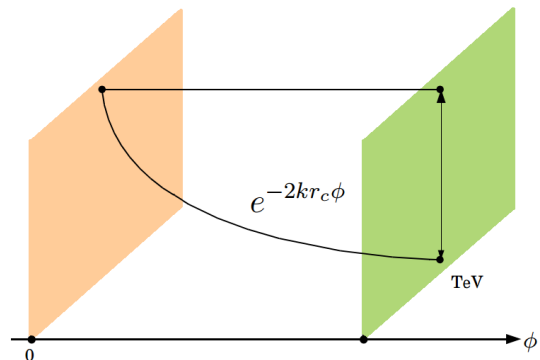


Figure 1.4: Schematics of the RS model: on the left the hidden warped dimension in which the gravity propagates at the Planck scale, on the right the SM 3-brane, where the gravitational redshift factor brings it back to the TeV scale.

is in particular considered in this thesis.

2. The ATLAS Experiment at the LHC

This chapter provides a description of the ATLAS experiment, located at the Large Hadron Collider (LHC). The first section gives an overview of the accelerator and the following ones of the experiment itself. More details can be found in the technical design reports for ATLAS [10] and for LHC [11].

2.1. The Large Hadron Collider

The Large Hadron Collider is the world's most powerful particle accelerator, designed to accelerate protons and heavy ions; it brings protons to a center-of-mass energy \sqrt{s} of 13 TeV, and will reach its maximum operational energy of 14 TeV over the coming years. The maximum peak luminosity delivered to the experiment for Run 2 was $10^{34}\text{cm}^{-2}\text{s}^{-1}$. It was built in the tunnel of the former Large Electron Positron Collider (LEP), located at the European Organization for Nuclear Research (CERN) near Geneva. The tunnel was built between 1984 and 1989, it has a total length of 26.7 km and is located underground at a depth between 45 and 170 m. There are two additional tunnels, linking the LHC with the Super Proton Synchrotron (SPS), which delivers protons at the energy of 450 GeV.

The acceleration chain starts with a bottle of hydrogen: protons are separated from the electrons through an electric field, bringing them to 92 KeV. Throughout a linear accelerator (LINAC) they achieve the energy of 50 MeV and are injected in the Proton Synchrotron BOOSTER, which increases the energy further to 1.8 GeV. Each beam goes then into the Proton Synchrotron (PS), getting a bunch space of 25ns, and then into the SPS. The 450 GeV beams are then delivered to the LHC.

The LHC tunnel consists of eight straight lines connected by section of arcs; the tunnels host the superconducting Nb-Ti magnets cooled down at 1.9K with superfluid helium. The strength of the magnetic field is 8.3 T, needed to achieve the operational energy per beam of 6.5 TeV at Run 2. There are 1232 dipole magnets of 14.3 m length each. The operations of the accelerator started in 2008 with the

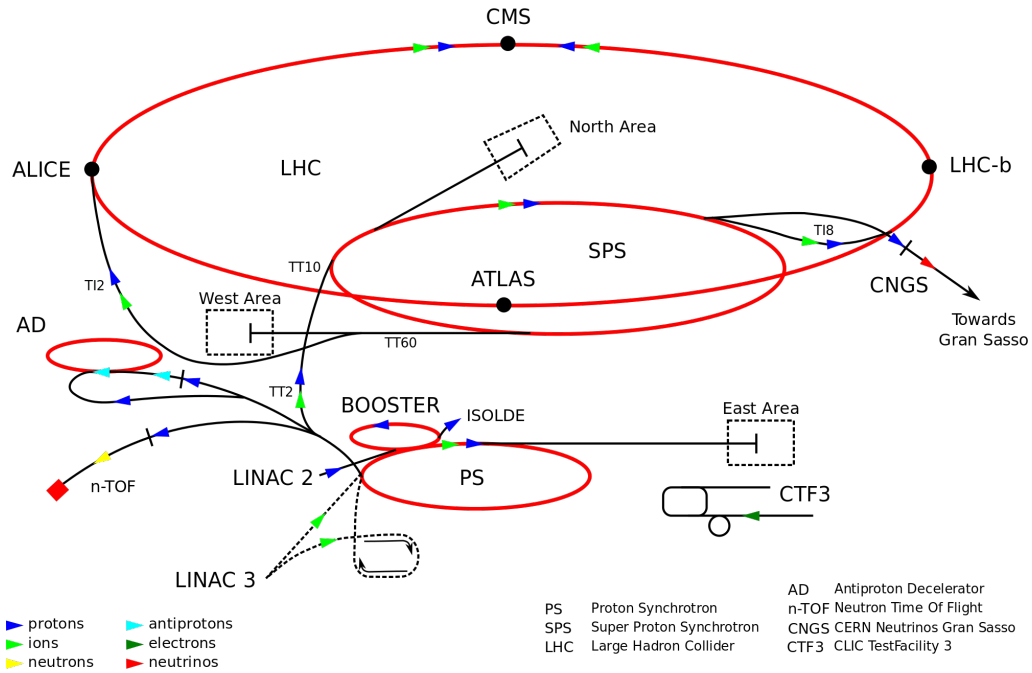


Figure 2.1: Accelerator chain at CERN.

Run 1, but it was interrupted few days later due to a major fault on one electrical connection. It started again after reparations and checks in 2009, operating until 2012 with a yield of 23.3 fb^{-1} . After the long shut-down 1, it was brought again to operational status in 2015, starting then the Run 2. It is currently fully operational; online luminosity is shown in 2.2. There are eight access points to the tunnel, in four of them are located the experiments: ATLAS at point 1, ALICE at point 2, CMS at point 5 and LHCb at point 8. ATLAS and CMS are two general-purpose detectors, designed to be competitive over all the main particle physics research lines; ALICE and LHCb are dedicated experiments, the former optimized for heavy-ions collisions and the latter for precision measurements in the forward region of CP violation and rare B and C hadrons decays.

2.2. The ATLAS Experiment

ATLAS (A Toroidal Apparatus) is a multi-purpose particle detector with nearly 4π coverage in solid angle. A lead/liquid-argon sampling electromagnetic calorimeter is split into barrel ($|\eta| < 1.5$) and end-cap ($1.5 < |\eta| < 3.2$) sections. A steel/scintillating-tile hadronic calorimeter covers the barrel region ($|\eta| < 1.7$) and two end-cap copper/liquid-argon sections extend to higher pseudo-rapidity ($1.5 < |\eta| < 3.2$). Finally, the forward region ($3.1 < |\eta| < 4.9$) is covered by a liquid-argon

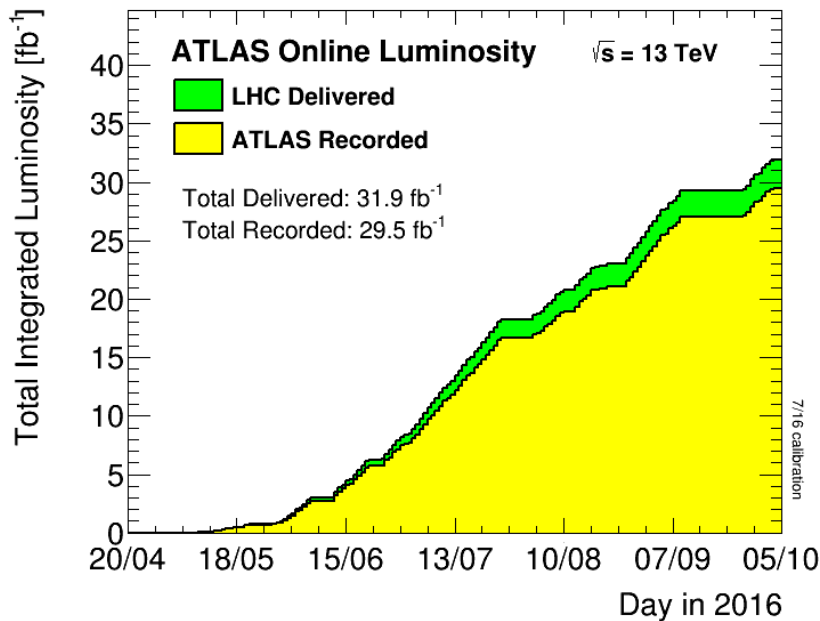


Figure 2.2: Delivered and recorded integrated luminosity as of 5th October 2016 for Run 2 since April 2016. The number of 30 fb^{-1} compares to the 33.2 fb^{-1} produced between 2010 and 2015. The final luminosity for 2016 will be 36 fb^{-1} with an overall data taking efficiency of 92.4%.

calorimeter with Cu (W), absorber in the electromagnetic (hadronic) section. Inside the calorimeters there is a 2 T solenoid that surrounds an inner tracking detector which measures charged particle trajectories covering a pseudo-rapidity range $|\eta| < 2.5$ with pixel and silicon micro-strip detectors (SCT) and additionally which covers the region $|\eta| < 2.0$ with a straw-tube transition radiation tracker (TRT). Outside the calorimeter there is a muon spectrometer: a system of detectors for triggering up to $|\eta| < 2.4$ and precision tracking chambers up to $|\eta| < 2.7$ inside a magnetic field supplied by three large superconducting toroid magnets.

A breakdown of the ATLAS sub-detector performance is shown in Table 2.1.

ATLAS Coordinate System

The Interaction Point (IP) of the proton-proton collisions is the center of a right-handed Cartesian coordinate system; the positive x -axis is pointing towards the center of the LHC ring in direction north-northeast, the positive y -axis points upwards and the z -axis lies in the direction of the beam-pipe, pointing east. The half of the detector on positive values of the z -axis is referred to as “A-side” and the negative one “C-side”. Other important variables often used in particle physics are

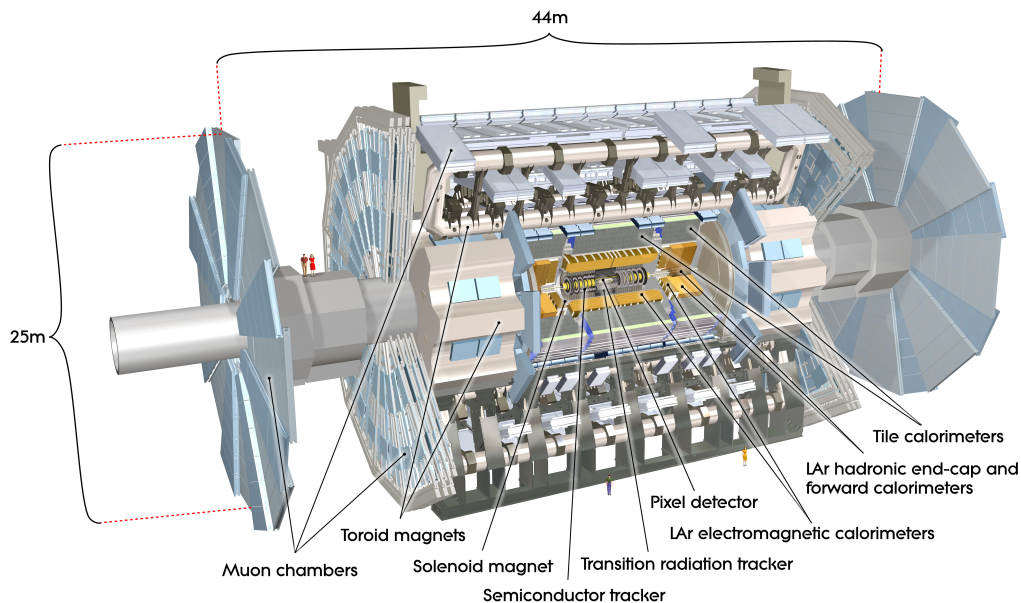


Figure 2.3: Overview of the ATLAS detector.

the azimuthal angle ϕ , measured from the x -axis, and the polar angle θ , measured from the z -axis. The pseudo-rapidity, η is defined as

$$\eta = -\ln \tan \theta/2$$

which is useful since it is invariant under boosts in the z -axis. The distance between two points in the (η, ϕ) space is defined as

$$\Delta R = \sqrt{\Delta\eta^2 + \Delta\phi^2}$$

2.2.1. Magnets

The ATLAS superconducting magnet system is composed of a central solenoid (CS), which provides the inner detector with a 2 T with peak of 2.6 T magnetic field, and three large toroids. Two of them occupy the end-caps of the detector (ECT) and are inserted inside the barrel toroid (BT). They provide magnetic field of a strength of 3.9 and 4.1 T, respectively, to the muon spectrometers. Being the CS in front of the electromagnetic calorimeter, a careful material optimization was required to avoid a reduction of the performance: in fact they share the same vacuum vessel. Moreover, the coil was designed to be as thin as possible. They are made of 20.5 kA aluminium-stabilized Nb-Ti superconductors. All the magnets are cooled down to assure the superconductivity and a forced flow of helium at 4.5 K assure this

condition; in addition the ECT and the BT have cold helium pumps to guarantee appropriate cooling.

2.2.2. Inner Detector

The Inner Detector (ID), also called Tracker, is mainly designed to: reconstruct the trajectories, measure momenta of charged particles with high precision, reconstruct and distinguish the interaction vertices from the secondary vertices of decaying particles. It has a coverage of $|\eta| < 2.5$ and it is fully contained in the CS. To fulfill its task and to cope with the dense environment at the LHC, both from the reconstruction and radiation point of view, detectors with fine granularity were needed, especially near the interaction point. Pixel technologies and silicon micro-strips (SCT) offer these features. The number of layers of these detectors is low, because of the high cost and the material budget; they provide a few number of hits. The Transition Radiation Tracker (TRT), based on gaseous straw tubes, on the other hand, provides a continuous of hits, with less material and at a cheaper cost; it provides hence a complementary and robust detector for the outer part of the ID. An overview of the Inner Detector is given in Figure 2.4 and in Figure 2.5 for the barrel.

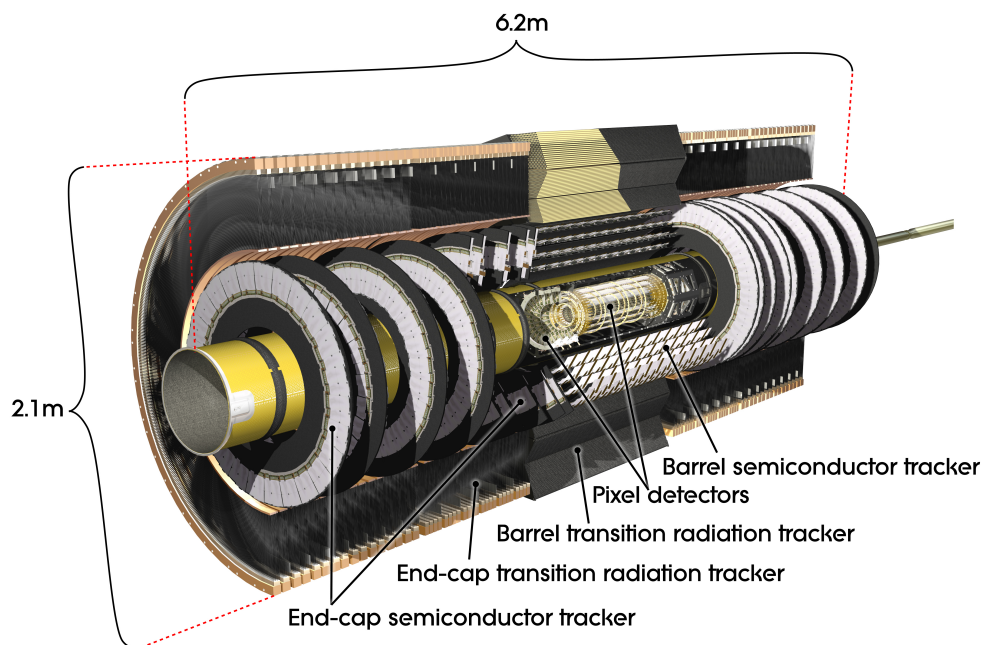


Figure 2.4: The ATLAS Inner Detector and its sub-detectors.

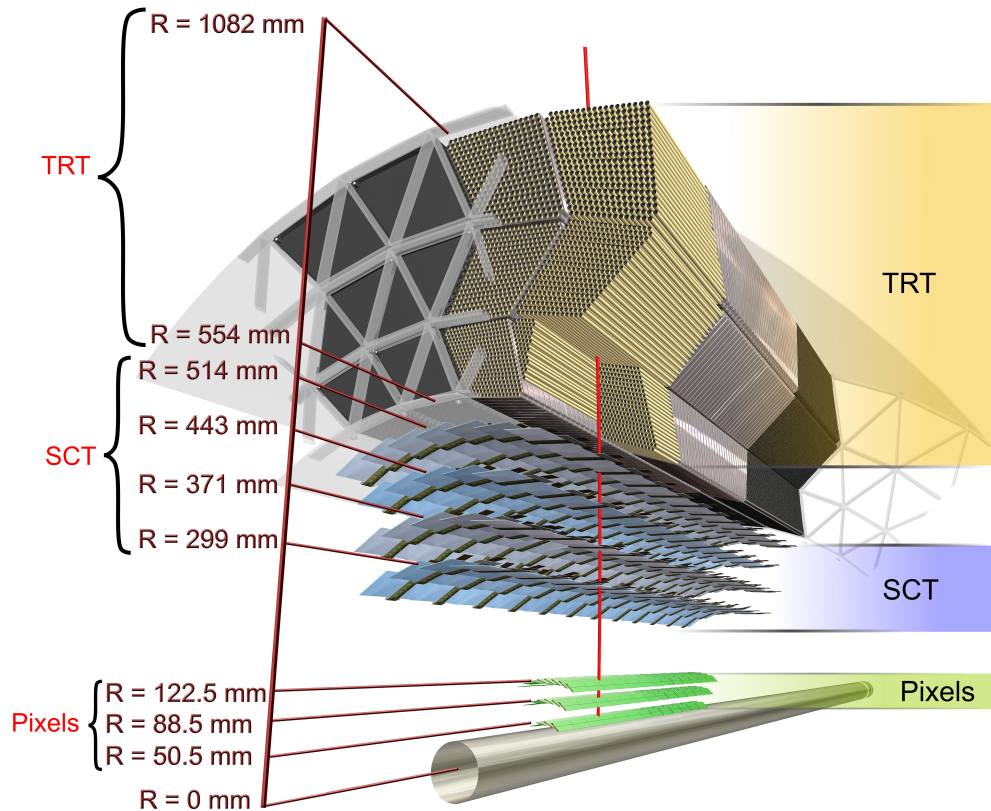


Figure 2.5: The ATLAS Inner Detector barrel view.

Pixel

The Pixel detector is the closest of the ID subsystem to the interaction point. It consists of high-granularity, semiconductor sensors; their area is $50 \times 400 \mu\text{m}^2$ and $50 \times 600 \mu\text{m}^2$ in the front-ends. They are organized in 1744 modules, each containing 47232 pixels. The modules are disposed in three layers in the barrel with radii of 50.5 mm, 88.5 mm, and 122.5 mm and three end-cap disks, distant 495 mm, 580 mm, and 650 mm from the IP. A fourth layer in the barrel, called Insertable B-Layer (IBL) was installed with radius of 25.7mm in the ID during the long shut-down between 2013 and 2015 to fulfill the requirements imposed from the increased luminosity in Run 2. The Pixel detector offers a resolution of $115 \mu\text{m}$ on the z -axis and $10 \mu\text{m}$ in the transverse plane, since on this plane the measurement of the momentum of the charged particle is achieved throughout the reconstruction of the trajectories

bended in the magnetic field. Given the small distance from the IP, the pixels were designed to withstand 10 years of operations and the voltage applied will go from 150 V to 600 V to compensate for the radiation damage to the silicon structure.

Semiconductor Tracker

The Semiconductor tracker (STC) detector is designed to provide eight precision position measurement per track, improving the momentum and vertices reconstruction; it is located just outside the Pixel detector. The STC consists of silicon micro-strips organized in 780 readout strips of 80 μm pitch and arranged in four layers in the barrel with radii of 299 mm, 371 mm, 443 mm and 5541 mm and nine disk layers in the end-cap, at a distance of 853 mm, 934 mm, 1091 mm, 1299 mm, 1399 mm, 1771 mm, 2115 mm, 2505 mm, and 2720 mm on the z -axis.

Transition Radiation Tracker

The Transition Radiation Tracker (TRT) is the outer of the ID systems; its main difference with the previous ones is that it is not based any more on silicon sensors, but on gaseous drift tubes (“Straw Tubes”), a cheap technology which is radiation resistant and provides a large number of hits per single track (typically 30). The barrel region is occupied, in radii from 55 to 108 cm, by 50000 straws; the end-caps, from 64 to 103 cm, by 320000 radial straws organized in 14 wheels. Each Straw tube has a diameter of 4 mm, containing at the center a gold-plated tungsten wire of 31 μm diameter. The gas used is a mixture of 70% Xe, 27%CO₂ and 3%O₂. The wire and walls are subjected to a 1.5 kV potential difference, in order to operate each tube as a proportional-mode counter. The TRT provides a spatial resolution of 120 μm for charged particles with $|\eta| < 2$ and $p_T > 0.5$ GeV, which is worse than the silicon-based tracker, but is compensated through the higher number of hits.

Moreover, the space between the straw tubes is filled with a polymer, designed to create a transition radiation, which is emitted by relativistic charged particles as they traverse a material boundary. The effect depends on γ , and allows particle identification, in particular for the discrimination between pions and electrons.

2.2.3. Calorimeters

Proceeding outwards from the interaction point, after the central solenoid, there is the location of the calorimeters. They are designed to measure the energy and direction of the particles emerging from the interaction, not any more measuring the curvature of tracks like in the ID, but resolving the energy they dissipate within

the detector itself. The electromagnetic calorimeter (EM) is studied to stop and measure energies of particles that interact electromagnetically, primarily photons and electrons. These particles interact with nuclei and electrons, converting photon to electron-positron pairs or producing *bremsstrahlung* photons. The basic unit of distance in the EM calorimeter is the *radiation length* X_0 , defined as the mean distance through which a charged particles loses energy such that it only has $1/e$ of the original amount; number of radiation lengths is shown e.g. in Figure 2.7. The hadronic calorimeter (HAD) is meant to stop and measure hadrons energies. The energy loss is quantified by the *interaction length* λ_I , which is the distance traveled by hadrons before undergoing inelastic collisions with the detector material, usually much larger than the radiation length (up to 30 times more); X_0 and λ_I are expressed in g/cm^2 .

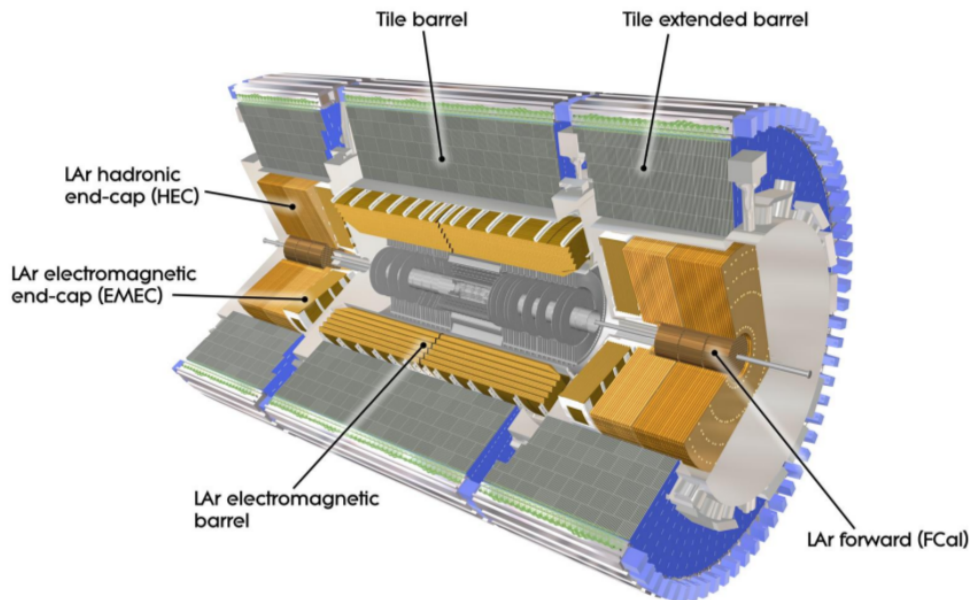


Figure 2.6: ATLAS overview of the calorimeter setup.

Both of them are *sampling* calorimeters, meaning that they are composed of a passive material, which has the purpose of stimulating the production of further particles into a cascade called *shower*, and an active material, which is meant to measure the ionization produced by the particles in the shower. Only neutrinos and Minimally Ionizing Particles (MIP) such as muons pass through the calorimeters almost unaffected. An overview of the ATLAS calorimeter set-up is given in Figure 2.6

Electromagnetic Calorimeter

The electromagnetic calorimeter makes use of liquid Argon (LAr) as active material, chosen because of its uniform nature, stability and radiation-hardness; the temperature of the LAr is between 88.5 K and 88.6 K. As passive material was chosen lead, because it is a cheap material and has a short radiation length of ($X_0 = 0.561$ cm) thus enhancing the containment of the shower inside the given detector geometry. The lead is arranged in accordion sheets, shape chosen to assure the full coverage in ϕ and enable fast signal extraction in the electrodes. The sheets have a thickness of 1.53 mm (1.13 mm) for $|\eta| < 0.8$ ($|\eta| \geq 0.8$) and in the end-caps of 1.7 mm (2.2 mm) for $0.8 < |\eta| < 2.5$ ($|\eta| \geq 2.5$), those differences are introduced to prevent a decrease in the sampling fraction for varying $|\eta|$.

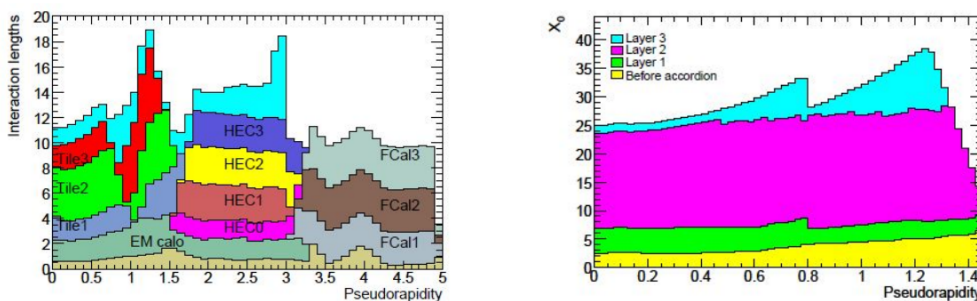


Figure 2.7: The number of interaction lengths for the whole calorimeters (left) and radiation lengths for the EM calorimeter in the barrel region (right).

The electrodes of the readout electronics are arranged in three conductive copper layers insulated with polyamide sheets. The two outer electrodes in the barrel are kept at 2000 V, while the signal is read out from the middle electrode. In the end-caps, the voltages vary by $|\eta|$ between 1000 V and 2500 V.

As particles pass through the calorimeters, they ionize the LAr. A high voltage is applied to the plates enclosing the LAr, causing the electrons to drift to the copper electrodes within a time of approximately 450 ns. The uniformity of the LAr results in a clean triangular signal shape, where the majority of the signal arrives within a short period before decreasing to zero linearly. In order to match the LHC bunch spacing of 25 ns, a signal shaper is applied to the triangular signal.

The EM calorimeter is divided into the electromagnetic barrel (EMB), the electromagnetic end-cap (EMEC) and the electromagnetic pre-sampler.

The EMB has three layers of different granularities and depth, as shown in Figure: 2.8, covering $|\eta| < 1.475$. The first layer has cells of 0.0031×0.098 (η, ϕ) designed

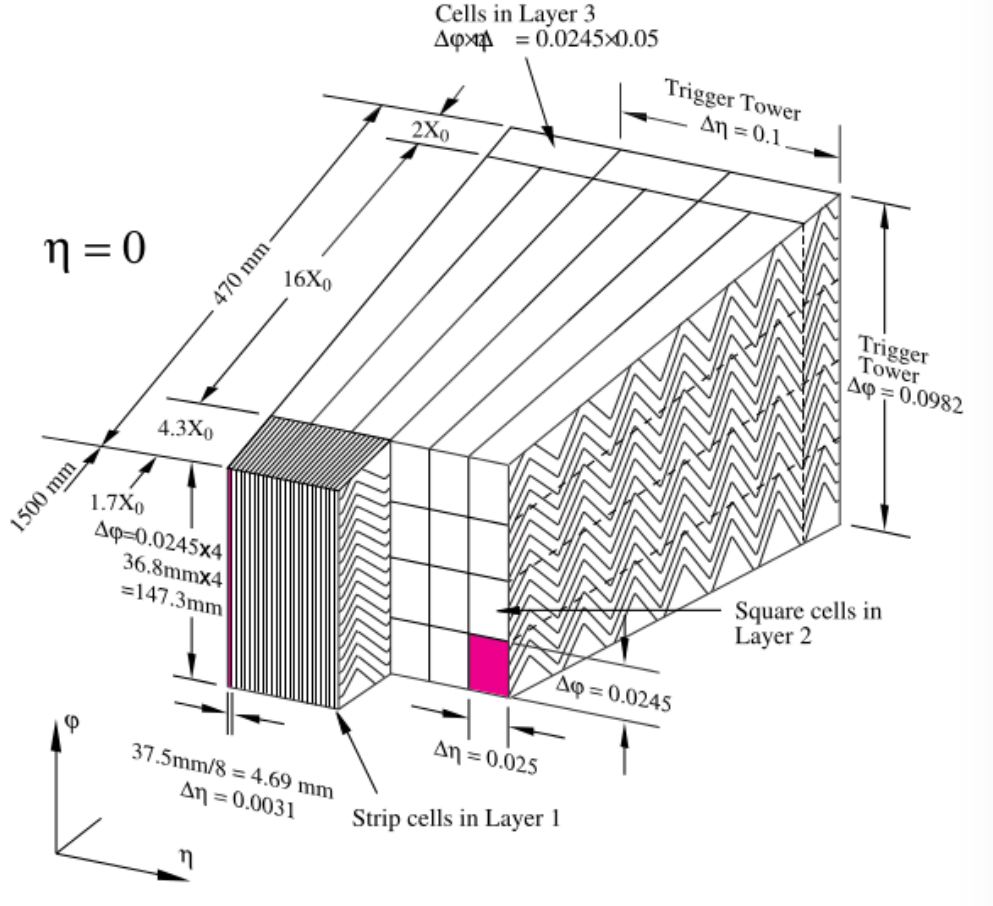


Figure 2.8: Section of the EM calorimeter in the barrel region. The accordion structure is visible on the side; the granularity and depth in radiation lengths is shown.

to help discriminating photons from neutral pions decay. The second layer is the thickest (16 radiation lengths) as intended to collect the most of the shower's energies, but with a much coarse granularity (0.025×0.0245). The third layer is again coarser than the other two in η (0.05×0.0245) and is shorter.

The EMEC is disposed into two wheels of radii 330 mm to 2098 mm in the A- and C-side, covering from 1.375 to 3.2 in $|\eta|$ with the same structure of EMB. The transition region between EMEC and EMB is referred to as *crack region* and contains several radiation lengths of material budget (mainly services to the inner detector).

The EM pre-sampler is meant to correct for the energy loss in the Inner Detector, solenoid and cryostat wall; it is placed only in the barrel region, since there is less material budget in the end-caps. A single thin layer of argon but no lead absorber is placed in front.

Hadronic Calorimeter

The hadronic calorimeters are located just outside the EM calorimeters and are designed to stop and measure the energies of strongly interacting particles. As the EM calorimeter, they are sampling calorimeter, made out of active materials, plastic scintillating tiles (for the barrel and extended barrel shown schematically in Figure 2.9) and LAr (for the hadronic end-caps); the passive material is steel and copper, respectively. The number of interaction lengths varies again throughout the calorimeter from 7 to $16 \lambda_I$. Steel was chosen for its moderate nuclear interaction length of 16.8 cm and its low cost considering the geometrical extension of the calorimeter. The hadronic barrel is known as Tile calorimeter and the hadronic end-cap is called HEC.

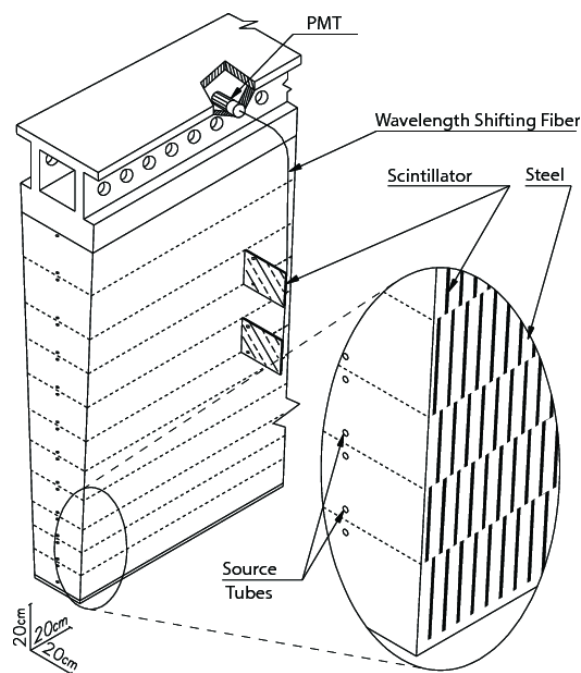


Figure 2.9: Schematic view of a tile module in the ATLAS hadronic Tile calorimeter.

As charged particles from the hadronic shower go through the scintillating tiles, photons are produced in proportion to the amount of energy deposited, which are then collected by means of wavelength shifter fibers and read out through photo multiplier tubes (PMT) to convert the photo-electrons from photoelectric effect into an analog signal. The fibers are grouped together with a supporting girder that is radially oriented to the calorimeter, each subtending a ϕ and η such that a granularity of 0.1×0.1 is achieved for the first two layers, while in the third the granularity in η is 0.2.

The HEC is placed just outside the EMEC, and they share the same detector

technology, LAr as active medium, but copper as passive one rather than lead. It is made out of two wheels, covering $1.5 < |\eta| < 3.2$ with cells of roughly 0.1×0.1 in η, ϕ for $\eta < 2.5$, but 0.2×0.2 for the rest.

Forward Calorimeter

The outermost calorimeters systems are the forward calorimeters (FCAL) which cover pseudo-rapidity ranges from 3.1 to 4.9. They are placed dovetailed between the other calorimeters end-caps, thus providing a coverage of the sub-detectors transition regions. They are made out of three layers, with again LAr as active medium and copper and tungsten for first and the last two, respectively. The inner module is for EM calorimetry and the last two for hadronic measurements. Being close to the beam pipe, it experiences extreme particles flux, requiring special material choices and radiation-hard components. Copper was chosen instead of lead for the EM layer because of a higher heat conductivity, hence dispersing energy and reducing the cooling infrastructure needed, while tungsten was taken because of its very short $\lambda_I=9.94$ cm, which allows the containment of the hadronic shower within the calorimeter. Additional precautions were chosen in the LAr gaps geometry, to avoid ions accumulation.

2.2.4. Muon Spectrometer

The muon spectrometer, or also muon system (MS) is composed of the outermost detectors in ATLAS and is designed to measure the momenta of MIP particles which still emerge from the calorimeters and which, at the energy provided from the LHC, are muons. The calorimeters depths strongly limit the *punch-through* of other particles. In order to provide the curvature of the muons, the MS are immersed into the magnetic field generated by the toroid magnet system. Since the toroid field is oriented in the transverse plane, entering muons bend in the η direction. The MS is then comprised of four sub-detectors, two in the barrel region and two in the end-caps. Each of those have a subregion which provides fast measurements, integrated in the trigger system, which is discussed later. The sub-detectors are: the Resistive Plate Chambers (RPC) and Thin Gap Chambers (TGC) which are the ones providing this kind of fast measurements; the Monitored Drift Tubes (MDT) and the Cathode Strip Chambers (CSC) instead are providing slower but more accurate muons momenta.

The schematic diagram of the MS is shown in Figure 2.10. Details of the four subsystems are given in the Appendix.

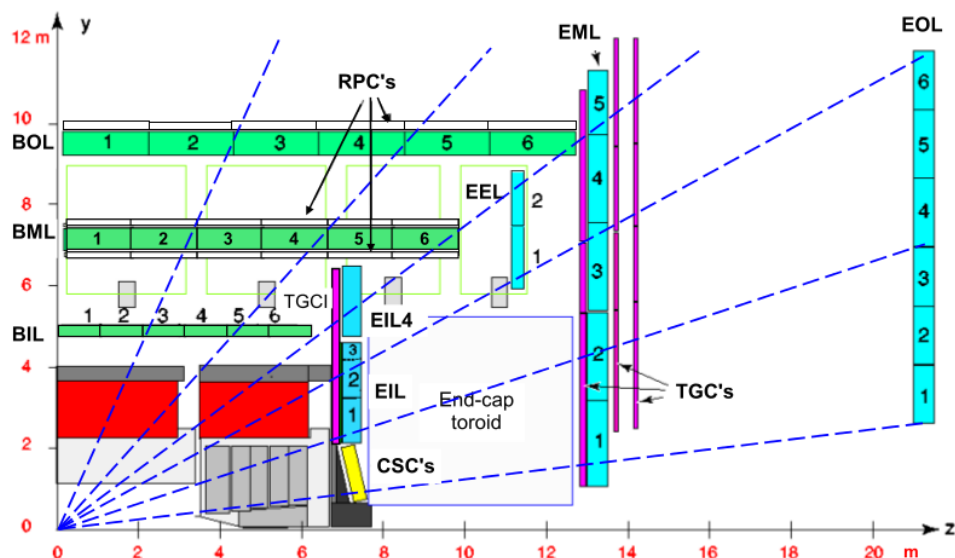


Figure 2.10: Disposition of the muon system sub-detectors and geometry arrangement in ATLAS. Here BIL, BML and BOL are the MDS's barrel layers and EIL, EML and EOL end-cap layers.

2.2.5. Trigger System

The size of digitized event, containing all the information from tracks 4-momenta, calorimeter energy deposit, muons and so on, is approximately above the scale of 1 MB. At the rate of LHC of 40 MHz, the expected data read out and recorded would be in the order of tens of PB/s, hence making the recording of such an amount of data impossible. This makes a priority the presence of a trigger system to select only the most interesting events, also taking care that it will not affecting physical analyses and cover all the possible topologies. From Figure 2.11, SM processes are shown, which range from the total inelastic cross section σ_{tot} (around 100 mb), to rarer processes like Higgs production. Here it is important to note the logarithmic scale: the amount of “interesting” events, i.e. the ones through which one could probe New Physics, are overwhelmed by known processes like e.g. QCD di-jet events. The typical observables used in the trigger system are high- p_T electrons, muons, taus, photons, jets, missing transverse momenta (E_T^{miss}).

Because of the complexity of the read-out of the entire detector and the time needed to build up the event from raw signals, a sophisticate multiple-step trigger have to be used, allowing a stepwise trigger decision also using storage buffers.

The ATLAS trigger system is comprised of Level 1 (L1) and High Level Trigger (the last before Run 2 upgrade was comprised of Level 2 (L2) and Event Filter (EF)), which allows the reduction of the rates from ~ 40 MHz to ~ 75 kHz (L1) and to ~ 200 Hz (HLT). Further details on the L1 and HLT are given in the Appendix.

2.2.6. Luminosity Measurement

All the physics programs at ATLAS share a common key component: the necessity of an accurate measurement of the delivered luminosity. In particular, for cross-sections measurement, the uncertainty on the delivered luminosity is often one of the dominant sources of systematics. In addition to that, searches for physics beyond the SM also rely on accurate information about the delivered luminosity to evaluate background levels and determine sensitivity to the signature of new phenomena [14]. Further details are given in the Appendix.

The most important sub-detectors deputed to luminosity measurement are: the Luminosity measurements Using Cherenkov Integrating Detector (LUCID, rebuilt for Run 2 to cope with the increase luminosity and 25 ns bunch spacing) and Absolute Luminosity for ATLAS (ALFA), a system which is designed to measure the elastically scattered protons (in particular in the Coulomb-Nuclear interference regime) and hence extrapolates the absolute luminosity. It is worth noting that also non-dedicated sub-detectors can perform luminosity measurements, like e.g. Tile Calorimeter.

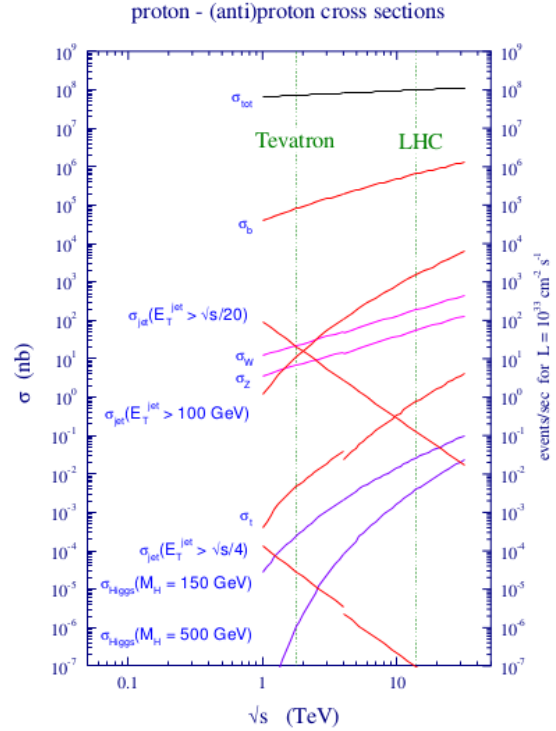


Figure 2.11: Cross sections of various SM processes as a function of the center-of-mass energy, from Tevatron to LHC measurements.

ATLAS	Description and performance
Magnetic field	2 T solenoid; 0.5 T toroid barrel and 1 T toroid end-cap
Tracker	Inner detector: IBL, Silicon pixel and strips, TRT $\sigma_{p_T}/p_T \simeq 5 \times 10^{-4} p_T \otimes 1\%$
EM calorimeter	EMB, EMEC and pre-sampler (Liquid Argon and lead) $\sigma_E/E \simeq 10\%/\sqrt{E} \otimes 0.7\%$
Hadronic calorimeter	Tile (Fe and scintillating tiles) and HEC (Cu and LAr) $\sigma_E/E \simeq 50\%/\sqrt{E} \otimes 3\%$
Muons	Inner detector and muon spectrometers $\sigma_{p_T}/p_T \simeq 2\%$ at 50 GeV $\sigma_{p_T}/p_T \simeq 10\%$ at 1 TeV
Trigger	L1 and HLT (L2 and EF) Rates from ~ 40 MHz to ~ 75 kHz (L1) and to ~ 200 Hz (HLT)

Table 2.1: Recap of ATLAS and performances of the sub-detectors, values in GeV for energies and momenta (where not stated differently).

3. Monte Carlo Simulation

The performance study presented in this thesis makes use of Monte Carlo generators; this section introduces the concept and specifies the dataset used. The purposes of a Monte Carlo simulation are different, from signal to background separation in physical analyses to comparison between data and theoretical prediction and to calibration and performance studies. The general use in high energy physics can be divided in *event generation* and *detector simulation*.

3.1. Event Generation

The first step for a MC simulation is the event generation, where the hard-scatter process is simulated using the matrix elements and the phase space integration (this step can be done analytically for simple topologies, but in general is done numerically with Monte Carlo methods). Afterwards the parton showers and the phenomenological models for the hadronization are applied (described in details in section 4.1). The relevant input to this simulation step is the information from the Parton Distribution Functions (PDFs) set which models the parton distribution inside the colliding protons; they are particularly important when it comes to precise simulation of high energy processes. An additional output of the event generation is the *underlying event*, which comprises the particles coming from the remnant of the proton after the collision; those particles undergo then the process of parton shower and hadronization as the ones coming from the hard-scattering (discussed also in the next chapter).

3.2. Detector Simulation

After the event generation, the interaction between the detector and the particles is simulated. This process includes then the electromagnetic and hadronic shower evolution in the calorimeter. A complete model of the ATLAS detector is provided

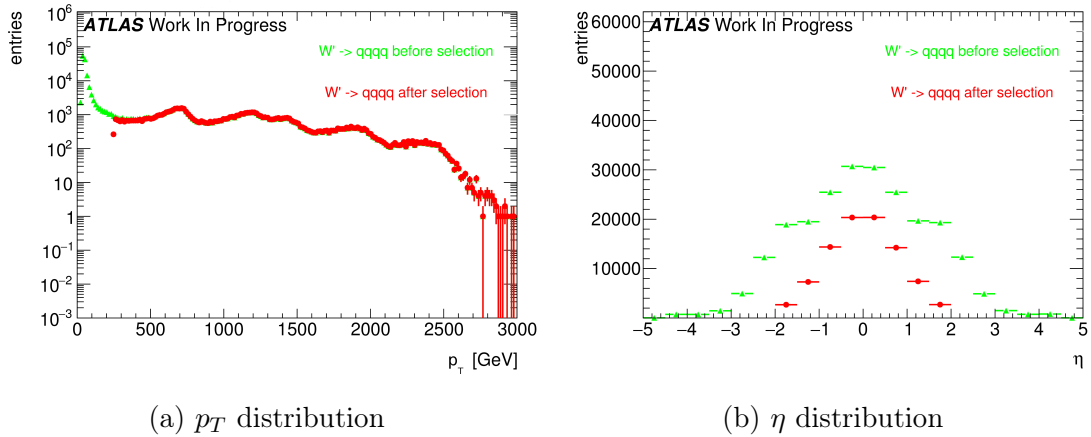


Figure 3.1: Kinematic distributions for the jet of the W' sample.

by GEANT4 [22]; it simulates the hits in the tracker system, the energy deposit in the calorimeter and all the other sub-detectors (*digitization*); moreover it runs the tracks, muons and jets reconstruction algorithms based on the simulation, to emulate a real-life detector-like output for the studies.

3.2.1. MC Sample

The samples used are divided into two main groups: SM background and beyond SM signal. The SM background includes the QCD multijet samples, produced with a falling p_T spectrum. The beyond SM signals are $W' \rightarrow WZ \rightarrow q\bar{q}'q\bar{q}$, $Z' \rightarrow t\bar{t}$ (top quarks considered in the full hadronic channel ($t \rightarrow W(\rightarrow q\bar{q}')b$)) and RS-Graviton $\rightarrow hh \rightarrow b\bar{b}b\bar{b}$, i.e. final states have only jets in all the samples. The details of the samples are given in Table 3.1; the masses considered span from 0.5 to 5 TeV to improve and diversify the kinematic space covered.

A set of kinematic distributions for the W' is shown in Figure 3.1: on the left the p_T distribution where the kinks correspond to the Jacobian peak of the mass considered and the η distribution on the right. The green dots represent the distribution before the selection, which is $p_T > 250$ GeV and $|\eta| < 2.0$ and the red dots after this selection. This selection typical for many searches for BSM physics. All the other samples and the background can be found in the Appendix. In what follows, it will also be used the nomenclature *boosted W/Z* for the W' sample, *boosted tops* for the Z' sample, *boosted Higgs* for the G_{RS} sample and *massive W* for the $W' \rightarrow \tilde{W}\tilde{W}$ with $m_{\tilde{W}} = m_t$.

Process	ME Generator & Fragmentation	ME PDFs	UE Tune	Resonance Masses
QCD multijet	Pythia 8	NNPDF23LO	A14	N/A
$W' \rightarrow WZ$	Pythia 8	NNPDF23LO	A14	1.5, 2.5, 3, 4, 5 TeV
$Z' \rightarrow t\bar{t}$	Pythia 8	NNPDF23LO	A14	1.5, 1.75, 2.5, 3, 4, 5 TeV
$G_{RS} \rightarrow hh(\rightarrow b\bar{b})$	Pythia 8	NNPDF23LO	A14	0.5, 1, 1.5, 2, 2.5, 3 TeV
$W' \rightarrow \tilde{W}\tilde{W}$ with $m_{\tilde{W}} = m_t$	Pythia 8	NNPDF23LO	A14	1.5, 2.5, 3, 4, 5 TeV

Table 3.1: Overview of the Monte Carlo Samples used. The first line shows QCD standard model process, the second, the third and the fourth the beyond SM samples considered; the last line the “massive W/Z ” sample.

4. Jet Reconstruction

This chapter provides an introduction to basic concepts of jets, from parton shower, to hadronization and to the algorithms used to build the jets from calorimeter input.

4.1. Jet Phenomenology

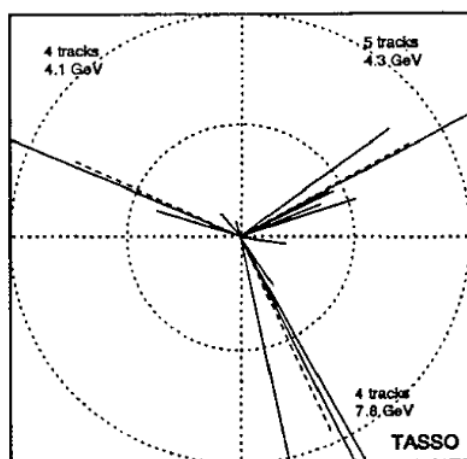


Figure 4.1: 3-jet in the final state with gluon bremsstrahlung off a quark in e^+e^- annihilation in $e^+e^- \rightarrow q\bar{q}g \rightarrow 3\text{-jets}$.

Given a quark or a gluon present in the final state, e.g. coming from a W or Z decay, in the perfect case one would aim at reconstructing as precise as possible the 4-momentum of those quarks or gluons, which means measuring the energy, direction and the mass or transverse momentum. Unlike electrons or muons, those particles are subjected to Quantum Chromodynamics, the theory of strong interaction already described in Section 1.3.2.

4.1.1. Parton Showering

Quarks, which were produced in a hard interaction will radiate a gluon (gluon *Bremsstrahlung*) at the scale of $1/E \ll 1$ fm, mostly collinearly in the direction

of the quark, $dN/d\Theta^2 \sim 1/\Theta^2$ [16]. An historical example of this process is given from the event in the TASSO detector [15] depicted in Figure 4.1. Subsequently, the gluon will split into two gluons or quark-antiquark pair which will split again in quarks and gluons, so that the original quark fragmented into quark/gluon cascade within a narrow cone. These two processes are referred together as *fragmentation*,

which results in the *parton shower*.

Further details on fragmentation, DGLAP equations and Sudakov factor can be found in the Appendix.

Due to the asymptotic freedom, quarks and gluons resulting from the fragmentation behave as quasi-free particles called partons, only at short distances (order of 10^{-2} fm). On the distance of the order of >1 fm, color confinement takes place, where colored partons form colorless hadronic final states. This process is referred to as *hadronization*, which is a stochastic process involving a large number of particles, also described in the next section. The hadronization proceeds, in fact, through the formation of jet in high energy processes.

4.1.2. Hadronization

When the colored partons are separated more than 1 fm, a gluonic flux tube of narrow transverse dimensions builds up which fragments into ordinary hadrons (similar mechanisms lead to the hadronization of gluons). As a result of this, instead of partons one can see jets of colorless hadrons which are clustered together. Due to the limited sensitivity of the detector, the properties of particles inside the jet cannot be individually measured in a precise manner, but the properties of the initial parton from the hard scatter can be reconstructed.

Because of its non-perturbative nature, the process of hadronization is described phenomenologically through various models including: independent jet fragmentation, Lund string model and cluster hadronization.

All of these models are described in the Appendix.

These hadronization schemes are implemented in different MC QCD event generators: string model in PYTHIA and the cluster model in HERWIG. Events generated using PYTHIA are also studied and used for the evaluation of the performance study presented in this thesis.

The only thing that defines a jet is the method which is used for its reconstruction.

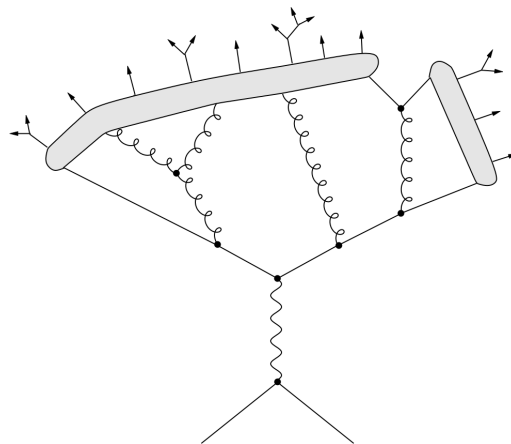


Figure 4.2: Schematic representation of the string model, used in PYTHIA.

4.1.3. Jet Reconstruction

After initial quarks and gluons from the hard-scattering have passed the process of parton showering and hadronization, the resulting jets of particles, mainly hadrons (pions followed by kaons and protons), enter the detector, interacting first with the Inner Detector, where tracks from charged particles are reconstructed, and then with the calorimeter system. Here the further evolution of showers, originating from the hadrons or leptons, is stimulated by the passive material as shown in Figure D.1.

The energy of the incoming particle populates the cells (both in lateral and longitudinal way) along the original direction and is then detected and register from the readout electronics.

The cells are then grouped together in order to find the energy deposited from hard-scatter activity. Additionally, a local calibration is used to reduce noise contribution. Those steps are called *Topo-clustering* and *Local Calibration Weighting* (LCW) and described in the Appendix. These 3-dimensional object, the topo-clusters, are used as input to the Jet Reclustering Algorithms.

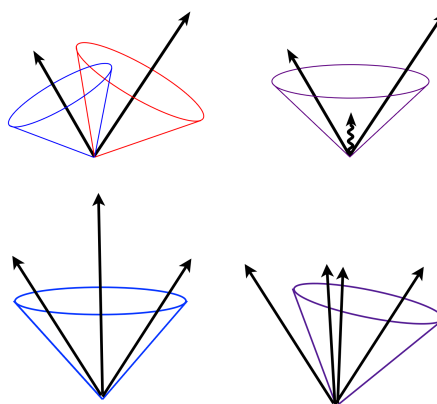


Figure 4.3: The behavior of well defined jet algorithms is shown. Infra-red safety: emission of soft particles should not change the configuration (top from left to right). Collinear safety: substituting one particle with two collinear ones, should again not change the configuration (bottom from left to right).

Jet Reclustering Algorithms

There are three main algorithms used to reconstruct a jet in ATLAS. Although they may look very different in the way they associated objects in the calorimeter (topo-cluster) or e.g. the tracker system (tracks), they share the same fundamental properties.

Well-behaved jet algorithms should be infra-red (IR) safe and collinear safe, meaning that adding a soft particle or the collinear splitting of a hard particle should not change the number of reconstructed hard jets in the event. An intuitive understanding of the IR and collinear safety is depicted in Figure 4.3.

The *sequential recombination jet algorithms* discussed here are parametrized by the power of the energy scale in the distance measure. The most used algorithms are: anti- k_t , k_t and Cambridge/Aachen (C/A). The algorithm SISCone will not be considered in this introduction, since is rarely used within ATLAS. The only difference between them is the definition of the distance d_{ij} between inputs i and j and the distance d_{iB} between the input i and the beam B , but it can be written in the same way for all the three:

$$\begin{aligned} d_{i,j} &= \min(k_{ti}^{2p}, k_{tj}^{2p}) \frac{\Delta_{ij}^2}{R^2} \\ d_{iB} &= k_{ti}^{2p} \end{aligned} \quad (4.1)$$

where $\Delta_{ij}^2 = (y_i - y_j)^2 + (\phi_i - \phi_j)^2$, k_{ti} , y_i and ϕ_i are transverse momentum, rapidity and azimuth of particle i . The algorithms starts by identifying the smallest of distance d_{ij} ; if it is smaller than d_{iB} the inputs i and j are combined together and if it is instead bigger than d_{iB} , then the entity i is called jet and removed from the list of inputs.

The radius parameter R defines how big the final jet would be (for large R the distance d_{ij} is smaller, hence increasing the inputs which will be added to the jet, since d_{iB} is fixed). The standard jet size in ATLAS is 0.4, while in this thesis focus will be held especially in jets of radius 1.0. The parameter p governs the relative power of the energy versus geometrical (Δ_{ij}) scales.

For different choice of p we recover the different algorithms:

- For $p = 1$ we have the k_t algorithm; it starts adding together the low p_T inputs at large angle (this way d_{ij} is smaller).
- For $p = 0$ we have the C/A algorithm; here only the geometrical measure is considered, since the momenta are set to 1.
- For $p = -1$ we have the anti- k_t algorithm; it starts adding high p_T inputs, since the inverse of high transverse momenta will have a low value.

Another important concept is the *ghost association*, which can be defined together with the *jet area*.

Jet Area and Ghost Association

The jet area is a quantity related to the jet's susceptibility to diffuse radiation. It is calculated by means of *ghost particles*: a large quantity of unphysical particles is

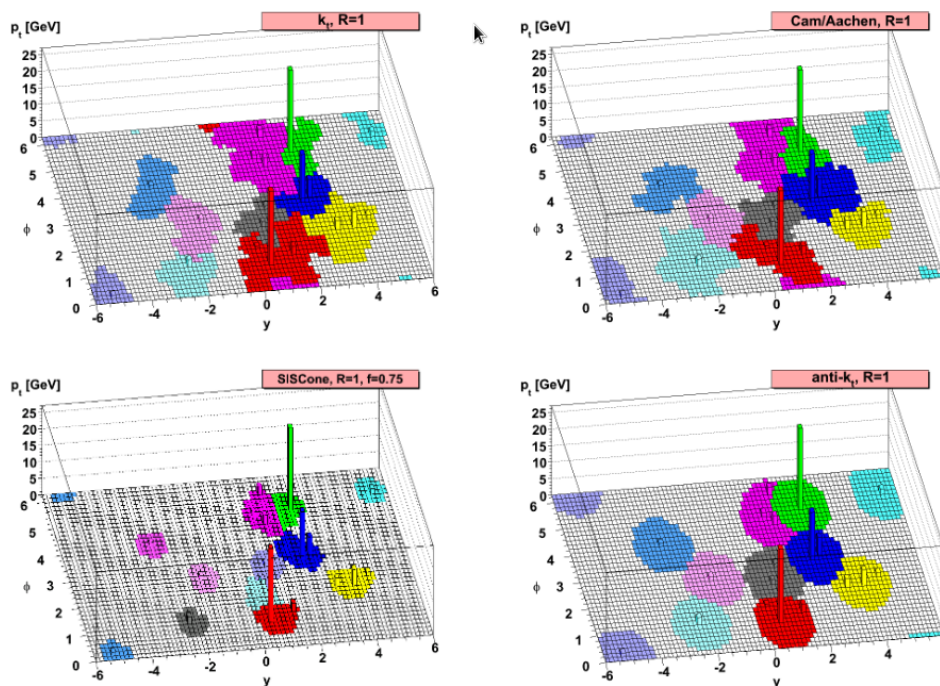


Figure 4.4: Overview of the various reclustering algorithms. SISCone is not described.

added randomly to the set of inputs of the jet. Those particles are created with a transverse momentum and a mass very close to zero, in order to reproduce the limit of soft infrared radiation. After the reclustering, a subset of ghosts will be taken inside the jet; the η, ϕ region in which those particles are is called the (active) jet area. The geometry and topology of the areas depends on the algorithm used: for the anti- k_t the shape is circular, while the area is independent of the jet p_T . For the C/A and k_t , the shapes are irregular and the area also depends on the jet p_T . The areas are also shown in Figure 4.4.

The concept of Ghost Association comes with a general problem of associating an object (e.g. tracks or truth particles) to the corresponding jet, for example to study the properties and explore correlations in quantities coming from the calorimeter and the tracker system. The most naïve, but still powerful approach is to use ΔR to associate them: the distances in η, ϕ are calculated, and the objects whose distances are below a certain threshold (e.g. for anti- k_t jets of radius 1.0 this value would define the threshold) are (univocally) assigned to one jet. While this method is relatively simple and easy to implement, it has some disadvantages with k_t or C/A jets: their irregular shapes compromise the correctness of the assignment since not always the closest object is also the one taken by the reclustering.

The alternative and more sophisticated approach is then the Ghost Association: the given objects (again tracks or truth particles) are reduced to ghosts, scaling down their mass and transverse momenta to values near zero, yet preserving the directions. After running the jet algorithm, the ghosts will be inside one of the jets or none of them, not necessarily the closest but inside the area of the one to which it is associated. Intuitively one can think as follows: if the particle momentum points toward the area of a jet, it will be univocally associated to that jet (the unambiguity is inherited from the jet algorithm itself). The Ghost Association is an important tool also used in the work presented in this thesis.

4.2. Basics of Calibration and Uncertainties

There are two main and important procedure when it comes to jets in high-energy particle physics: calibration and uncertainty.

4.2.1. Responses Jet Energy Scale and Resolution

Two important tools which are used within these procedures are the *Jet Energy Scale* (JES) and *Jet Energy Resolution* (JER). They are based on *Responses*: given any observable X , which we have in the form “estimated” (X^{reco}) and “reference” (X^{ref}), from example a reconstructed quantity and a measurement which is trusted more because the underlying physical process is well known and described, the response is built from their ratio:

$$R_X = \frac{X^{reco}}{X^{ref}}$$

The JES and JER are then the mean and standard deviation of the energy response. Other important tools are the *Jet Mass Scale* (JMS) and *Jet Mass Resolution* (JMR), important for large- R jets discussed later and built upon mass responses.

4.2.2. Calibration

The calibration accounts for various effects which affect the measurements of jet’s properties:

- Calorimeter non compensation: different energies scales of hadronic and electromagnetic showers, often shown as the ratio e/h , is caused mainly by decay of nuclei during the interaction of the shower with the calorimeter, which remains undetectable;

- Dead material: energy lost in areas of the calorimeter which are not sensitive;
- Leakage: showers which reach the end of the calorimeter system and are therefore not contained and fully measured;
- Out of calorimeter jets: all those particle jets which are not reconstructed as calorimeter jets;
- Energy deposits below the noise threshold;
- Pile-up contamination.

All these effects require a dedicated chain of procedures, both involving Monte Carlo simulation and measurements, which is shown in Figure 4.5.

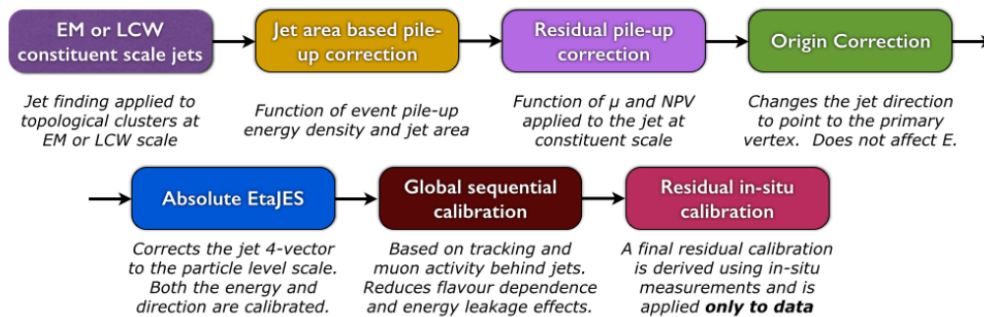


Figure 4.5: Overview of the current calibration procedure in ATLAS.

The procedure includes the following steps [23]:

- EM or LCW constituent scale jets: they are the input to the jet calibration: Local Cluster Weighting is described in the Appendix;
- Origin Correction: the momentum of the jets is corrected to point to the primary vertex, improving η resolution;
- Jet area based pile-up correction: the pile-up (described in Section 4.3.2) can be parametrized both by the number of primary vertices N_{PV} and by the average number of interactions $\langle\mu\rangle$ per bunch crossing; Monte Carlo is used to simulate this effect both from the same (*in-time pile-up*) and in others (*out-of-time pile-up*) bunch-crossings. The correction depends on the ghost area and a parameter evaluated event-by-event as a function of N_{PV} ;
- Residual pile-up correction: removes the additional, non linear dependencies both from N_{PV} and from $\langle\mu\rangle$;

- Absolute EtaJES: corrects the JES and the η of the jet using the information from MC truth, such that the energies and η are as close as possible to the MC truth;
- Global Sequential Calibration: big step which takes into account the differences between quark- and gluon-initiated jets, jets which are not fully contained, and the non-compensation. It is comprised of five stages, using the energy deposit information, the tracker system, and the muon segment; the correction is parametrized in η and p_T ;
- Residual in-situ calibration: is the final step which uses a data driven method, exploiting processes in which a well measured reference object is recoiling against a jet (the processes are e.g. $Z/\gamma + jet$ and di-jet).

4.2.3. Uncertainties

The JES calibration chain discussed above could introduce systematic biases across its various steps; dedicated in-situ analyses measure the uncertainties with respect to transverse momentum and pseudo-rapidity of the jet, as differences in the responses between data and simulation in well known SM processes. Additionally, systematic uncertainties account also for the MC simulation used, pile-up suppression modeling and flavor dependencies. The JES uncertainties are constructed from:

- $\mathcal{O}(20)$ systematic in-situ;
- $\mathcal{O}(30)$ statistical from in-situ;
- $\mathcal{O}(20)$ from jet flavor, pile-up, single hadron response, read-out settings and event reconstruction changes, IBL effects.

The largest contributions come from the flavor composition, since quark-initiated jets have a different response than gluon-initiated, and in-situ systematics.

The JES uncertainties are evolving and improving together with the calibration chain for the JES.

The JER uncertainties are related to the width of the response (the mean is the JES), which should be as small as possible (since it quantifies the spread of the energies around the correct value); it is parametrized in terms of the jet transverse momentum with a noise, stochastic and constant term. They are calculated usually using in-situ methods.

4.3. Jets in the *Boosted* Regime

The Beyond the Standard Model processes considered are characterized by a high resonance mass, from 0.5 to 5 TeV, since for those models the masses below that value are excluded at 95% confidence level from both ATLAS [26] and CMS [27] analyses. (For further information, the ATLAS Conference Notes for the $Z \rightarrow t\bar{t}$ [28], the $W' \rightarrow WZ$ included in the diboson resonance [29], and the RS-Graviton to $hh \rightarrow b\bar{b}b\bar{b}$ [30]).

Therefore, huge efforts are currently going on to extend these limits further and exclude higher and higher masses. However, probing more massive resonances means probing more extreme kinematic regimes, or *boosted* regimes as referred to within ATLAS, of its decay products.

As an example for the $W' \rightarrow WZ$, taking e.g. $m_{W'} = 3$ TeV, the transverse momentum distribution of the W or Z will have the maximum at the jacobian peak, i.e. $p_T \simeq m_{W'}/2 \simeq 1.5$ TeV, as shown in Figure H.4, in the Appendix.

The main issue of this extreme kinematics regime is not the p_T of the electroweak bosons, but follows the angular separation of the quarks, as pictorially depicted and shown in Figure 4.6. For a generic decay $a \rightarrow b, c$ the separation ΔR in η, ϕ space, neglecting the b, c masses, from simple kinematics reads:

$$\Delta R_{b,c} \simeq \frac{2m_a}{p_{T,a}}$$

This is a crucial point: as the p_T goes higher, the angular separation decreases. Since the resonance masses of physical interest are very large, following the jacobian distribution, the transverse momentum of the intermediate decay product (here considered $W/Z, t\bar{t}, hh$) also is large, but conversely the angular separation ΔR between the final-state quarks which give rise to two (or three for the tops) distinct jets will be small.

An extreme situation is in Figure 4.6 on the right, the two once separated jets (left) whose reconstruction could be done without additional complications with jet reconstruction algorithm of standard ATLAS radius of 0.4, approach each other at the level that the two jets touch or even merge to one.

This is quantitatively shown in Figure 4.7: the angular separation follows the relation given above and shows the hyperbolic shape. The green line shows the constant $\Delta R=1.0$. For the standard jet algorithm anti- k_t with radius 0.4, considerably many top quark's decay product, and a huge amount of quarks from W/Z would be reconstructed together. At this point, the standard reconstruction techniques

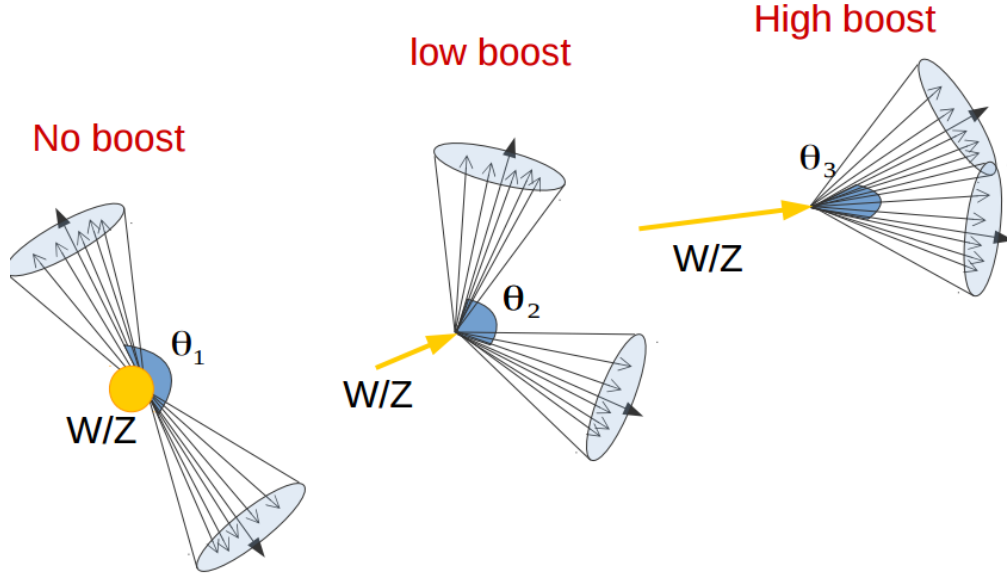


Figure 4.6: Impact of the extreme kinematic regime on the decay products, with $\theta_1 > \theta_2 > \theta_3$.

become to fail, and the jets are not anymore individually resolved by standard jet algorithms. This poses a serious problem and a challenge of extreme priority, being the precise reconstruction of these object’s properties a crucial issue in searches for beyond SM physics and limit setting.

The simple idea is then to extend the jet radius to 1.0 or more, such that all the decay products fall inside it, and start looking into the *substructure*, developing a series of new technologies in order to assure a better reconstruction. The jets which are built with such a large radius, are called *large- R jets* or sometimes in papers, *fat jets*.

4.3.1. Large- R jets

Large- R jets are jets constructed with a radius parameter of the reclustering algorithm much bigger than the standard 0.4; within ATLAS the size of large- R jets is 1.0 for anti- k_t and 1.2 for C/A (the area of C/A is $\sim 20\%$ smaller than anti- k_t).

It is worth noting that, for a standard anti- k_t 0.4 jet the active area [17] is $A_{\text{anti-}k_t} = \pi R^2 \simeq 0.5$, while it is $\simeq 3.14$ for 1.0 jet, i.e. around six times bigger.

Already from this “geometrical” point of view, the necessity of further techniques can be understood: the effect of soft radiation contamination from Pile-Up (PU) and Underlying Event (UE) will be in this case six times bigger and spoil the efficiency of the jet mass measurements.

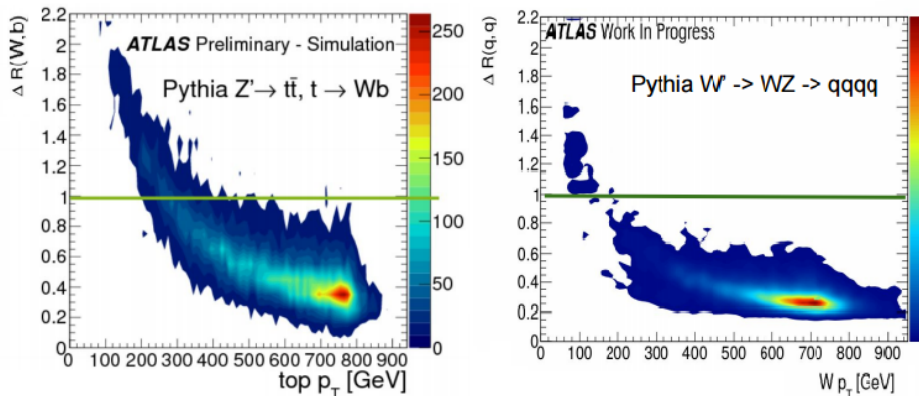


Figure 4.7: Angular separation ΔR on the left between W and b quark from top quarks decay and on the right ΔR between the quarks from W/Z hadronic decay. In the first case the samples were obtained with a Z' and in the second with a W' . Masses were 1.6 and 1.5 TeV. Left picture from [31].

4.3.2. Pile-Up and Underlying Event

The *pile-up* is a term used to describe the jets coming from another interaction in the same bunch-crossing (*in-time pile-up*), i.e. coming from an interaction at low- p_T , which happens together with the hard-scattering, or in another bunch-crossing (*out-of-time pile-up*), before or after the hard-scattering. The Underlying Event (UE) describes all the hadronic activities of soft parton-parton scattering in the single proton-proton interaction, which accompany hard-scattering process. Further details in the Appendix.

4.4. Substructure: Grooming Techniques

This section is based on the 7 TeV article on jet Substructure [31]. In order to use large- R jets, it is necessary to gain additional information on the interior of these objects, i.e. using techniques that exploit its substructure allowing a jet-by-jet discrimination of the energy deposit most likely coming from the hard-scattering to other soft radiation.

A common feature in substructure is the use of *sub-jet*, i.e. jets obtained from a parent jet (e.g. the large- R jet), using its constituent but running the jet reclustering algorithm with a smaller radius parameter; in one large- R jet, typically there are two or more sub-jets depending on the originating process and its p_T .

Techniques have been developed, both using sub-jets or directly constituents of a jet, which are referred to as *grooming* algorithms.

Grooming algorithms are designed to retain the characteristic substructure within such a large- R jet while reducing the impact of the fluctuations of the parton shower and the UE, thereby improving the mass resolution and mitigating the influence of pile-up.

The grooming algorithms presented here are the most important ones in ATLAS: the *Trimming*; other used as well, the *Split-Filtering* and the *Pruning* can be found in the Appendix.

4.4.1. Trimming

The trimming algorithm is the most important in ATLAS and the one mainly used in the work presented in this thesis. It takes advantage of the fact that contamination from soft radiation has a much lower p_T with respect to the hard-scattering component. Therefore uses a transverse momentum balance to distinguish among those. The algorithm works on a two-dimensional parameter space: R_{sub} and f_{cut} . The steps are as follows:

- k_t algorithm (but of course other choices are also possible) is used to create sub-jets with a smaller radius R_{sub} , aiming at separating the soft radiation from the hard one in different sub-jets. Typical choices are 0.2 and 0.3 (0.2 is used as standard);
- for each sub-jet, the ratio f_{cut} of its p_T with the parent jet p_T^{jet} is calculated: if then this ratio is below a certain value, the sub-jet is removed. Standard choice is $f_{cut} = \frac{p_T}{p_T^{jet}}=0.05$;
- the sub-jets which survived this procedure are the only one which compose the trimmed jet.

The trimming procedure is also explained in Figure 4.8, an example of performance in simulation with standard parameters is shown in Appendix (Figure E.2).

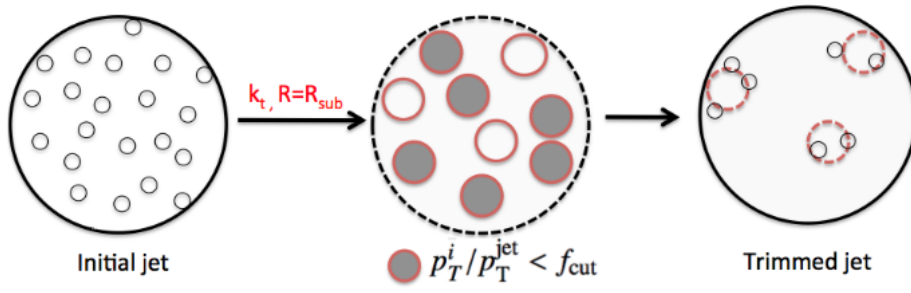


Figure 4.8: Schematic of the trimming algorithm.

5. Optimization of Large- R Jet Mass Reconstruction

In this chapter the main outcome of the work of this thesis is presented. The variable track-assisted sub-jet mass (m^{TAS}) will be then defined and its performance will be presented and confronted with two standard definitions, the track-assisted mass m^{TA} and the calorimeter mass m^{calo} . A further development, the combined mass of m^{TAS} and m^{calo} , that is called m_{TAS}^{comb} , is shown. It is presented and also confronted with its counterpart used in ATLAS m^{comb} , the combined mass of m^{TA} and m^{calo} .

5.1. Calorimeter Mass

Once the collection of constituents from the large- R jet is groomed, it is possible to use them for the measure of physical related properties such as the jet mass, since the possible sources of soft radiation from PU and UE have been reduced.

The *calorimeter mass* or m^{calo} is a widely used variable which takes as input the topo-cluster information. Given that each topo-cluster i has a 3D information on the energy deposit, E_i , the mass can be simply calculated from 4-vector properties:

$$m^{calo} = \sqrt{\left(\sum_{i \in J} E_i\right)^2 - \left(\sum_{i \in J} p_{T,i}\right)^2}$$

where J labels the Large- R jet.

5.2. Track Mass

This section briefly presents the tracks and their relation with the large- R jet's properties. There are significant advantages and few disadvantages of their usage for precise jet mass reconstruction, which are inherited both from the detector experimental properties and from the underlying physical processes.

First of all the excellent performance of track reconstruction and angular separation at low p_T is intrinsically better than the calorimeter one (see the Chapter 2. and Table 2.1). The second main advantage is that tracks can be associated with the primary vertex, thus simply excluding those from PU or other beam-induced soft radiation background (this is not the case for the UE).

The requirement made on tracks to achieve optimal performance are grouped into two categories, the quality of the track, i.e. if it was fully reconstructed from the detector and separated from others with no ambiguities, and the association conditions with the primary vertex:

- $p_T^{track} > 400$ MeV;
- $|\eta| < 2.5$;
- Maximum 7 hits in the Pixel and STC sub-detectors;
- Maximum 1 Pixel hole;
- Maximum 2 silicon holes;
- Less than 3 shared modules;
- Maximum 2 mm of displacement along beam axis (z_0) from the primary vertex;
- Maximum 2.5 mm of distance in x-y plane from the primary vertex and point of closest approach (d_0).

Given the set of tracks which pass this selection, the mass m^{track} is calculated summing up the 4-momenta of those tracks which are ghost associated to the groomed jet.

Apart from this benefits which derive from the tracker system, there is also an important disadvantage which comes from the underlying physics: it is completely blind to the electrically neutral component (mostly π^0) of the jet. As seen in Figure 5.1, the track mass (red distribution) is not only shifted towards lower values than the calorimeter mass (green distribution), but its width also degrades.

Tracks could be used either for independent mass reconstruction (and in this section is shown how this is not the case), or, most importantly, as an ulterior information to the calorimeter measurement.

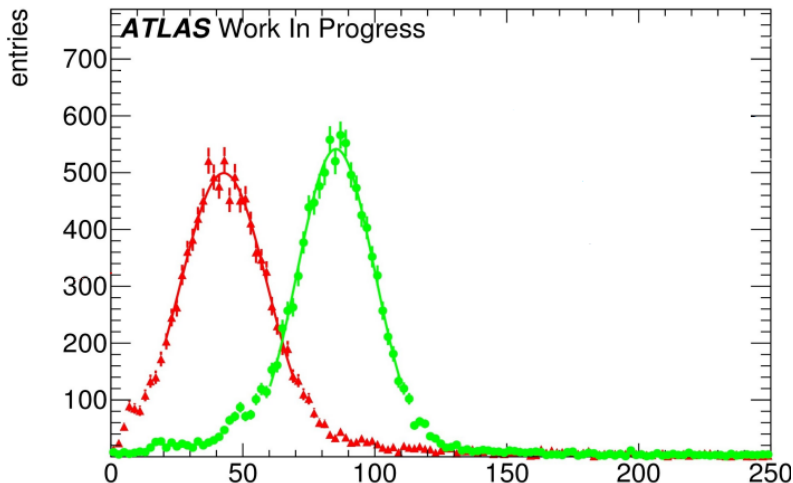


Figure 5.1: Mass distribution boosted W/Z : in green the m^{calo} and in red the m^{track} .

5.3. Performance Figure of Merit (FoM)

Since we already introduced the calorimeter and track mass, a concrete, quantitative feature has to be defined in order to understand which observable is “better”, in the sense that we would prefer one or the other according to this criterion. This is often referred to as *Figure of Merit* or simply FoM.

There are few ways to look at the FoM: one can e.g. naïvely think about the mean of the mass distribution, since closer values of the mean to the e.g. W or Z mass (if we are speaking about W/Z decays), indicate a more correct mass reconstruction. However, this does not take into account the width of this distribution, as a large width spoils the reconstruction in terms of percentage of jets misreconstructed. Moreover, the mean is not as important since it can be rescaled to the desired value in a calibration procedure.

5.3.1. Gaussian Fit

The important feature to keep in mind, in fact, is the underlying physics which brings us to calculate the mass of a jet. In figure 5.2 this is made clear: if the width of the invariant mass distribution of the jet is smaller (highlighted), it allows a bigger background rejection, here shown as the QCD dijet, and a higher signal efficiency, by means of a simple mass requirement.

The width σ of the distribution, which can be obtained from a fit to the Gaussian core, is already a valid FoM, which has an underlying physical feature. Moreover, in order to be independent from the mean of the distribution, the width can be divided

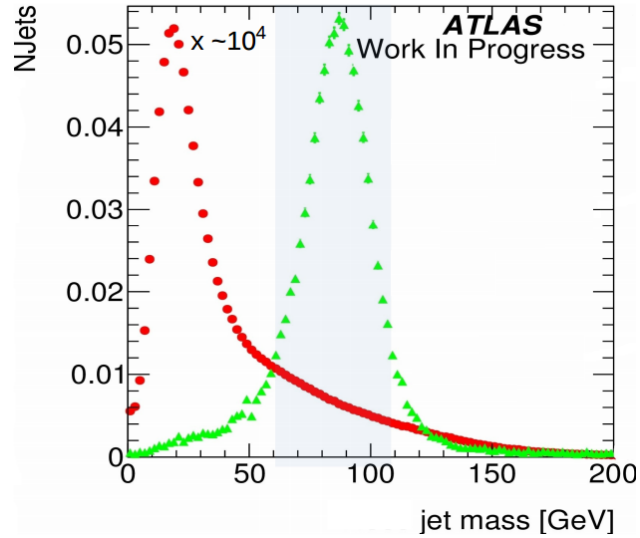


Figure 5.2: Mass distributions: in red the QCD dijet background rescaled, in green the W/Z from the W' sample. Highlighted the width of the W/Z distribution.

by the mean itself. This was in fact the FoM which was used at the beginning of the work for this thesis, since it provided a simple and fast solution. However, special care must be used both in the procedure of fitting Gaussian cores of responses, since they are asymmetric, and to how the tails are treated.

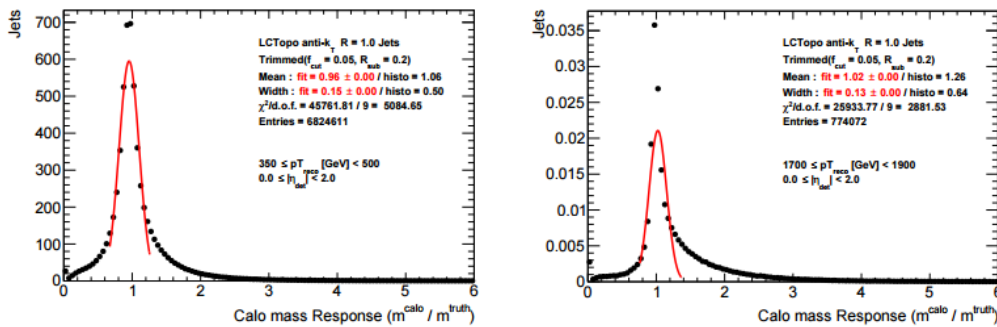


Figure 5.3: Mass Response distributions for the QCD multijet for various p_T ranges: on the right the failure of the Gaussian fit shows the limitation of this approach to evaluate the Figure of Merit. On the plot the fit parameters and transverse momentum ranges.

The situation is depicted e.g. in Figure 5.3, where a mass response is shown for calorimeter mass for QCD multijet: here the presence of a right-handed tail which enhances going from low to high transverse momenta makes the Gaussian fit clearly not the tool which provides the stability needed. The ideal tool should

take care of managing the presence of at least tails outside the Gaussian core and should converge to the intuition of the standard deviation for a perfect Gaussian distribution. The closest tool to this idea was found to be the *InterQuantile Range*, which was therefore preferred and presented in the next section.

5.3.2. InterQuantile-Range

Another way to look at the mass FoM is half of the 68% of the InterQuantile range (IQnR) (here defined such as it corresponds to a sigma of a “perfect” Gaussian distribution: $q84\% - q16\%$ where $q84\%$ is the 84th percentile and $q16\%$ is the 16th, not to be confused with the InterQuartile Range (IQR) which is the $q75\% - q25\%$ and does not correspond to the sigma) divided by the Median ($\frac{1}{2} \times 68\% \text{ IQnR} / \text{median}$). It provides stability and high sensitivity to left-hand-side and right-hand-side tails.

Another important FoM, used for the work in this thesis, is the response distribution: given the reconstructed mass (calorimeter, track or whichever method) one can compare it to its *truth* mass (m^{truth}), computed from the particle at MC level before the interaction with the detector:

$$R_m = \frac{m^{\text{reco}}}{m^{\text{truth}}}$$

Standard descriptor of the FoM e.g. in [24] and here is the IQnR of the R_m .

In Figure 5.4 a mass response for a single range of transverse momentum is shown, for the calorimeter mass. On the plot the contours of a standard deviation and of $q16\%$ and $q84\%$ are drawn with dashed and solid lines, respectively, showing the difference induced by the tail. This sort of plot is the key when looking quantitatively to the observable performance and can be found in the Appendix for each of the process studied in every p_T range considered. In this chapter will be shown, however, the quantity which describes this FOM, the IQnR, as a function of p_T , in order to get an understanding of the behavior in the entire spectrum and assure the exclusion of local sub-optimality.

5.4. Track-Assisted Mass (m^{TA})

The main limitation of the calorimeter mass comes from the angular resolution of the topo-clusters, which, for extreme kinematic regimes, start approaching each other at the point that they hit the granularity of the detector. The main advantage is that on the contrary the relative energy resolution increases at higher energies.

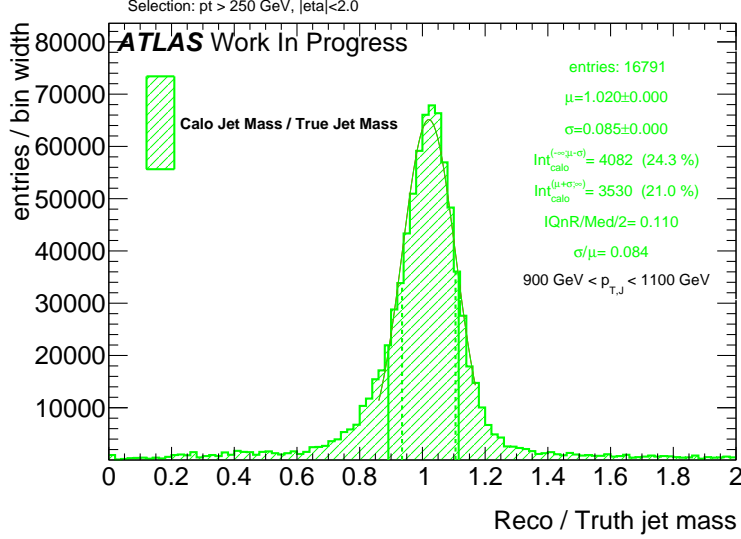


Figure 5.4: Calorimeter mass response plot for boosted W/Z . On the plot, right, are shown: the number of entries, the mean and the width of the fit to the Gaussian core, the integral from 0 to $\mu - \sigma$ and the one from $\mu + \sigma$ to $+\infty$, the values $\frac{1}{2} \times 68\%$ IQnR/median and σ/μ . On the distribution the dashed vertical lines represent the points $\mu - \sigma$ and $\mu + \sigma$ and the solid lines represent the $q16\%$ and $q84\%$.

The tracks instead have a very good angular resolution, but p_T relative resolution degrades linearly with the transverse momentum.

One could then think about creating a variable which exploits the advantages of both and minimizes the disadvantages. As seen, the track mass is missing the neutral component, i.e. each measurement is missing the fraction $\frac{\text{neutral} + \text{charged}}{\text{charged}}$, but it could be corrected on a jet-by-jet basis: this leads to the definition of the *track-assisted mass* (m^{TA}):

$$m^{TA} = \frac{p_T^{calo}}{p_T^{track}} \times m^{track} \quad (5.1)$$

It can be intuitively understood as follows: the term m^{track} has the superior angular resolution, but misses the neutral component; the ratio p_T^{calo}/p_T^{track} , representing exactly the $(\text{neutral} + \text{charged})/\text{charged}$ ratio, “restores” the correct value of the mass back to $\text{charged} + \text{neutral}$.

From Figure 5.5 the comparison of the track-assisted mass and the calorimeter mass; the width of the distribution is smaller, making this observable a good candidate for usage.

The track-assisted mass was first proposed to correct the angular information measurement in the finely segmented electromagnetic calorimeter by the energy

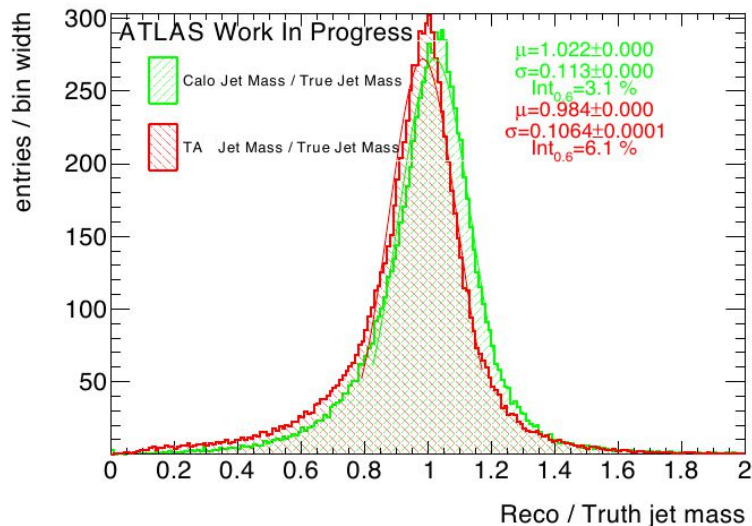


Figure 5.5: Track-assisted mass response plot for boosted W/Z : in green the calorimeter mass, in red the track-assisted mass. On the right are shown properties of the fit to the Gaussian core; it can be seen than the width of the m^{TA} distribution is smaller, and the mean is slightly below the calorimeter mass.

measurement in the hadronic calorimeter that is typically coars [35][36]. Successively, the concept was extended to charged particle tracks, in the context of the top-quark tagging [37], using the HEPTopTagger [38][39]; moreover there have been phenomenological studies using the track-assisted jet mass for boson and top quark jets in the extreme boosted regime [40][41].

5.4.1. Advantages and Limitation of m^{TA}

The m^{TA} has a good handle on boosted W/Z , looking at all the transverse momentum spectrum for these results.

Another big advantage which supports the use of the track-assisted mass is the relatively small uncertainties: in Figure 5.6 the comparison of m^{calo} (left) and m^{TA} (right) fractional uncertainties on the JMS, shows how the tracking uncertainties are much smaller because of the ratio m^{track}/p_T^{track} . On the right plot the black line indicates the JMS fractional uncertainty for the m^{calo} , and is always above the m^{TA} . Of course this introduces another argument in the development of new techniques, which is to look for a good balance between performance and small uncertainties: a perfect observable in terms of behavior which has very big uncertainties is not really useful.

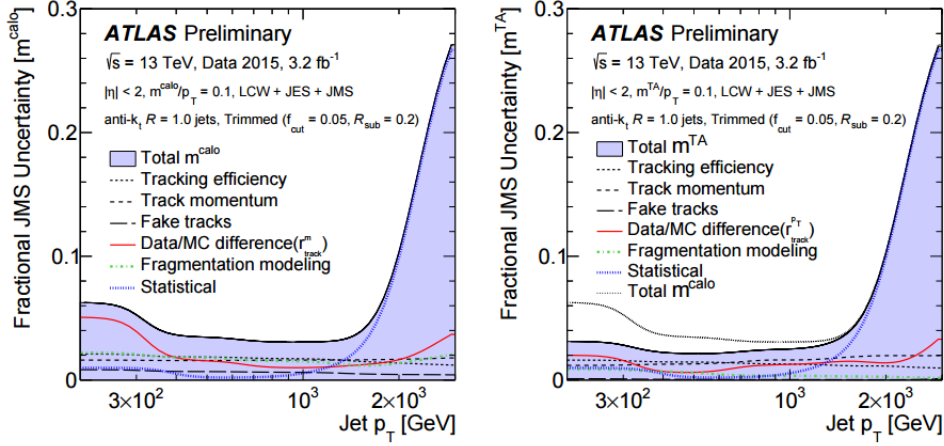


Figure 5.6: Comparison of the uncertainties for m^{calo} , on the left, and m^{TA} , on the right the rise on the high jet p_T is due to statistics. From the [24].

When looking in the extreme kinematic regime, at very high p_T , as in the top plot in Figure 5.7, the m^{TA} shows its real strength, achieving much smaller value of the IQnR. However, there are some severe limitations which are worth noting, especially looking at the performance in different regions of transverse momentum: this is shown in the bottom plot of Figure 5.7, where at a low p_T it exhibits a much worse behavior.

Performance in $W \rightarrow q'\bar{q}$ Decays

The performance in all the bins of p_T can be studied looking at Figure 5.8; these plots have as horizontal axis the transverse momentum and as vertical one the value of the $\frac{1}{2} \times 68\%$ IQnR/median calculated from the correspondingly response. For W/Z jets, there is a crossing point around $p_T \sim 1$ TeV, which can be understood as the point in which the two sub-jet present start merging (sub-jet multiplicity shown in Figure H.5 in Appendix).

Performance in $t \rightarrow q'\bar{q}b$ Decays

For top quarks the situation is much different: with respect to W/Z jets, in fact, there are two main disparities: on one side, the mass of the top quark is much higher than the one of the electroweak bosons, hence making the separation $\Delta R = \frac{2m}{p_T}$ bigger; on the other side, the decay is not anymore two-prong (two-sub-jet-like) but rather a three-prong (three-sub-jet-like) decay, one from the b-jet and the other two from the W decay. m^{TA} is here never performing better than m^{calo} , as can be seen e.g. in Figure 5.8, right.

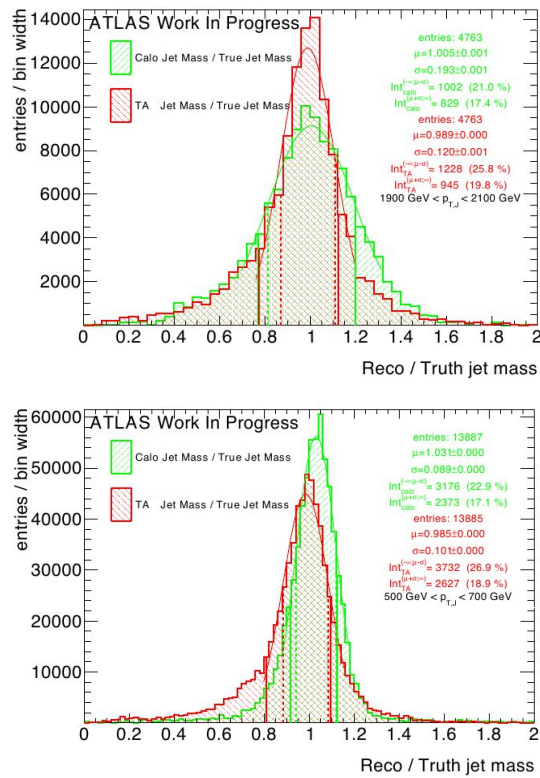


Figure 5.7: Mass response plots for selected ranges of p_T : on the bottom, a “low” range, $500 \text{ GeV} < p_T < 700 \text{ GeV}$, on the top an high p_T , $1900 \text{ GeV} < p_T < 2100 \text{ GeV}$. A difference in performance can be clearly seen.

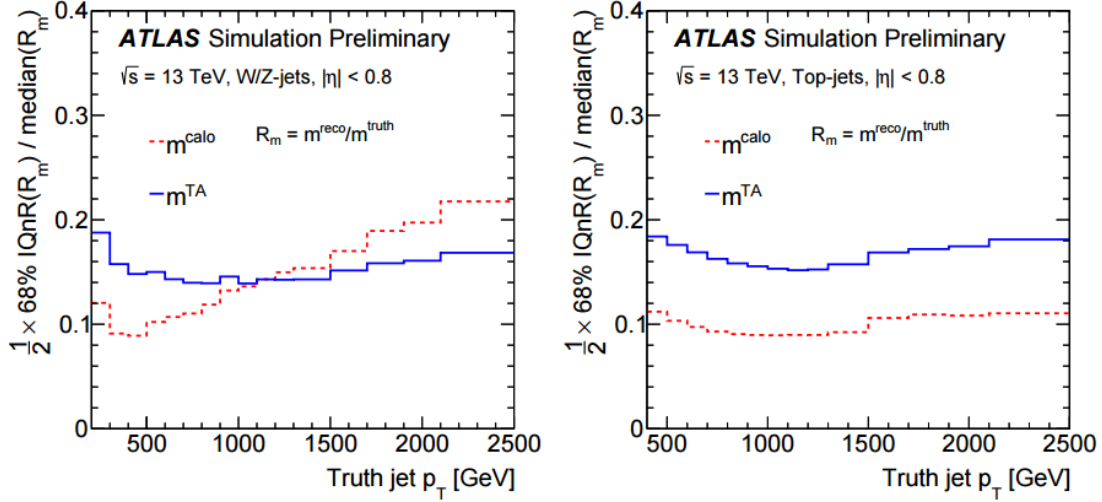


Figure 5.8: The comparison between the performance of m^{calo} and m^{TA} for W/Z jets (left) and top jets (right); on the x-axis the transverse momentum and on the y-axes the $\frac{1}{2} \times 68\%$ IQnR/median of the mass distribution, from [24]. A better observable has lower values on the y-axis.

Performance in $h \rightarrow b\bar{b}$ Decays

For boosted Higgs the m^{calo} outperforms the m^{TA} in the spectrum of transverse momentum. Although the decay is two-pronged, the mass of the Higgs is higher than the electroweak bosons, moreover another difference lays in light quarks initiated jets and heavy quarks initiated ones, like the b-quarks from Higgs decay.

5.5. The Track-Assisted Sub-jet Mass (m^{TAS})

In this section the main outcome of the work of this thesis is presented: the *track-assisted sub-jet mass* (m^{TAS}). The main idea takes inspiration from the track-assisted mass: if one can use the tracks to exploit the better angular resolution and correct the missing neutral component jet-by-jet, there is an additional information that can be used. The neutral fraction, in fact, varies stochastically not only per-jet basis, but even per-sub-jet basis, since each sub-jet is originated from a different quark. Correcting the missed neutral component per-sub-jet, it should perform better already at an intuitive level, as it accesses information from the jet substructure. There are few question in the definition of this mass observable, whose answers are in the next section:

- Regarding the inputs:

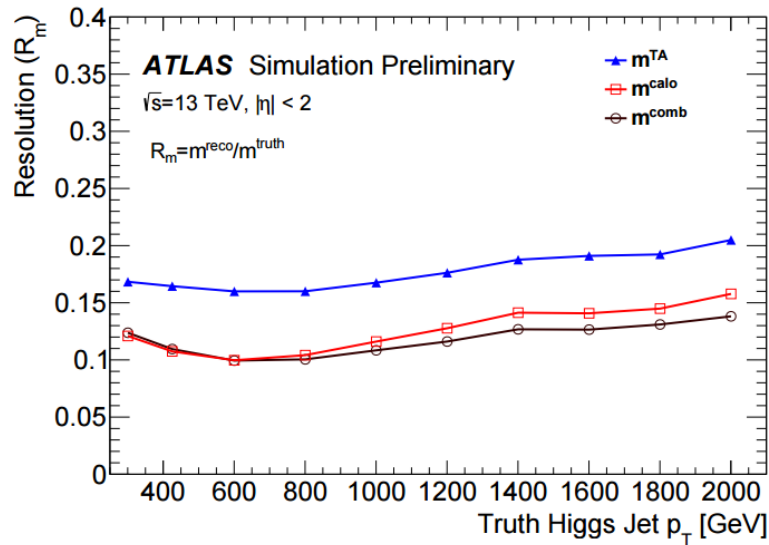


Figure 5.9: Performance of the m^{TA} with the boosted Higgs sample; the m^{TA} is the blue line, the m^{comb} will be described later in this chapter. From [25]. The FoM here is the resolution of the Response.

- How to select the set of tracks to be used?
- Which kind of sub-jet should be used?
- Regarding the procedure
 - How to associate the tracks to a sub-jet?
 - How to correct for the missed neutrals on a sub-jet basis?
 - How to add everything back together?

Those details are given in the next subsection.

5.5.1. Observable Definition: Inputs

There are two inputs to the m^{TAS} : the tracks and the sub-jets. The definition of the standard inputs are give here; alternative approaches are given in subsection 5.7.3.

Tracks

Only the tracks that satisfy the quality criteria and primary vertex association, described in the previous section 5.2, are used. The tracks taken additionally are required to be ghost associated to the sub-jets of the groomed jet; namely only the sub-jets which survived the trimming procedure and are described in the next

subsection. Ghost association provides a one-to-one correspondence to the sub-jets set, and was therefore chosen and preferred to other kind of assignments.

Sub-jets

The choice of sub-jets must follow a simple requirement: of course we want to take those which most likely come from the hard-scattering. This means that the choice of taking them after grooming is forced.

As grooming technique used, the trimming was preferred as being the standard in ATLAS and the most flexible one for optimization studies.

The standard version of the trimming uses the k_t reclustering algorithm with radius of 0.2, with the transverse momentum ratio f_{cut} at 5%.

As shown later, this is also the optimal configuration for sub-jets.

5.5.2. Observable Definition: Procedure

Having tracks and sub-jets now well defined, we can describe the recipe to produce the m^{TAS} . For brevity we will call the sub-jets SJ in the formulae below.

As said, the tracks are the one ghost-associated to the sub-jets; however, tracks which fall inside the area of the large- R jet, but not inside the sub-jets area, are still much probably coming from the hard-scattering. They are then associated again to the closest sub-jets via ΔR association.

Each sub-jet will have at this point some tracks associated via ghost-association and some other via ΔR (which are maximally 5%). We call this set of tracks, a “custom” Track-Jet or TJ.

At this point, the one-to-one correspondence is still preserved (for each SJ there is one and only one TJ), and we can move on correcting the neutral fraction.

Getting inspired from the formula $m^{TA} = p_T^{calo} / p_T^{track} \times m^{track}$, we would like to replicate this at sub-jet level, i.e.

$$m^{TAS} = \sum_{SJ} \frac{p_T^{SJ}}{p_T^{TJ}} \times m^{TJ}$$

Since now we are working inside the sub-jets we need to change the sub-jet’s 4-vector itself and not only the mass: if we call p_μ^{TJ} the Lorentz vector of the track-jet,

$$p_\mu^{TJ} = \begin{pmatrix} m^{TJ} \\ p_T^{TJ} \\ \eta^{TJ} \\ \phi^{TJ} \end{pmatrix} \rightarrow p_\mu^{TA} = \begin{pmatrix} m^{TJ} \times \frac{p_T^{SJ}}{p_T^{TJ}} \\ p_T^{SJ} \\ \eta^{TJ} \\ \phi^{TJ} \end{pmatrix}$$

where p_μ^{TA} is the track-assisted sub-jet's 4-vector. If we label i the i -th track-jet of the N ones present in the large- R jet,

$$m^{TAS} = \sqrt{\left(\sum_i^N p^{TA} \right)_\mu \left(\sum_i^N p^{TA} \right)^\mu}$$

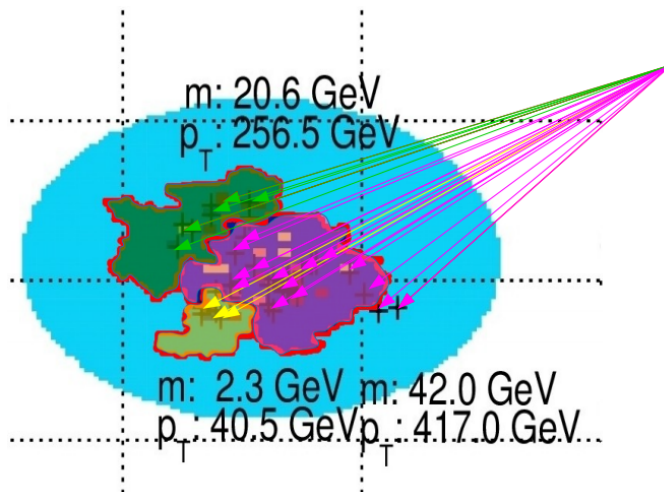


Figure 5.10: Pictorial event display showing the η ϕ region of a large- R jet, (in blue the catchment area of the anti- k_t) showing the different k_t sub-jets: they are highlighted in green, fuchsia and yellow. The associated track-jets (here as arrows pointing the calorimeter area) are colored with the same color of the correspondent sub-jet. Some tracks associated with ΔR procedure can be seen in the fuchsia sub-jet. The transverse momenta and mass values are also shown for the sub-jets.

An important remark is that, in the case of a large- R jet with only one sub-jet, the m^{TAS} has exactly the same definition of the m^{TA} . This implies, since the angular separation of the decay product scales inversely with p_T , that the performance should approach the one of the m^{TA} in the extreme kinematic regime. However, the space for improvement is precisely in the low-middle p_T regime, as seen in the m^{TA} section.

5.5.3. Performance in $W \rightarrow q'\bar{q}$ Decays

The boosted W/Z was the first one looked at, and with which the m^{TAS} was designed. The m^{calo} shows a fast deterioration of the performance at high p_T , and, as shown in the previous section, the m^{TA} prevents this deterioration but suffers at low transverse momenta ($p_T < 1$ TeV). The m^{TAS} has the same behavior in the extreme transverse momentum regime as the m^{TA} , since the sub-jet multiplicity peaks at one,

where there are no differences between the two observables. In the low- p_T regime, on the contrary, it exploits the different charged to neutral fluctuation, achieving a better performance. This is shown in Figure 5.11 as a function of p_T : below ~ 1 TeV it achieves lower values of the IQnR converging from below to the m^{TA} as the number of sub-jets decreases to one.

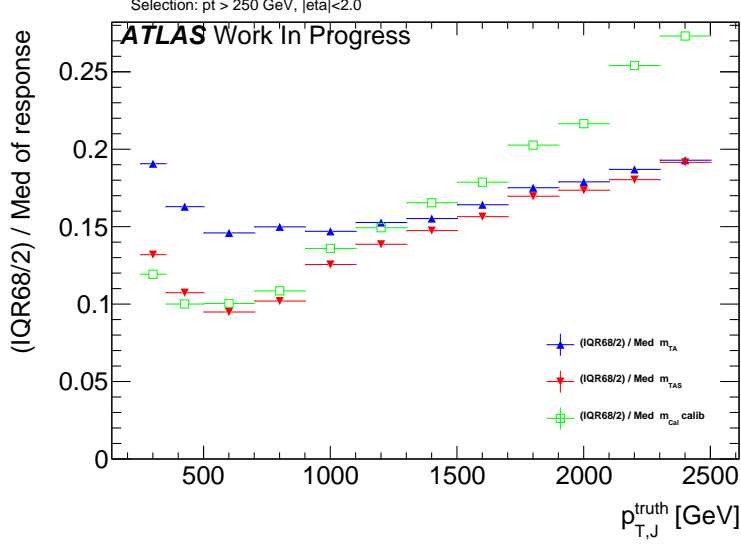


Figure 5.11: Performance of the m^{TAS} versus the m^{calo} and m^{TA} for the boosted W/Z sample.

5.5.4. Performance in $t \rightarrow q'\bar{q}b$ Decays

The boosted tops are shown on Figure 5.12; the m^{TAS} is comparable yet slightly worse than the m^{calo} in the low-middle p_T regime, while degrades at higher p_T approaching the m^{TA} , which is far beyond the track-assisted sub-jet mass in performance. As already noted, the worse performance can be ascribed both to the higher top-quark mass, and to its different and more complex decay topology.

5.5.5. Performance in $h \rightarrow b\bar{b}$ Decays

In the Randall-Sundrum graviton to di-Higgs to four b-quark, the performance is again problematic for the m^{TA} with respect to m^{calo} , which is far beyond the latter, while the performance of the m^{TAS} is partially similar to the boosted top-quark sample, but degrades much more in the extreme p_T regime, following the m^{TA} . Shown in Figure 5.13.

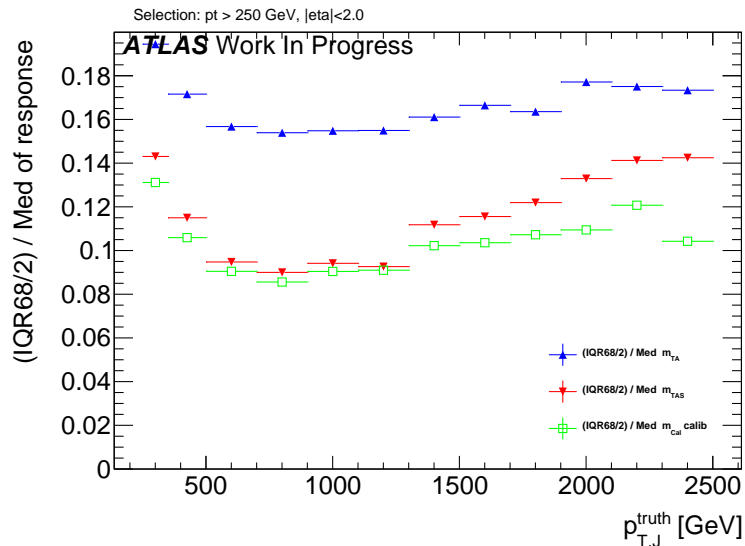


Figure 5.12: Performance of the m^{TAS} versus the m^{calo} and m^{TA} for the boosted top sample.

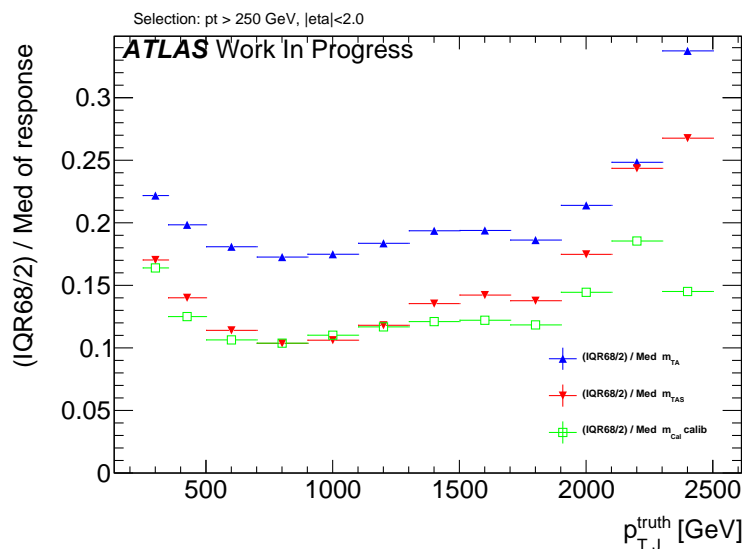


Figure 5.13: Performance of the m^{TAS} versus the m^{calo} and m^{TA} for the boosted Higgs sample.

5.5.6. Performance in QCD Multijet Events

The behavior of the QCD multijet sample is similar to the boosted W/Z sample, where the m^{TA} exhibits a crossing point in the middle-low regime $p_T \simeq 900$ GeV and proceeds with a better performance at high transverse momenta. Again the m^{TAS} follows this similarity showing no crossing point and an optimal overall behavior, both with respect to calorimeter- and track-assisted-based mass definition.

On Figure 5.14.

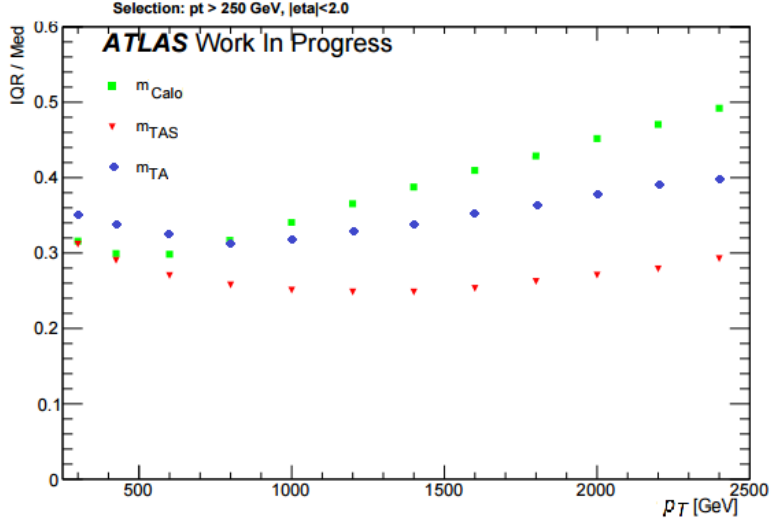


Figure 5.14: Performance of the m^{TAS} versus the m^{calo} and m^{TA} for the QCD multijet. Here shown IQR/Med not $\frac{1}{2} \times 68\%$ IQnR/median.

5.5.7. Performance in Massive $\tilde{W} \rightarrow q'\bar{q}$ Decays with $m_{\tilde{W}} = m_t$

The massive W sample is a special sample which was used to understand the behavior of the boosted tops, whether its worse resolution was coming from the higher mass of the top quark or from the more complex decay topology (three-pronged instead of two-pronged decay and b-quark presence). The sample is almost identical to the boosted W/Z one ($W' \rightarrow WZ$) but in this case the SM electroweak boson are set to have the mass of the top quark $m_{\tilde{W}} = m_t$. In fact, from the rule $\Delta R = 2m/p_T$, a bigger separation is expected between the quark from the hadronic decay. The comparison with m^{calo} is shown in Figure 5.15, together with the boosted top-quark for comparison. As seen here, the performance of the latter is clearly worse than the former, the trend is yet very similar. This difference is interpreted in terms of different and more complex topology and hence higher sub-jet multiplicity: in the three sub-jet structure, resolving accurately the components is more challenging.

5.6. Other Stability Quantifiers

The stability of the m^{TAS} was checked, although the IQnR is already a good quantifier of stability, explicitly for the mean of the mass response distribution and for the left-hand-side tail, as a function of the transverse momentum. This was an

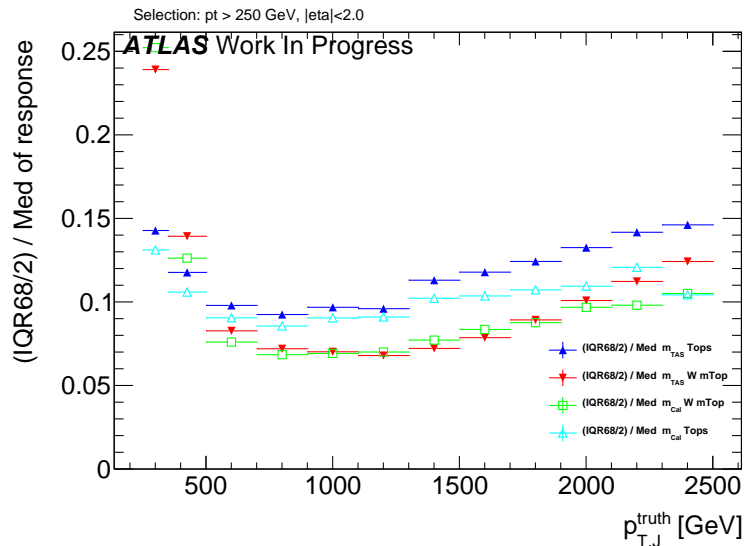


Figure 5.15: Performance of the m^{TAS} versus the m^{calo} for the massive W/Z (in red and green); shown on the same plot also the boosted top sample (in blue and light blue).

important check to assure the overall gaussianity of the final distribution in the whole spectrum of p_T , and suitability in regards of the calibration step, which is not discussed in this thesis.

The mean of the response distribution is shown for boosted W/Z decays in Figure 5.16, left; as seen here, despite being the mean constantly below the unity, its behavior is much more flat and independent of p_T , especially in the low-middle regime. This is surprising since the m^{calo} is already shown after the calibration step, which is not taken instead for the m^{TAS} . Conversely the left-hand-side tail of the mass response which is shown in the same figure, right, shows a more enhanced behavior than the m^{calo} , but still never reaches the 10%. Of course an enhancement of the tail causes a loss of gaussianity and a number of jets which are reconstructed with a lower mass than they should, but it is still comparable with the calorimeter mass.

Those quantifiers show analogous behavior for the other samples considered and those figures can be found in the Appendix.

5.7. Sub-jet Calibration

An additional attempt of calibrating the sub-jet was also tried and, although the results were not substantially improved, it is presented in this section. This study

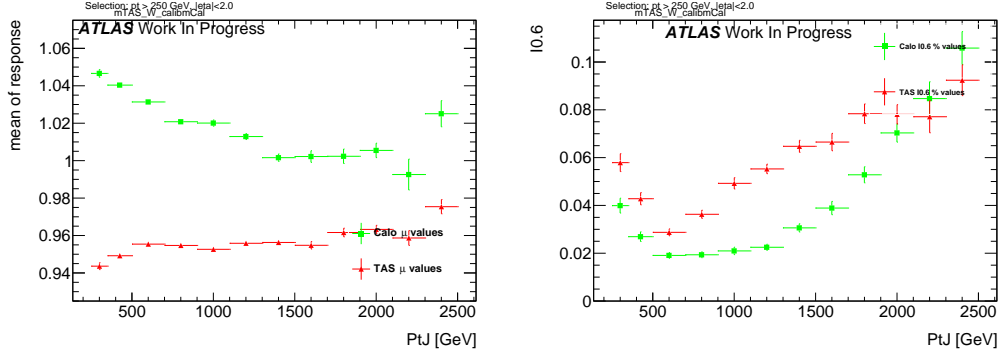


Figure 5.16: Stability quantifiers which were checked for the m^{TAS} : mean, on the left, and normalized left-hand side integral, on the right, of the mass response distribution. The mean is calculated from a Gaussian fit and the integral goes from 0 to 0.6.

was performed using only boosted W/Z samples.

5.7.1. Preliminary Studies on Sub-jet Calibration

The first attempt in calibrating the sub-jets had as start a “perfect calibration”, which means using the truth-level information from the MC sample *before* the interaction with the calorimeter. Truth-level tracks are the particles in the jet which have an electric charge and are stable, truth-level sub-jets are all the particles, charged and not, which are ghost associated to the calorimeter sub-jets. There are few possibilities in doing so, here some nomenclature for this study will be introduced:

- m^{TAS} using truth-level sub-jets and tracks; normal tracks (with all detector effects) are used to assist the truth-level sub-jets;
- m^{TAS} using truth-level tracks and truth-level sub-jets; the truth-level tracks are used to assist the truth-level sub-jets;
- m^{calo} truth, calculated using only the truth sub-jets.

Perfect Calibration

The *perfect calibration* refers to the procedure of using m^{TAS} with truth-level sub-jets and track, i.e. looking at the best possible scenario with an ideal detector. The performance is of course expected to be optimal, because of the use of the truth-level. This step was necessary as feasibility study, to understand whether ulterior efforts in this direction were meaningful. The perfect calibration is shown in Figure 5.17; since

the performance exhibits room for big improvement below ~ 1 TeV and moderate to small improvement above this value, the second step of a simple calibration was tried.

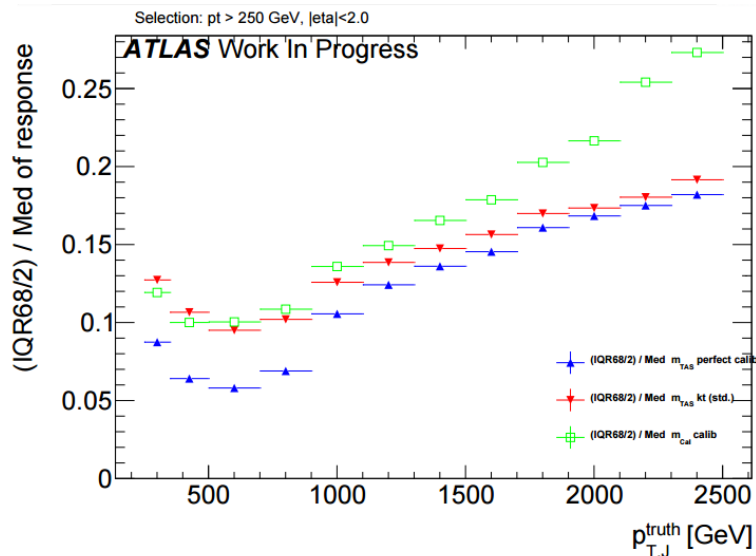


Figure 5.17: Performance of the perfect calibration. It shows room for improvement especially at low-middle p_T .

Simple Sub-jet Calibration

Following the example of calibration of jets in general, a simple approach to emulate this procedure was tried, constructing in various bins of transverse momenta the responses of the sub-jet's energy to derive the weights factors to be applied. The detailed procedure is as follows:

1. Responses in energy $R_E = E^{reco}/E^{truth}$ were built in several bins of p_T , spanning to the whole transverse momentum range;
2. The mean μ_R of this response was calculated via a fit to the Gaussian core;
3. Those values (*scale factors*) were stored and applied again to the sub-jets before the computation of the m^{TAS} via 4-momentum correction $E' = E/\mu_R$; the p_T (the value which only enters the m^{TAS} variable) was changed then correspondingly to keep the sub-jet's mass constant.

This procedure was called *poor man's calibration* or PM calibration or *simple calibration*. A check on the p_T response before and after calibration together with

the mean of the entire Large- R jet response is shown in Figure H.11 and H.12 in Appendix.

The results are on Figure 5.18; there are only marginal improvements in few ranges of low transverse momentum where the scale factors are further away from unity, and the overall observable is not performing better than the standard m^{TAS} . This is interpreted both in terms of a missing calibration as a function of the η variables (having hence a benefit from the crack region) and because the correction done on average does not provide the sufficient handle in a jet-by-jet basis, especially when all the sub-jets are rescaled by similar factors (which translates into a similarity of p_{TS} of the sub-jets, often the case for e.g. boosted W/Z , less for boosted tops entirely contained in the large- R jet).

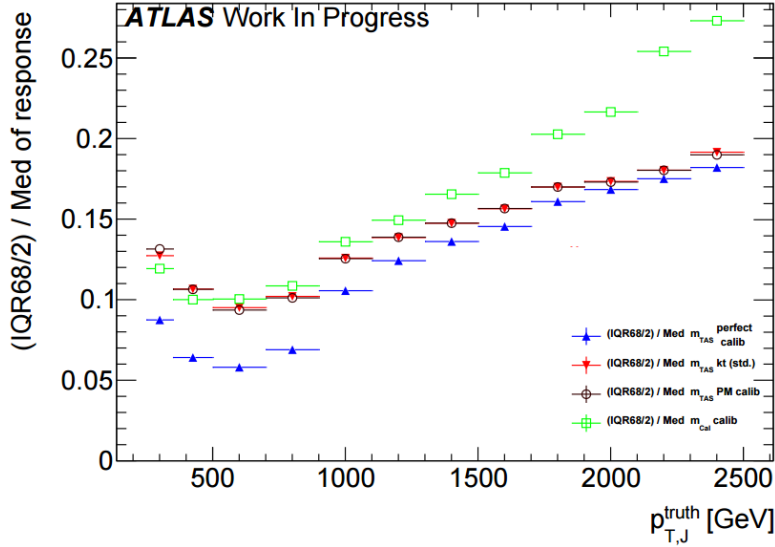


Figure 5.18: Performance of the poor man's calibration. The improvement is marginal throughout the entire transverse momentum space.

5.7.2. Limitation of m^{TAS}

The final effort to understand the various and competing effects, which take place in the m^{TAS} and which was inspired by the perfect calibration procedure, brought to a final study on the variable to understand the reason for the worsening of the resolution at high transverse momenta, using again the truth MC information.

The preliminary investigation in this direction was then the study on the track-resolution: since the track relative resolution of the transverse momentum is expected to worsen linearly with this variable, a response of the mass of the tracks was constructed, using the truth-level tracks.

The result is shown on Figure 5.19: for the samples considered, it shows a linear degradation of the mass of the tracks, both for massive and SM W/Z .

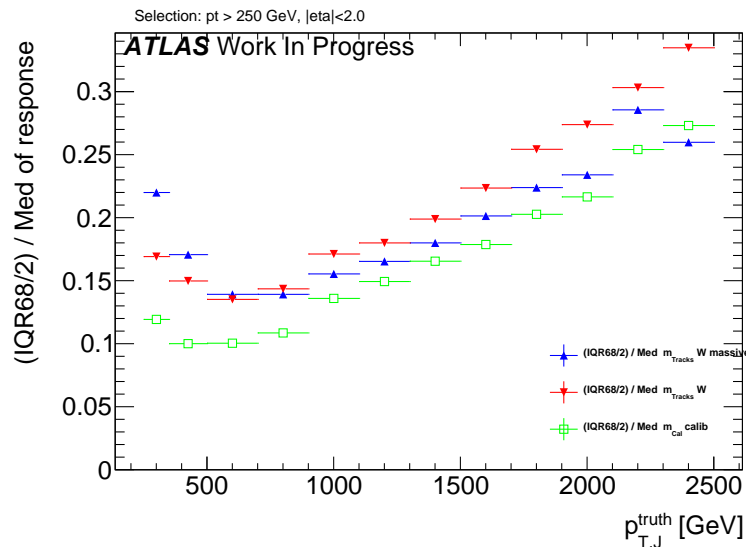


Figure 5.19: The performance of the track mass in blue and red for massive W sample and boosted W/Z respectively; for reference in green the calorimeter mass of the large- R jet.

The hypothesis of the degradation of the m^{TAS} driven by the tracks is also supported by the Figure H.13 in Appendix, where the truth-level tracks are used instead of real tracks to compute the variable; it can be seen the flat behavior at high p_T , hence ascribing the worsening of the resolution to tracks at higher transverse momenta.

A complete breakdown of the variable in terms of truth-level particles is given in Figure 5.20, where all the different components are separated. In particular the black dots show the m^{TAS} using truth-level sub-jets but real tracks for the track assistance procedure. Even combining this truth-level information, in fact, it shows a large worsening of the performance (truth-level sub-jets only are shown as blue dots).

Other results using truth-level information on boosted tops are shown and described in the Appendix.

5.7.3. Alternative Observable Definitions

There are quite a few ways to modify the track-assisted sub-jet mass; however, all the alternative approaches showed worse performance, and they are mentioned here for completeness only.

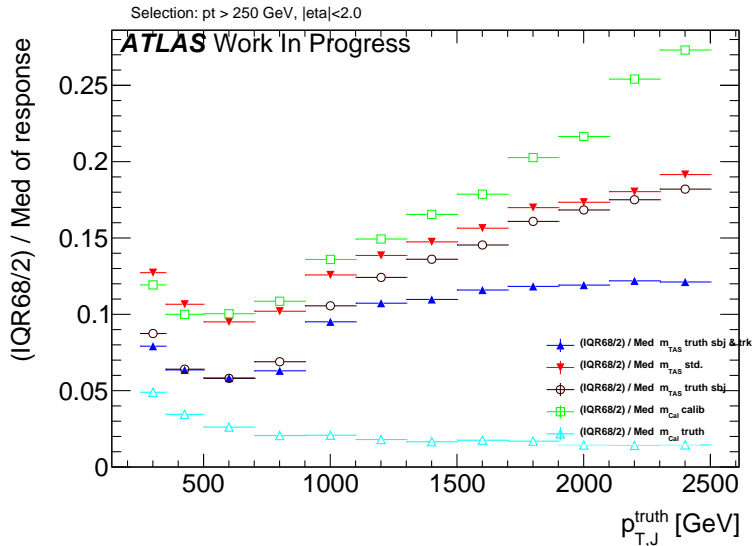


Figure 5.20: Breakdown of the m^{TAS} in its component using truth-level information for boosted W/Z decays.

Alternatives considered were:

- for the tracks:
 - use of tracks not as input directly, but only taking those belonging to anti- k_t reclustered track-jet with radius of 0.3 or 0.2;
 - tighter or looser quality conditions were explored;
 - tighter or looser primary vertex association requirement were explored.
- for the sub-jets:
 - the trimming procedure was modified: various radii R_{sub} of the sub-jets were tested;
 - the sub-jets were reclustered using not only the standard k_t , but also anti- k_t and C/A.
- for the procedure: different 4-momentum correction scheme was also explored.

The different reclustering algorithm choice has a deep impact and was studied in details, since it changes the topo-cluster added to the sub-jets and the tracks associated to them. The situation is depicted in the event-display in Figure 5.21; the display on the left shows the standard choice of k_t , the one on the right shows the modified approach anti- k_t .

In the Appendix, figure H.6 H.7 H.8 the performance for boosted W/Z , tops and Higgs are shown, respectively. It can be seen that the k_t algorithm provides

the best observable definition, in all the samples considered. However, the anti- k_t algorithm provides similar performances; this was an important check as the jet calibration procedure currently going on in ATLAS, the R -Scan procedure includes the anti- k_t algorithm with radius of $R=0.2$ and aims at providing the calibration and uncertainties that could be used directly in the computation of the m^{TAS} .

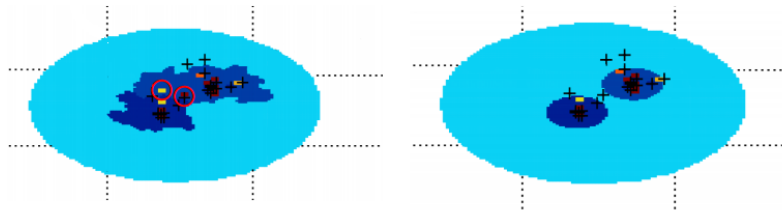


Figure 5.21: An example of event-display shows the differences in the reclustering algorithm used for the sub-jets: on the right k_t and on the left anti- k_t . Highlighted some constituents trimmed away with the second choice.

5.8. Combined Track and Calorimeter Mass

Since the calorimeter large- R jet mass is not explicitly used in the track-assisted (sub-jet) mass, it may be possible to improve the performance creating a new observable which combines both mass definitions.

This is true for both the m^{TA} and the m^{TAS} ; they are introduced in the next subsections. Provided that the two observables are nearly independent (correlation coefficient are $\sim 10\%$, see Figure H.9 in the Appendix), due to the Gaussian nature of the p_T and mass response, the optimal combination of the two is linear¹. An example is provided in Figure 5.22.

¹If the joint distribution of the responses is Gaussian, then one can write their probability distribution function as $f(x, y) = h(x, y) \times \exp[A(\mu) + T(x, y)\mu]$, where x is the calorimeter-based jet mass response, y is the track-assisted jet mass response, μ is the common average response, and h, A, T are real-valued functions. This form shows that the distribution is from the exponential family and therefore T is a sufficient statistic. Since the natural parameter space is one-dimensional, T is also complete. Therefore, the unique minimal variance unbiased estimator of μ is the unique unbiased function of $T(x, y) = x/\sigma_x^2 \times +y/\sigma_y^2$. See e.g. Ref. [34] and [24] for details.

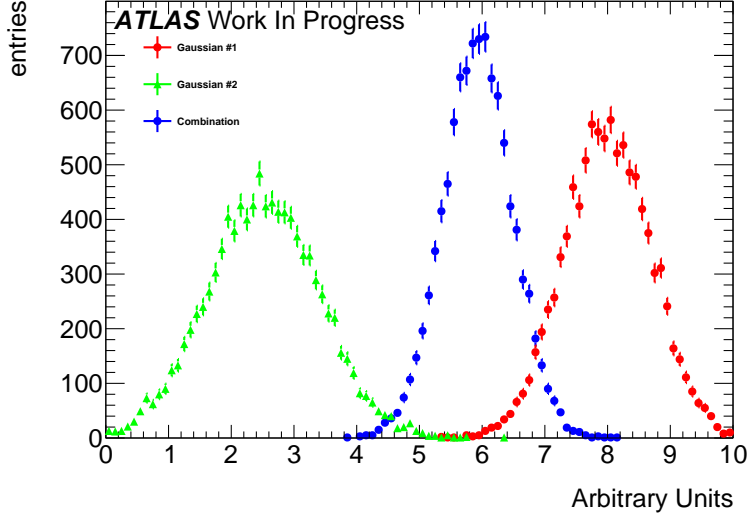


Figure 5.22: A toy example of the combination of two independent Gaussian observables, in red and green, and their combination, in blue. It can be seen that the combination has a smaller width.

5.8.1. Combination $m^{TA} - m^{calo}$

For the $m^{TA} - m^{calo}$ combination the observables are considered nearly independent, then

$$m^{comb} = a \times m^{calo} + b \times m^{TA}, \quad (5.2)$$

$$a = \frac{\sigma_{calo}^{-2}}{\sigma_{calo}^{-2} + \sigma_{TA}^{-2}} \quad b = \frac{\sigma_{TA}^{-2}}{\sigma_{calo}^{-2} + \sigma_{TA}^{-2}}$$

where σ_{calo} and σ_{TA} are the m^{calo} 's and m^{TA} 's resolution functions. The m^{comb} then is the $m^{TA} - m^{calo}$ combination.

5.8.2. Combination $m^{TAS} - m^{calo}$

There is a main difference between the m^{TAS} and m^{TA} when it comes to combination: since the m^{TAS} is using sub-jet level information but m^{TA} not, the correlation with the m^{calo} is expected to be higher. This can be seen e.g. in the plots in Figure 5.23 (additional plots shown in Figure H.10 in Appendix), where the correlation is not only higher for the simple W/Z and Higgs jets, but above 50% for tops. The assumption of independent variables here falls, forcing a more complete approach.

The Ansatz is to take into account the correlation via the formula:

$$m_{TAS}^{comb} = w \times m^{calo} + (1 - w) \times m^{TAS},$$

$$w = \frac{\sigma_{TAS}^2 - \rho\sigma_{calo}\sigma_{TAS}}{\sigma_{calo}^2 + \sigma_{TAS}^2 - 2\rho\sigma_{calo}\sigma_{TAS}} \quad (5.3)$$

where now m_{TAS}^{comb} is the new $m^{TAS} - m^{TA}$ combination. This expression reduces then to the form:

$$m_{TAS}^{comb} = a \times m^{calo} + b \times m^{TAS},$$

$$a = \frac{\sigma_{TAS}^2 - \rho\sigma_{calo}\sigma_{TAS}}{\sigma_{calo}^2 + \sigma_{TAS}^2 - 2\rho\sigma_{TAS}\sigma_{calo}} \quad b = \frac{\sigma_{calo}^2 - \rho\sigma_{calo}\sigma_{TAS}}{\sigma_{calo}^2 + \sigma_{TAS}^2 - 2\rho\sigma_{TAS}\sigma_{calo}} \quad (5.4)$$

which reduces to equation (5.2) after simple algebra for the case when $\rho = 0$. Of course, this value can be set to the value of the specific sample considered, or to an average of 0.3 if one wants to give a definition generally valid for all the cases considered; in this case, the performance would be slightly sub-optimal.

Procedure

The procedure of producing the m_{TAS}^{comb} is defined as follows:

1. For the given sample, the m^{TAS} and m^{calo} are produced;
2. The mass responses are also produced for the given ranges of p_T ;
3. For each of these responses, the value of the IQnR as defined previously is calculated and stored;
4. The average correlation factor of 0.3 is assumed;
5. With the formula 5.3, m_{TAS}^{comb} is calculated using the m^{TAS} , m^{calo} and the values stored from before.

A remark on the procedure: the step 3. uses values of the IQnR because this was showed to be a more robust way to look at the response and fit-independent. For step 4. the correlation factor was decided to be an average of the samples considered.

Additionally, the IQnR weights are produced for each sample specifically. In order to give a sample-independent definition of the m_{TAS}^{comb} , following also the procedure adopted for the m^{comb} , these weights could be taken from a QCD multijet sample and applied indiscriminately to the particular case. Here of course the performance would be again sub-optimal, since the variable was not developed in an ad-hoc way.

Throughout the results presented in the following sections, both observables were calculated with ad-hoc weights. Quantitative statements between them would still hold in the case of QCD weights. However, when confronting e.g. m^{TAS} with them it has to be kept in mind that in this case their performance is overestimated, since this choice, although being more general, would perform slightly worse.

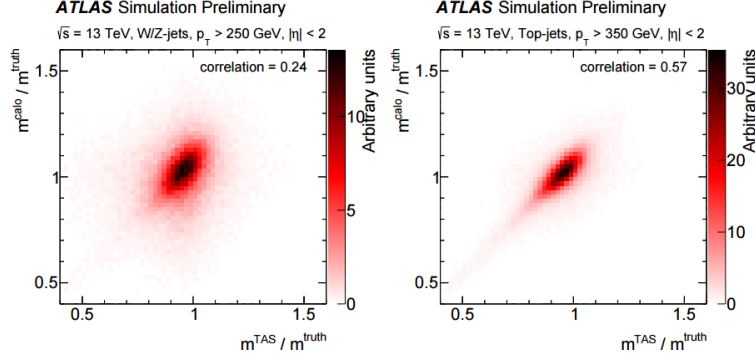


Figure 5.23: The calorimeter based jet mass mass response versus the track-assisted sub-jet mass response, on the left for boosted W/Z on the right for boosted tops.

5.8.3. Performance in $W \rightarrow q'\bar{q}$ Decays

On the boosted W/Z s sample, the performance of the m_{TAS}^{comb} outperforms all the other definitions throughout all the transverse momentum space; on Figure 5.24 they are shown for reference together with the m^{TAS} . It can be noted here that the track-assisted sub-jet mass, although being sub-optimal, has comparable performance, yet presenting fewer complications due to the combination procedure.

5.8.4. Performance in $t \rightarrow q'\bar{q}b$ Decays

The boosted top sample remains the most challenging one also with the combined mass; as seen on Figure 5.25, the m^{comb} performs quite similarly to the calorimeter based mass definition, yet behaving considerably better than the m^{TAS} especially at high transverse momentum. The m_{TAS}^{comb} , however, outperforms all the other definitions, and shows its optimal observable strength at middle p_T i.e. in the range $1 < p_T < 1.6$ TeV.

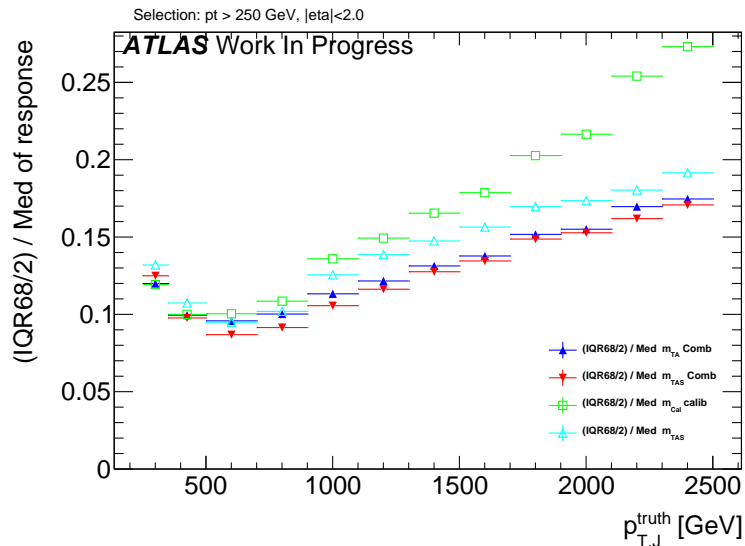


Figure 5.24: Performance of the combined mass on W/Z samples; here shown the two definitions of the combined mass, m^{comb} and m_{TAS}^{comb} , together with the calorimeter mass and the track-assisted sub-jet mass.

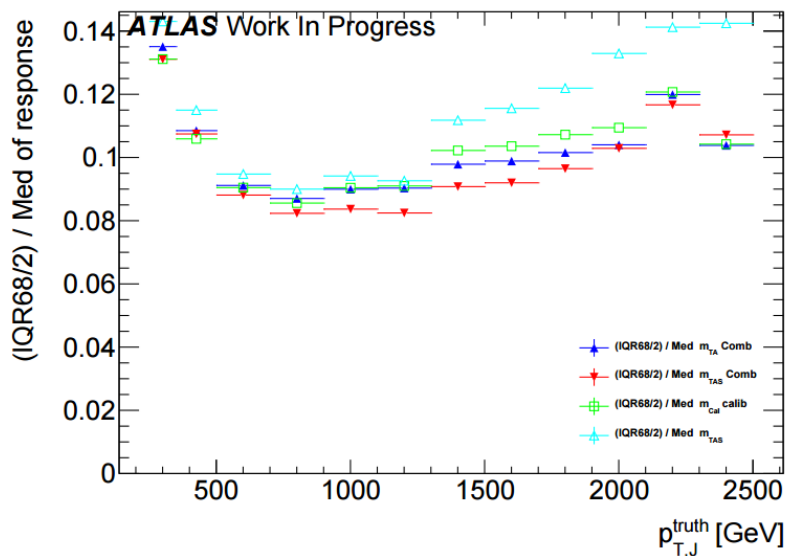


Figure 5.25: Performance of the combined mass on the top sample; here shown the two definitions of the combined mass, m^{comb} and m_{TAS}^{comb} , together with the calorimeter mass and the track-assisted sub-jet mass.

5.8.5. Performance in $h \rightarrow b\bar{b}$ Decays

Again, for the Higgs decay there are similarities as for the top sample; on Figure 5.26 the two definitions of the combined mass, together with the simpler m^{TAS} . Although this variable is lightly sub-optimal yet still comparable in the low to intermediate

range in transverse momenta, where the tracks are driving a decrease in performance for the high to very-high p_T . The m_{TAS}^{comb} uses this advantage to achieve optimal behavior in the entire transverse momentum spectrum, outperforming both m^{calo} and m^{comb} almost everywhere.

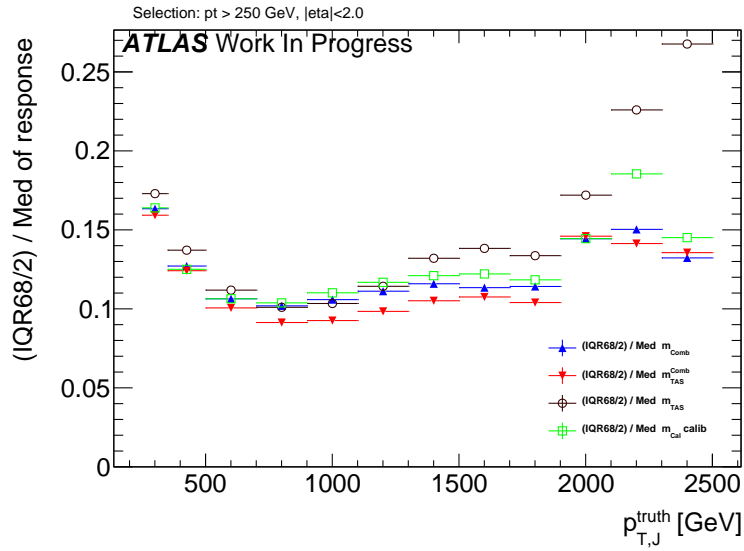


Figure 5.26: Performance of the combined mass on the Higgs decay; here shown the two definitions of the combined mass, m^{comb} and m_{TAS}^{comb} , together with the calorimeter mass and the track-assisted sub-jet mass.

6. Conclusion and Outlook

The m^{TAS} was demonstrated to a simple, robust and powerful observable; this chapter draws a few lines of conclusion to this thesis and the outlook for these studies.

6.1. Conclusion

The m^{TAS} variable was developed for the large- R jet mass; it combines the information of the tracker- and calorimeter-system to achieve an higher precision in the jet mass reconstruction, correcting the missed neutral fraction which is absent in the tracker but not in the calorimeter. With respect to the m^{TA} , it applies this correction at sub-jet by sub-jet level and not at jet by jet level, therefore providing a more accurate reconstruction. It was shown in Monte Carlo simulation to be a very good observable confronting quantitatively with the other definitions which are either standard or in preparation, m^{calo} , m^{TA} and m^{comb} . In fact, it behaves better in terms of $\frac{1}{2} \times 68\%$ IQnR/median and all the other ways to look at the figure of merit, the mass response, for the boosted W/Z and QCD sample; is always better than the m^{TA} and similar to the m^{calo} for the boosted tops and Higgs. Moreover, it is a slightly worse observable than the m^{comb} , yet being comparable, and avoiding the development of ad-hoc weights. The optimal configuration of m^{TAS} is shown and confronted with different approaches, in particular in terms of different trimming procedure of the large- R jet to be used as an input. All the components of the observable have been studied with the use of truth Monte Carlo information without detector effect, in order to evaluate quantitatively its limits and strengths; the track p_T measure degradation was found to be the cause of the variable decreasing performance at higher transverse momenta.

The m_{TAS}^{comb} is the logical extension of the m^{TAS} , which improves by construction the results beyond the m^{calo} and the m^{TAS} , combining these two variables on the same way of the m^{comb} , but taking into account the higher correlation factor which

is inherited from the sub-jet usage. Weights for its construction can be in both cases either derived specifically for the sample considered, or constructed on average with the QCD sample, in this case getting a sub-optimal performance. In all the cases studied, it has a better behavior than the m^{comb} , m^{calo} and m^{TA} .

For the very conclusion, both the variables constructed in the work of this thesis, m^{TAS} and m_{TAS}^{comb} , exhibit a better performance of their counterparts, m^{TA} and m^{comb} , which are now ready to be use or in preparation within the ATLAS collaboration, and share the same advantages -and disadvantages. Further steps are necessary to get this observables to usage: calibration and uncertainties.

6.2. Outlook

The outlook of the m^{TAS} and m_{TAS}^{comb} variables follows two main scenarios, concerning the calibration and uncertainties determination which are necessary to get this observables ready to be used. The procedure involved are already fully understood, since the the same was applied or is being applied for the m^{TA} and m^{comb} .

6.2.1. Calibration

For the simple scenario here the procedure that would take place is the direct Monte Carlo calibration of the m^{TAS} , aiming at correcting the reconstructed jet mass to the particle-level jet mass by applying the calibration factors derived from QCD multijet events, an analogous procedure to the one described in Section 4.2 for the jet energy scale.

The more complex scenario considers an additional calibration to the sub-jets with $R=0.2$, which is already at an advanced stage within ATLAS for anti- k_t reclustering algorithm (it has a slightly worse performance than k_t , as presented previously).

6.2.2. Uncertainties

The uncertainties are expected to be similar to the one which were derived for the m^{TA} and which are compared to the m^{calo} on Figure 5.6; the tracking uncertainties are smaller for the track-assisted mass because of the ratio m^{track}/p_T^{track} and will be smaller as well for the track-assisted sub-jet mass since it uses the same ratio.

In-situ uncertainties were derived for the m^{TA} with a sample of enriched top-quark; the same technology used here can be applied to the m^{TAS} .

In the more complex scenario, the uncertainties could be derived for the sub-jets $R=0.2$ reclustered with anti- k_t .

Bibliography

- [1] Particle Data Group Collaboration, K. Olive *et al.*, *Review of Particle Physics*, Chinese Physics C 38 (2014) 090001.
- [2] Paul Langacker, *The Physics of Heavy Z Gauge Bosons*. In: Rev. Mod. Phys. 81 (2009), pp. 1199–1228. doi: 10.1103/RevModPhys.81.1199. arXiv: 0801.1345 [hep-ph].
- [3] Martin Schmaltz and Christian Spethmann, *Two Simple W' Models for the Early LHC*. In: JHEP 07 (2011), p. 046. doi: 10.1007/JHEP07(2011)046. arXiv: 1011.5918 [hep-ph].
- [4] Georges Aad *et al.* *Combination of searches for WW, WZ, and ZZ resonances in pp collisions at $\sqrt{s} = 8$ TeV with the ATLAS detector*. In: Phys. Lett. B755 (2016), pp. 285–305. doi: 10.1016/j.physletb.2016.02.015. arXiv: 1512.05099 [hep-ex].
- [5] The CMS Collaboration, *Search for massive resonances decaying into pairs of boosted bosons in semi-leptonic final states at $\sqrt{s} = 8$ TeV*, CERN-PH-EP/2013-037 2014/09/03 arXiv:1405.3447v2 [hep-ex].
- [6] C. Patrignani *et al.*, Particle Data Group, Chin. Phys. C, 40, 100001 (2016). <http://pdg.lbl.gov/2015/reviews/rpp2015-rev-wprime-searches.pdf>
- [7] C. Patrignani *et al.*, Particle Data Group, Chin. Phys. C, 40, 100001 (2016). <http://pdg.lbl.gov/2015/reviews/rpp2015-rev-zprime-searches.pdf>
- [8] L. Randall and R. Sundrum, *A Large Mass Hierarchy from a Small Extra Dimension*, Phys. Rev. Lett. 83 (1999) 3370, arXiv: hep-ph/9905221.
- [9] H. Davoudiasl, J.L. Hewett and T.G. Rizzo, *Warped Phenomenology*, Stanford Linear Accelerator Center Stanford CA 94309, USA, arXiv:hep-ph/9909255v1 6 Sep 1999.

- [10] ATLAS Collaboration, *ATLAS detector and physics performance: Technical Design Report, 1 & 2*, Tech. Rep. ATLAS TDR 14, CERN/LHCC 99-14, Geneva, 1999.
- [11] L. Evans and P. Bryant, *LHC Machine*, JINST 3 (2008) S08001.
- [12] C. Patrignani *et al.*, Particle Data Group, Chin. Phys. C, 40, 100001 (2016). <http://pdg.lbl.gov/2010/reviews/rpp2010-rev-qcd.pdf>
- [13] The CMS Collaboration, *Measurement of the inclusive 3-jet production differential cross section in proton-proton collisions at 7 TeV and determination of the strong coupling constant in the TeV range*, CERN-PH-EP/2013-037 2015/05/04 arXiv:hep-ph/14121633.
- [14] The ATLAS Collaboration, *Improved luminosity determination in pp collisions at $\sqrt{s} = 7$ TeV using the ATLAS detector at the LHC*, Eur. Phys. J. C (2013) 73: 2518. doi:10.1140/epjc/s10052-013-2518-3.
- [15] W. Bartel *et al.* [JADE Collaboration], *Observation of Planar Three Jet Events in $e + e -$ Annihilation and Evidence for Gluon Bremsstrahlung*, Phys. Lett. B 91, 142 (1980).
- [16] Ahmed Ali (DESY), Gustav Kramer (Univ. Hamburg), *Jets and QCD: A Historical Review of the Discovery of the Quark and Gluon Jets and its Impact on QCD*, arXiv:1012.2288v2 [hep-ph].
- [17] Matteo Cacciari, Gavin P. Salam, Gregory Soyez, *The anti- k_t jet clustering algorithm*, arXiv:0802.1189v2 [hep-ph].
- [18] F. Halzen, A.D. Martin and D.M. Scott, Phys. Rev. D25 (1982) 754, Phys. Lett. B112 (1982) 160.
- [19] Torbjorn Sjostrand, *Monte Carlo Generators*, hep-ph/0611247, CERN-LCGAPP-2006-06.
- [20] W. Lampl *et al.*, *Calorimeter Clustering Algorithms: Description and Performance*, ATL-LARG-PUB-2008-002.
- [21] The ATLAS Collaboration, *Jet energy resolution in proton-proton collisions at $\sqrt{s} = 7$ TeV recorded in 2010 with the ATLAS detector*, CERN-PH-EP-2012-191 arXiv:1210.6210v1 [hep-ex].

-
- [22] GEANT4 Collaboration (S. Agostinelli *et al.*), *GEANT4: A Simulation toolkit*, Nucl.Instrum.Meth. A506 (2003) 250-303 DOI: 10.1016/S0168-9002(03)01368-8 SLAC-PUB-9350, FERMILAB-PUB-03-339.
- [23] Ariel Schwartzman, *Jet energy calibration at the LHC*, SLAC National Accelerator Laboratory, 2575 Sand Hill Road Menlo Park, California 94025, USA, arXiv:1509.05459v1 [hep-ex] 17 Sep 2015.
- [24] The ATLAS Collaboration, *Jet mass reconstruction with the ATLAS Detector in early Run 2 data*, ATLAS-CONF-2016-035 19 July 2016.
- [25] The ATLAS Collaboration, *Boosted Higgs ($\rightarrow b\bar{b}$) Boson Identification with the ATLAS Detector at $\sqrt{s} = 13$ TeV*, ATLAS-CONF-2016-039 30th July 2016.
- [26] The ATLAS Collaboration, *Search for high-mass diboson resonances with boson-tagged jets in proton-proton collisions at $\sqrt{s} = 8$ TeV with the ATLAS detector*, arXiv:1506.00962v3 [hep-ex].
- [27] The CMS Collaboration, *Combination of searches for WW, WZ, ZZ, WH, and ZH resonances at $\sqrt{s} = 8$ and 13 TeV*, CMS PAS B2G-16-007.
- [28] The ATLAS Collaboration, *Search for heavy particles decaying to pairs of highly-boosted top quarks using lepton-plus-jets events in proton-proton collisions at $\sqrt{s} = 13$ TeV with the ATLAS detector*, ATLAS-CONF-2016-014.
- [29] The ATLAS Collaboration, *Search for resonances with boson-tagged jets in 15.5 fb⁻¹ of p-p collisions at $\sqrt{s} = 13$ TeV collected with the ATLAS detector*, ATLAS-CONF-2016-055.
- [30] The ATLAS Collaboration, *Search for pair production of Higgs bosons in the $b\bar{b}b\bar{b}$ final state using proton proton collisions at $\sqrt{s} = 13$ TeV with the ATLAS detector*, ATLAS-CONF-2016-049.
- [31] The ATLAS Collaboration, *Performance of jet substructure techniques for large-R jets in proton-proton collisions at $\sqrt{s} = 7$ TeV using the ATLAS detector*, CERN-PH-EP-2013-069 arXiv:1306.4945 [hep-ex].
- [32] Oleg Zenin, on behalf of the ATLAS Collaboration, *Soft QCD and underlying event measurements at ATLAS*, Nuclear and Particle Physics Proceedings Volumes 273275, April-June 2016, Pages 2053-2058 37th International Conference on High Energy Physics (ICHEP).

- [33] Page title: JetSubstructureECFA2014 At-
lasPublic TWiki Website name: Twiki.cern.ch
URL:<https://twiki.cern.ch/twiki/bin/view/AtlasPublic/JetSubstructureECFA2014>
Access date: 27th October 2016.
- [34] E. Lehmann and G. Casella, *Theory of Point Estimation*, Springer Verlag, 1998, isbn: 0387985026.
- [35] M. Son, C. Spethmann and B. Tweedie, Diboson-Jets and the Search for Resonant Zh Production, JHEP 08 (2012) 160, arXiv: 1204.0525 [hep-ph]
- [36] A. Katz, M. Son and B. Tweedie, Jet Substructure and the Search for Neutral Spin-One Resonances in Electroweak Boson Channels, JHEP 03 (2011) 011, arXiv: 1010.5253 [hep-ph]
- [37] S. Schaetzel and M. Spannowsky, Tagging highly boosted top quarks, Phys. Rev.D89(2014) 014007, arXiv: 1308.0540 [hep-ph]
- [38] T. Plehn et al., Stop Reconstruction with Tagged Tops, JHEP 10 (2010) 078, arXiv: 1006.2833 [hep-ph]
- [39] T. Plehn, G. P. Salam and M. Spannowsky, Fat Jets for a Light Higgs, Phys. Rev. Lett. 104 (2010) 111801, arXiv: 0910.5472 [hep-ph]
- [40] A. J. Larkoski, F. Maltoni and M. Selvaggi, Tracking down hyper-boosted top quarks, JHEP 06 (2015) 032, arXiv: 1503.03347 [hep-ph]
- [41] S. Bressler et al., Hadronic Calorimeter Shower Size: Challenges and Opportunities for Jet Substructure in the Superboosted Regime, (2015), arXiv: 1506.02656 [hep-ph]

A. List of Tables and Figures

A.1. List of Figures

1.1	Particles in the Standard Model	2
1.2	$\alpha_S(Q)$ from CMS analysis	8
1.3	Feynman diagrams considered	10
1.4	Schematic of the RS model	11
2.1	Accelerator chain at CERN.	14
2.2	Luminosity in ATLAS	15
2.3	Overview of the ATLAS detector.	16
2.4	The ATLAS Inner Detector and its sub-detectors.	17
2.5	The ATLAS Inner Detector barrel view.	18
2.6	ATLAS overview of the calorimeter setup.	20
2.7	Interaction lengths for the calorimeter	21
2.8	EM calorimeter section, barrel	22
2.9	Schematic view of a tile module	23
2.10	Set-up of the muon system sub-detectors	25
2.11	Cross section for SM processes	26
3.1	Kinematic distributions for the jet of the W' sample.	29
4.1	Tasso 3-jet final state	31
4.2	Schematic representation of the string model, used in PYTHIA.	32
4.3	Behavior of well defined jet algorithms	33
4.4	Overview of the various reclustering algorithms	35
4.5	Overview of the calibration procedure in ATLAS	37
4.6	Impact of the extreme kinematic regime on the decay products	40
4.7	Angular separation ΔR for W s and quarks	41
4.8	Schematic of the trimming algorithm.	43

5.1	Mass distribution for boosted W/Z	46
5.2	QCD and W' mass distribution	47
5.3	Gaussian fit for QCD multijet	47
5.4	m^{calo} response single p_T bin	49
5.5	m^{calo} and m^{TA} mass responses	50
5.6	Comparison of the uncertainties for m^{calo} and m^{TA}	51
5.7	Mass response plots for the m^{TA}	52
5.8	m^{calo} and m^{TA} comparison for W/Z jets and top jets	53
5.9	Performance of the m^{TA} with the boosted Higgs sample	54
5.10	Pictorial event display	56
5.11	m^{TAS} for boosted W/Z	57
5.12	m^{TAS} for boosted tops	58
5.13	m^{TAS} for boosted Higgs	58
5.14	m^{TAS} for QCD jets	59
5.15	m^{TAS} for boosted massive W/Z	60
5.16	Mean and left-hand side integral for boosted W/Z	61
5.17	Perfect calibration	62
5.18	Simple calibration	63
5.19	Track mass degradation in tops and massive W/Z	64
5.20	Breakdown of the m^{TAS}	65
5.21	Different reclustering in event display	66
5.22	Toy example of Gaussian combination	67
5.23	m^{calo} and m^{TAS} correlation plots	69
5.24	m_{TAS}^{comb} on the boosted W/Z	70
5.25	m_{TAS}^{comb} on the boosted tops	70
5.26	m_{TAS}^{comb} on the boosted Higgs	71

A.2. List of Tables

2.1	Recap of ATLAS and performances of the sub-detectors	27
3.1	Overview of the Monte Carlo Samples used	30

B. ATLAS Detector: Further Details

Further details here about the ATLAS detector are given.

B.1. Muon subdetectors

B.1.1. RPC

The RPCs offer fast triggering of the muons, providing track information in 15 to 25 ns. They are utilized in the barrel region ($|\eta| < 1.05$) and made out of electrically resistive parallel plates with a 2mm distance filled with a gas mixture, arranged in three layers. The plates are kept at 9800 V potential difference to assure avalanche from the gas ionization caused by charged particles, which is then read out by metallic strips. The spatial resolution of this sub-detector is rather coarse, 10 mm in η, ϕ plane, which is the price to pay for the fast response.

B.1.2. TGC

The TGC is again offering fast track information, but they are placed in the end-caps ($1.05 < |\eta| < 2.4$) and with four layers. The technology adopted here is the Multi Wire Proportional Chamber (MWPC). Typical readout happens in 25 ns.

B.1.3. MDT

The MDTs consist of pressurized drift tubes and, oppositely to the RPC and TGC, provides a high precision muon momentum measurement with a slower response. It is placed in $|\eta| < 2.7$ and provides average spatial resolution of 80 μm , resulting in a total resolution of 35 μm , at the cost of charge collection time of 700 ns. Tubes are arranged in three to eight layers within each chamber, enhancing the performance of tracking pattern recognition software.

B.1.4. CSC

The CSCs, like the TGC, are made out of MWPCs, covering the innermost end-cap ($2 < |\eta| < 2.7$), with resolution of $40 \mu\text{m}$ and a time resolution of 7 ns per plane, making them able to accommodate the higher particle flux due to the beam vicinity up to 1000 Hz/cm^2 , making drift tubes technology infeasible to use in this region.

B.2. L1

The L1 exploits a raw information from the calorimeters and muons system, making use of algorithms to determine the Bunch Crossing Identification (BCID) associated to those raw measurements. It then uses a custom-made electronics to take a decision in $\sim 25 \mu\text{s}$ on an event-by-event basis. The raw information are simplified e.g. geometrically grouping together the calorimeter cells in so called *towers*, while the muon system makes use of dedicated sub-detectors (RPC and TGC) as described above. The trigger information for the calorimeter (L1Calo) and the muon system (L1Muon) are then merged together. After that positive decision is made, the L1 defines one or more Region of Interest (RoI) which contains the measurements from the raw information and transmits those to the HLT.

B.3. HLT

At this step, in Run 1, the L2 trigger matched the inner detector data to the RoI, and made a successive trigger decision based on ID also, having $\sim 40 \text{ ms}$ for this operation. The selected events were then passed to the EF, which performed a full-granularity event reconstruction in the RoI, using hence all the sub-detector and not anymore raw data only, including calibrations, alignment corrections etc. The EF had here 4 s for the final decision. The computer resources were allocated separately to L2 and EF; in Run 2 instead this two step were reduced to 1 in the HLT, which is now a unique computer farm with merged processing nodes, for simplification and dynamic resources sharing. If the event is again positive, it is registered on disk (here the final rate is 200 Hz) and will be then used for offline analyses.

B.4. Luminosity Measurement

The delivered luminosity can be written as a function of the accelerator parameters as:

$$\mathcal{L} = \frac{n_B f_r n_1 n_2}{2\pi \Sigma_x \Sigma_y}$$

where $n_{1,2}$ are the numbers of protons per beam (1,2), $\Sigma_{x,y}$ characterize the horizontal and vertical convoluted beam width (measured through Van der Meer scans) and f_r is the revolution frequency and n_B is the number of bunches traveling at frequency f_r . There are also alternative parametrizations, where delivered luminosity is written as a function of the visible total inelastic cross section σ_{vis} and the average number of inelastic interactions per bunch crossing μ_{vis} . A fundamental ingredient of the ATLAS strategy to assess and control the systematic uncertainties affecting the absolute luminosity determination is to compare the measurements of several luminosity detectors, most of which use more than one algorithm to assess the luminosity. These multiple detectors and algorithms are characterized by a significant different acceptance, response to pile-up, and sensitivity to instrumental effects and to beam-induced backgrounds.

C. Parton Shower and Hadronization Details

C.1. Parton Shower

To perform a quantitative study of the parton shower, one can start from the simple $2 \rightarrow 2$ process with the further splitting into quarks and gluons, e.g. $q \rightarrow qg$, $g \rightarrow q\bar{q}$ and $g \rightarrow gg$. Parton shower can originate from initial state radiation (ISR) or final state radiation (FSR) like in Figure C.1. For details on this section, see [19]. The resulting process can now be depicted as

$$2 \rightarrow 2 \otimes \text{ISR} \otimes \text{FSR}$$

For the simplest $2 \rightarrow 2$ process, the production cross section is given by:

$$\sigma = \sum_{i,j} \iiint dx_1 dx_2 d\hat{t} f_i^A(x_1, Q^2) f_j^B(x_2, Q^2) \frac{d\hat{\sigma}_{i,j}}{d\hat{t}}$$

where i, j are the incoming partons and $f_{i,j}^{A,B}(x_{1,2}, Q^2)$ are the parton distribution functions of partons in the incoming protons, A and B and Q^2 being the momentum transfer squared. The parton distribution function (PDFs) of gluons and sea quarks are strongly peaked at small momentum fractions $x_1 \sim E_i/E_A$, $x_2 \sim E_j/E_B$. The first step is to study the particular case of $2 \rightarrow 3$ e.g. with an additional gluon radiated from a quark in the final state. Here the cross section can be written in the form [18]:

$$\frac{d\sigma_{2 \rightarrow 3}}{\sigma_{2 \rightarrow 2}} = \frac{\alpha_S}{2\pi} \frac{4}{3} \frac{x_1^2 + x_2^2}{(1-x_1)(1-x_2)} dx_1 dx_2 \quad (\text{C.1})$$

neglecting the quark masses. Now rewriting the energy fractions x_j as $1 - x_2 = Q^2/E_{cm}^2$, $x_1 \sim z$, $x_3 \sim 1 - z$, equation C.1 looks as follows:

$$d\mathcal{P} = \frac{d\sigma_{2 \rightarrow 3}}{\sigma_{2 \rightarrow 2}} \simeq \frac{\alpha_S}{2\pi} \frac{dQ^2}{Q^2} \frac{4}{3} \frac{1+z^2}{1-z} dz$$

which is collinear singular ($Q^2 \sim 1 - \cos\theta \rightarrow 0$ if $\theta \rightarrow 0$).

To generalize the probability for the process $a \rightarrow bc$, which could be then gluon radiation ($q \rightarrow qq$) gluon splitting ($g \rightarrow gg$) or quark-antiquark splitting ($g \rightarrow q\bar{q}$), the Dokshitzer-Gribov-Lipatov-Altarelli-Parisi (DGLAP) equations are used:

$$d\mathcal{P}_{a \rightarrow bc} = \frac{\alpha_S}{2\pi} \frac{dQ^2}{Q^2} P_{a \rightarrow bc}(z) dz$$

where $P_{a \rightarrow bc}$ are fragmentation functions:

$$P_{q \rightarrow qq} = \frac{4}{3} \frac{1+z^2}{1-z}$$

$$P_{q \rightarrow gg} = 3 \frac{(1-z(1-z))^2}{z(1-z)}$$

$$P_{q \rightarrow q\bar{q}} = \frac{n_f}{2} (z^2 + (1-z)^2)$$

and with n_f being the number of quark flavors.

To describe now a cascade of successive branchings, like e.g. the one depicted in Figure C.2, one has to evolve the DGLAP equation above in smaller and smaller Q^2 using the so-called *Sudakov factor* which describes the probability that the *first* emission happens at time T

$$d\mathcal{P}_{first}(T) = d\mathcal{P}_{sth}(T) \exp\left(-\int_0^T \frac{d\mathcal{P}_{sth}(t)}{dt} dt\right)$$

where \mathcal{P}_{sth} is the probability of branching.

Thereby, the DGLAP equations become then

$$d\mathcal{P}_{a \rightarrow bc}(T) = \frac{\alpha_S}{2\pi} \frac{dQ^2}{Q^2} P_{a \rightarrow bc}(z) dz \exp\left(-\sum_b \int_{Q^2}^{Q_{max}^2} \frac{dQ'^2}{Q'^2} \int \frac{\alpha_S}{2\pi} P_{a \rightarrow bc}(z') dz'\right)$$

where the exponential term is called the Sudakov form factor and intuitively represents the probability of not having already radiated a particle with higher momentum transfer. Sudakov formulation provides by definition the order in Q^2 (from larger to smaller) or in “times” from smaller to larger. By introducing the Q_{max}^2 as Q^2 of the hard-process one can regulate the collinear singularities.

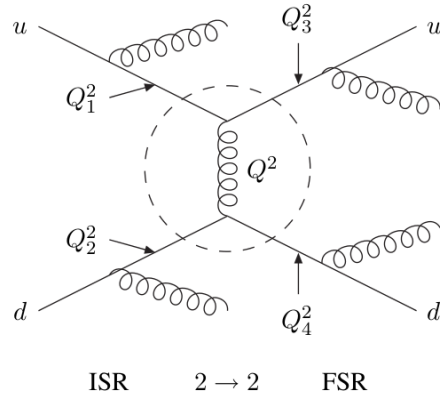


Figure C.1: Example of factorization of $2 \rightarrow n$ process.

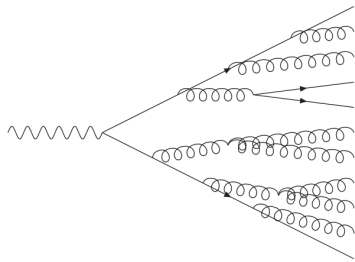


Figure C.2: Example of cascade of successive branchings.

Parton showers from ISR are described in similar way, but with the additional complication of taking into account the parton distribution functions.

Due to the asymptotic freedom, quarks and gluons resulting from the fragmentation described above, behave as quasi-free particles called partons, only at short distances (order of 10^{-2} fm); when these colored objects separate more than the order of 1 fm, the

confinement forces become effective, which have the effect of binding the quarks and gluons in hadrons. This process is referred to as *hadronization*, which is a stochastic process involving a large number of particles, also described in the next section. The hadronization proceeds in fact through the formation of jet in high energy processes.

C.2. Hadronization

Being non-perturbative, the process of hadronization is described with phenomenological models, the most important ones being: independent jet fragmentation, Lund string model and cluster hadronization.

In the first one, which is first one also historically in PETRA and PEP, gluonic flux tubes appear when colored objects separate and can then split to quark-antiquark pairs balancing their energy fraction and forming then primary mesons; the process lasts with the un-hadronized quarks and until the energy decreases to a cut-off. The problem of the model was an overall unsatisfactory implementation of the energy-momentum conservation, but had the advantage of a small number of parameters and simplicity.

In the (Lund) string model, which is similar to the independent fragmentation, $q\bar{q}$ interaction is described as string interaction with $V(r) \sim kr$, with r being the distance, $k = \left| \frac{dE}{dz} \right| = \left| \frac{dp_z}{dz} \right| = \left| \frac{dE}{dt} \right| = \left| \frac{dp_z}{dt} \right|$ and neglecting the Coulomb part of the interaction. When tension reaches the critical values, the string breaks, forming new $q\bar{q}$ pair. See Figure 4.2 for a schematic representation.

In the cluster model, hadronization mechanism is based on color pre-confinement; in fact gluons split to quark-antiquark pairs and nearby partons in cascade arrange themselves in color-neutral clusters, preferably at small invariant mass, down to the

QCD scale, $\mathcal{O}(200 \text{ MeV})$. With respect to the string model, it has the advantage of having a simple flavor composition with fewer parameters, but a less predictive energy-momentum description with more parameters.

D. Topo-Clustering and Local Calibration Weighting

Topo-Clusters

Topological cell clustering or topo-clustering, is the process where the calorimeter cells are grouped together in order to find energy deposited from the hard-scattering process. The result of topo-clustering is the formation of topo-cluster, in a way that suppresses calorimeter contribution from noise related effects, but still maintaining the activity from the underlying physical process. The topo-clustering works as follow: first a seed cell is defined, and then other neighboring cells are added to the seed if their energy is above a noise threshold. It is efficient at suppressing noise in clusters with large numbers of cells [20].

An additional step is taken to further reduce noise contribution, enhance the performance of topo-clusters and ensure that no bias is introduced in data: a local calibration scheme (Local Calibration Weighting, LCW) [21] is also applied, based on Monte Carlo.

The calibration weights are determined from simulations of charged and neutral pions according to the cluster topology measured in the calorimeter. The cluster properties used are the energy density in the cells forming them, the fraction of their energy deposited in the different calorimeter layers, the cluster isolation and its depth in the calorimeter. The natural requirement which has to be satisfied at this point is that the calorimeters cells should be then (three-dimensionally) “grouped” together, in order to reconstruct the energy of the hard-scattered particle. This is done in ATLAS in two steps: first the collection of calorimeter energy deposit represented as topo-clusters is created; then those objects are used as input for the jet reconstruction algorithm (here we are speaking of topo-clusters for the reconstruction of calorimeter jets; however other input can be tracks for track-jets and truth particles for truth-jets). Corrections are applied to the cluster energy to account for the energy deposited in the calorimeter, but outside of clusters and energy deposited

in material before and in between the calorimeters. Jets are formed from calibrated clusters by using dedicated reclustering algorithms, described in the body of the thesis.

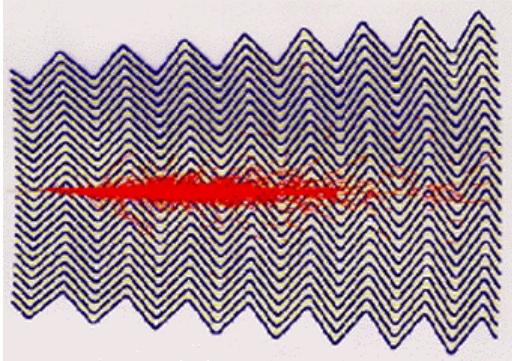


Figure D.1: Shower development in the accordion calorimeter, Monte Carlo simulation.

E. Pile-Up and Underlying Event

The *pile-up* is a term used to describe the jets coming from another interaction in the same bunch-crossing (*in-time pile-up*), i.e. coming from another interaction at low- p_T which happens together with the hard-scattering, or in another bunch-crossing (*out-of-time pile-up*), before or after the hard-scattering. When sub-detectors are sensitive to several bunch-crossing or their electronics integrate over more than 25 ns, these collisions can affect the signal in the collision of interest.

In case of the in-time pile-up, this effect can be directly parametrized by the number of primary vertices N_{PV} reconstructed, which is around 15 for Run 2, and by the average number of interactions per bunch-crossing $\langle\mu\rangle$ (which is a function of the instantaneous luminosity \mathcal{L}) by the total inelastic cross section σ_{in} and by the average frequency of bunch-crossing at the LHC $N_{bunch} \times f_{LHC}$:

$$\langle\mu\rangle = \frac{\mathcal{L} \times \sigma_{in}}{N_{bunch} \times f_{LHC}}$$

Given the increased luminosity condition for the Run 2, the average number of interactions is around 24, making the soft radiation contamination from PU an issue of increasing seriousness. The Underlying Event is a term which describes, in the single proton-proton interaction, all the phenomena, besides the hard-scattering, of several softer parton-parton scatters and the fragmentation of QCD strings which connects colored objects including beam remnant and initial and final state radiation [32]. Coming from the primary vertex, those soft radiations survive the tracks requirement to come from the PV (which is not the case for pile-up).

As seen in Figure E.1, where the large- R jet mass is shown with five different PU

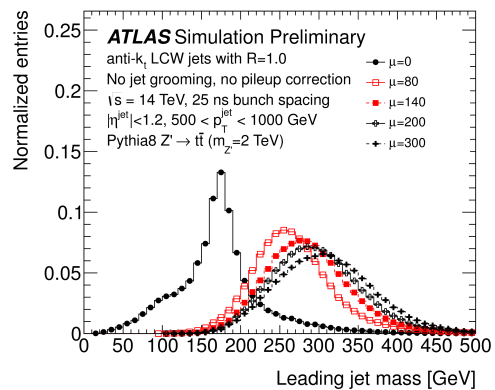


Figure E.1: Effect of pile-up contamination in large- R jets: here shown different PU conditions parametrized by $\langle\mu\rangle$. From [33].

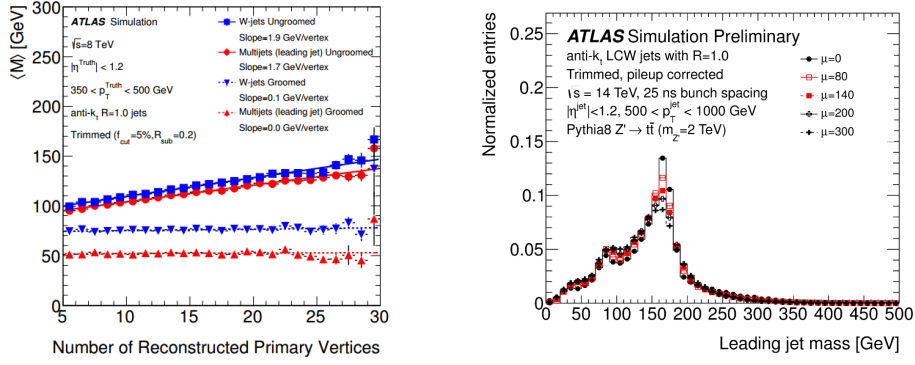


Figure E.2: Left: mass reconstructed as a function of the number of primary vertices (parameterizing PU) for different samples; after trimming procedure the mass is pretty much independent of PU for all the samples. Right: mass distributions for different PU conditions: after trimming the reconstruction is not degraded as much as Figure E.1.

conditions, the contamination spoils the distribution, giving rise to a misreconstruction which gets worse as it goes to worse environment conditions.

Other relatively small sources of contamination can be e.g. cavern background, beam halo events and beam gas events.

F. Additional Grooming Techniques

The standard grooming technique used for the optimization studies of this thesis was described in the body; however there are two common choices which are worth mentioning here: the *split-filtering* and the *pruning*

F.1. Split-Filtering

The split-filtering was developed and optimized using C/A in jet searches of Higgs to b -quarks. It is made out of two stages: the *Mass-drop and symmetry* and the *Filtering*. For the Mass-drop and symmetry these are the steps:

- the last step of C/A is undone, obtaining two sub-jets (e.g. the ones that should contain the bottom quark from Higgs decay);
- a significant difference between the parent jet mass and the sub-jets j_i is required: $m^{j_i}/m^{jet} < \mu_{frac}$;
- the two p_T of the sub-jets are required to be relatively similar (symmetry requirement) by the condition $\frac{\min[(p_T^{j_1})^2, (p_T^{j_2})^2]}{(m^{jet})^2} \times \Delta R_{j_1, j_2}^2 > y_{cut}$.

If the mass-drop and symmetry criteria are not satisfied, the jet is discarded. The second step is the filtering:

- j_1 and j_2 are reclustered with the C/A algorithm with variable radius parameter $R_{filt} = \min[0.3, \Delta R_{j_1, j_2}^2/2]$, where $R_{filt} < \Delta R_{j_1, j_2}^2$;
- the jet is then filtered: all the constituents outside the three hardest sub-jets are discarded, in order to allow the emission of an additional radiation from the two-body decay;
- the split-filtered jet is composed of those three sub-jets only.

This method shows powerful sensitivity to highly collimated decays.

F.2. Pruning

The pruning algorithm is widely used in CMS; it works in a similar manner as the trimming, removing constituents (not sub-jets) with a relatively small p_T , but additionally applying a veto on wide angle radiation. The procedure runs as follows:

- the C/A or k_t reclustering algorithms is run on the constituents of the parent jet;
- at each reclustering step, transverse momentum *or* an angular requirement has to be satisfied: being j_1 and j_2 the constituents, either $p_T^{j_1}/p_T^{j_1+j_2} > z_{cut}$ or $\Delta R_{j_1,j_2}^2 < R_{cut} \times (2m^{jet}/p_T^{jet})$;
- j_1 and j_2 are merged only if one or both of those criteria are met, else j_2 is discarded and the algorithm continues.

G. Limitation of the m^{TAS}

In this Appendix, additional results on the limitation of the m^{TAS} based on MC studies without detector interactions are presented. In particular, the truth study presented for boosted W/Z decay in the thesis is here extended for boosted top quark decays.

As seen on Figure G.1, the breakdown of the m^{TAS} shows that, in particular for the high transverse momenta regimes, the tracks are subjected to fast degradation which makes their combination with the calorimeter mass not anymore an advantage.

This is a limitation which was expected and understood from the detector performance point of view, and here shows the impossibility, with the variables which are presented here m^{TA} and m^{TAS} to reach a competitive standpoint with the m^{calo} in the extreme kinematic regime for the top quark decay.

In black, in fact, the performance of the m^{TAS} variable using tracks with detector effect and sub-jets without those effects, shows this intrinsic limit which takes place already at 1.5 TeV.

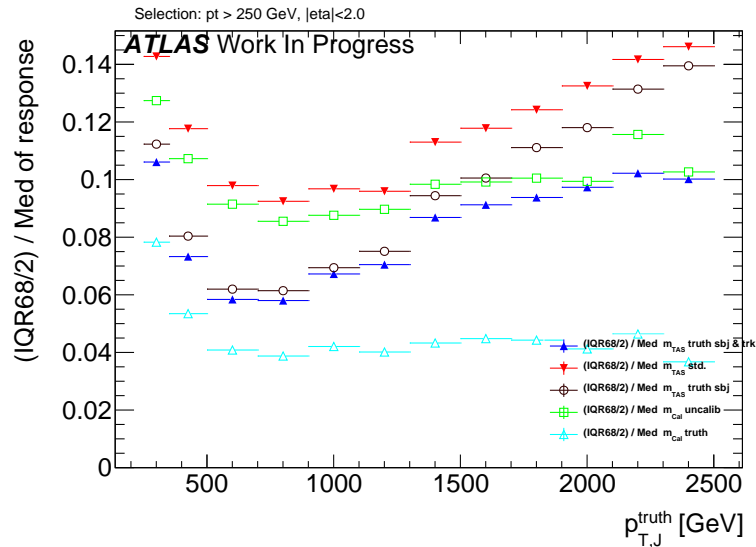
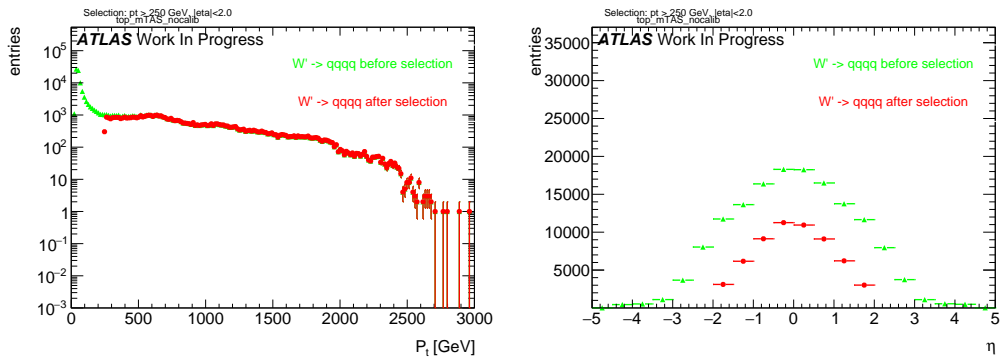


Figure G.1: Breakdown of the m^{TAS} in its component using truth-level information for boosted top quarks decays.

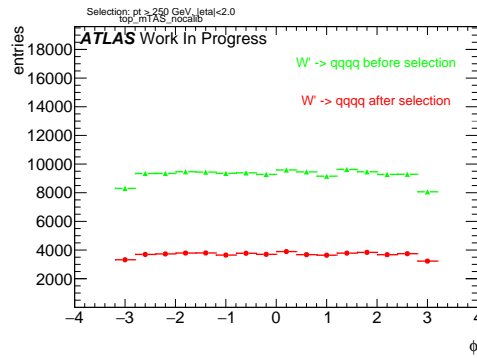
H. Jet Mass Observable Distribution

Kinematic distribution for all the samples, p_T , η and ϕ is shown.



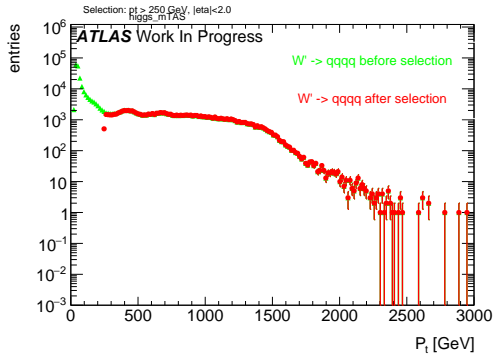
(a) p_T distribution

(b) η distribution

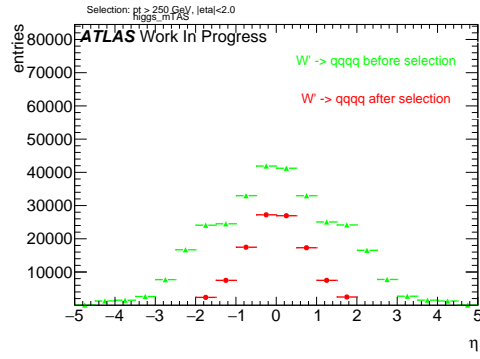


(c) ϕ distribution

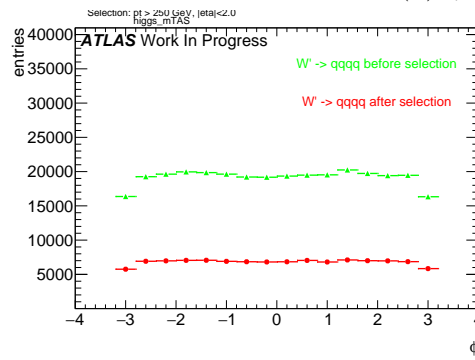
Figure H.1: Boosted tops kinematic distribution.



(a) p_T distribution



(b) η distribution



(c) ϕ distribution

Figure H.2: RS-Graviton kinematic distribution.

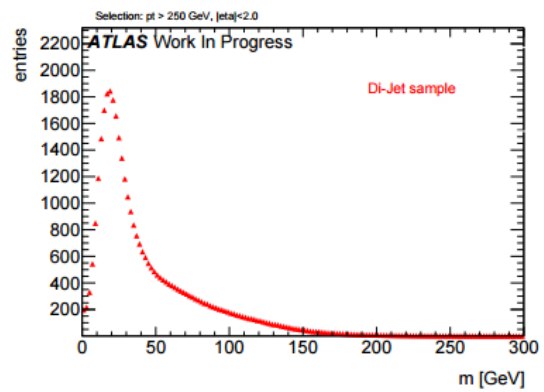
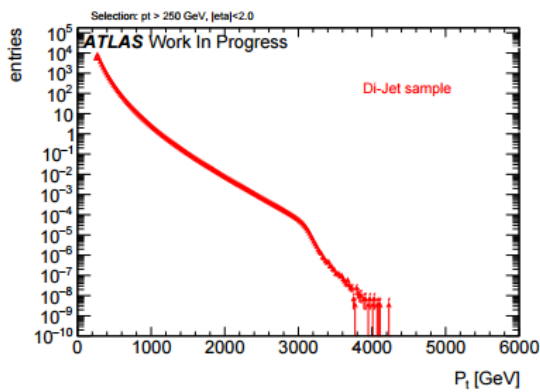


Figure H.3: QCD dijet transverse momentum and mass distributions.

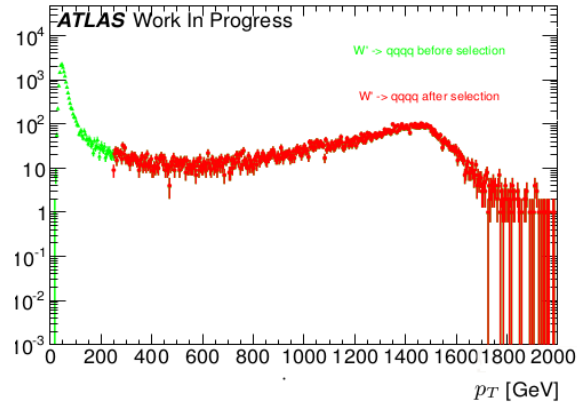


Figure H.4: The p_T distribution of a 3 TeV resonance from the hadronically decaying W or Z , in logarithmic plot. As can be seen, the jacobian peak is around $p_T \simeq m_{W'}/2 \simeq 1.5$ TeV.

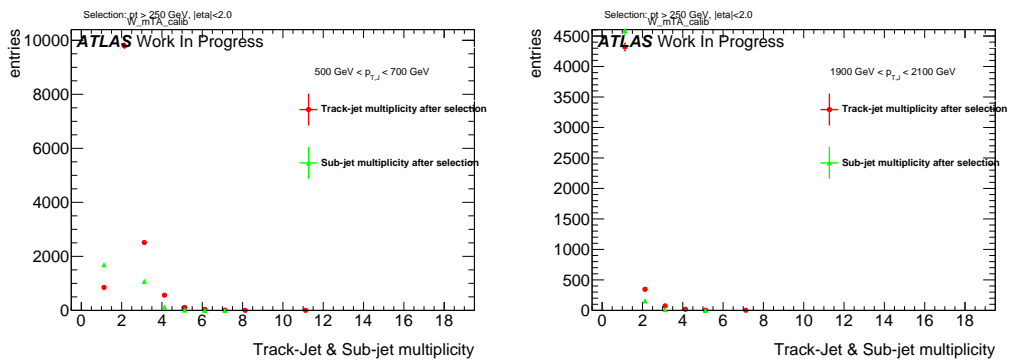


Figure H.5: Sub-jet and Track-jet (jets created having tracks as input) multiplicity, for selected bins of transverse momentum.

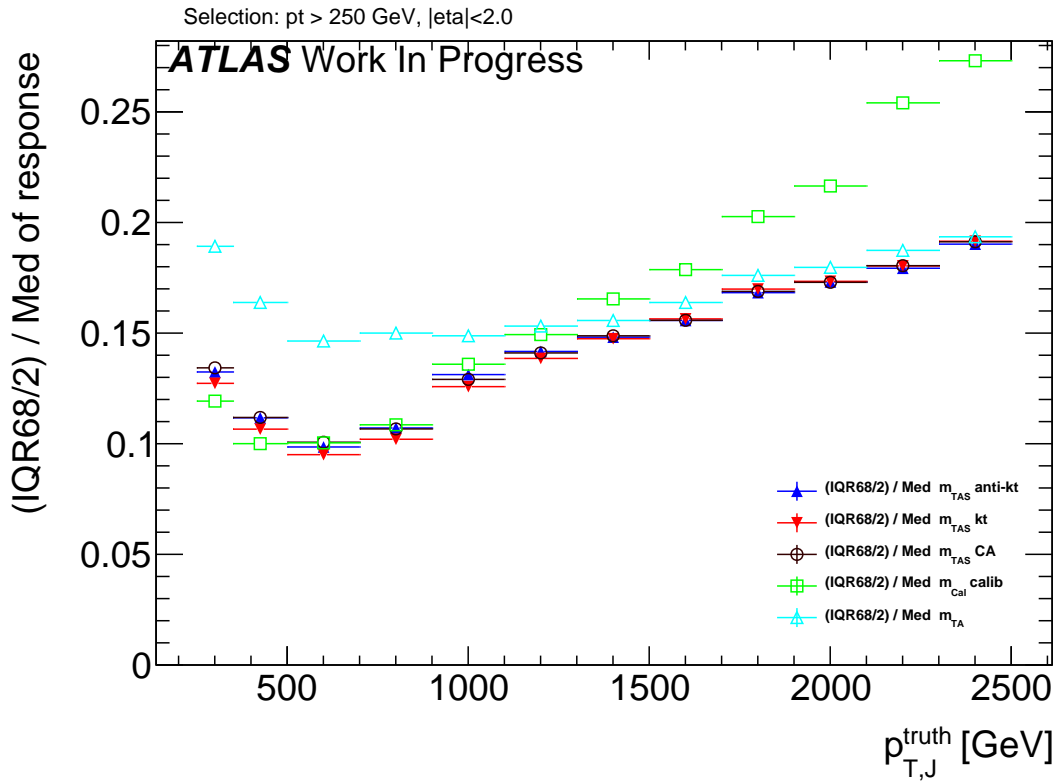


Figure H.6: Performance of m^{TAS} with different reclustering algorithm for the sub-jets: anti- k_t , k_t and C/A. Boosted W/Z sample.

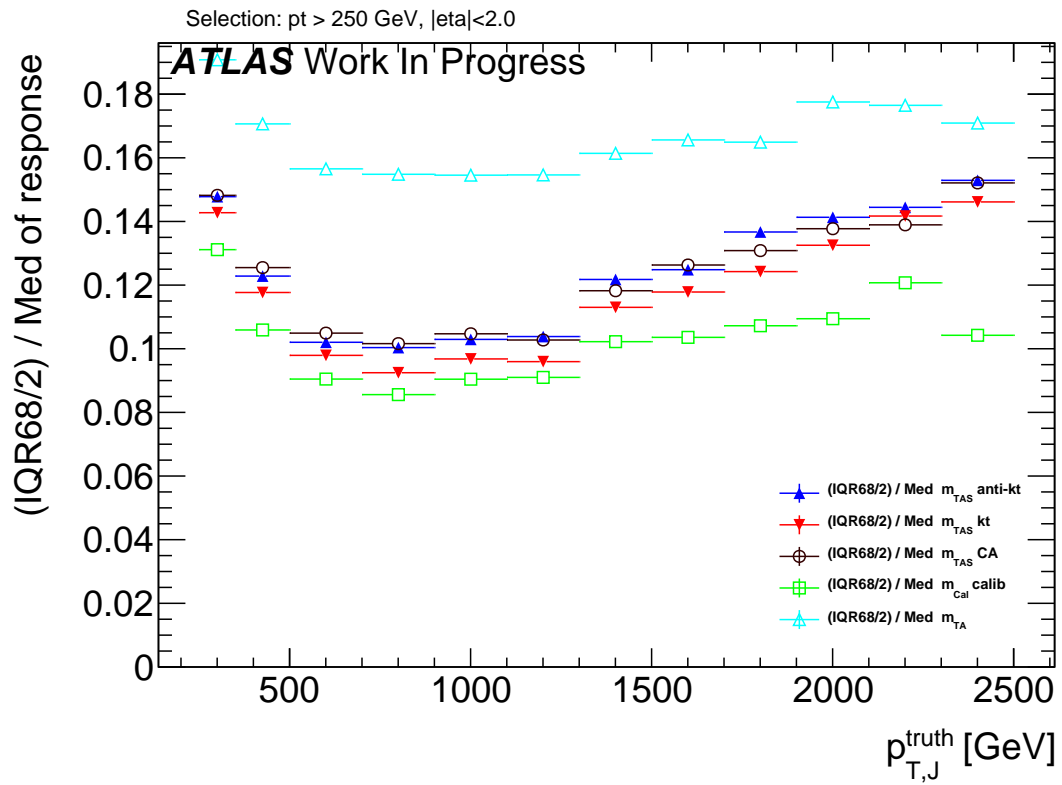


Figure H.7: Performance of m^{TAS} with different reclustering algorithm for the subjects: anti- k_t , k_t and C/A. Boosted top sample.

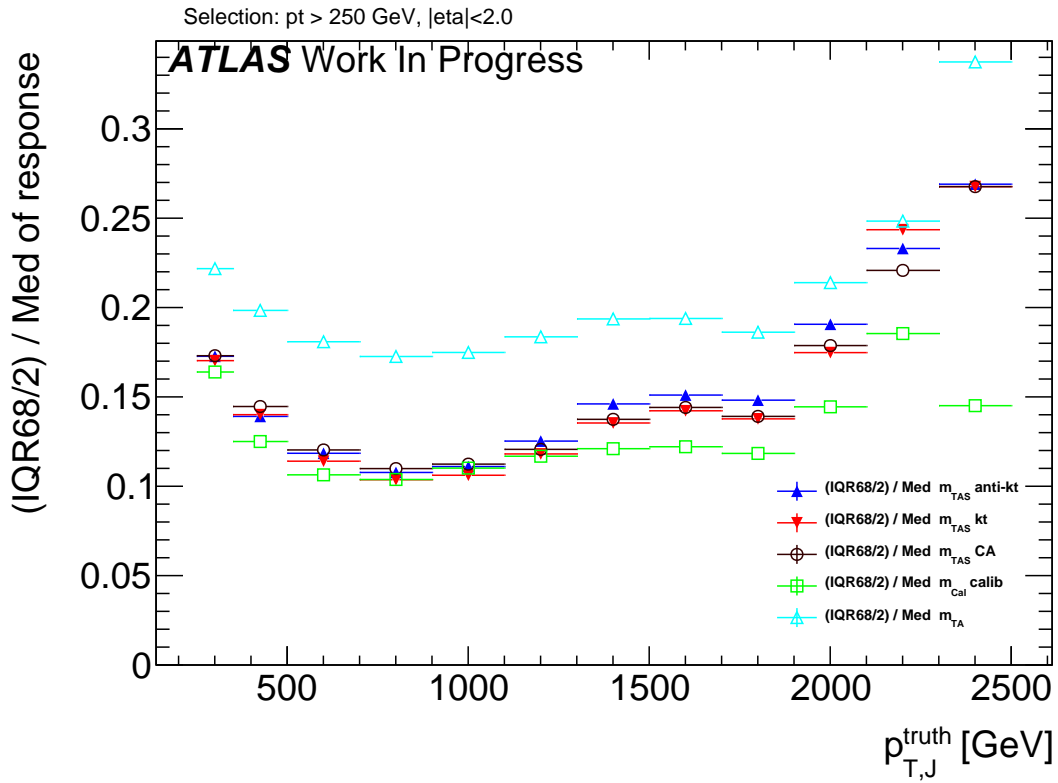


Figure H.8: Performance of m^{TAS} with different reclustering algorithm for the sub-jets: anti- k_t , k_t and C/A. Boosted higgs sample.

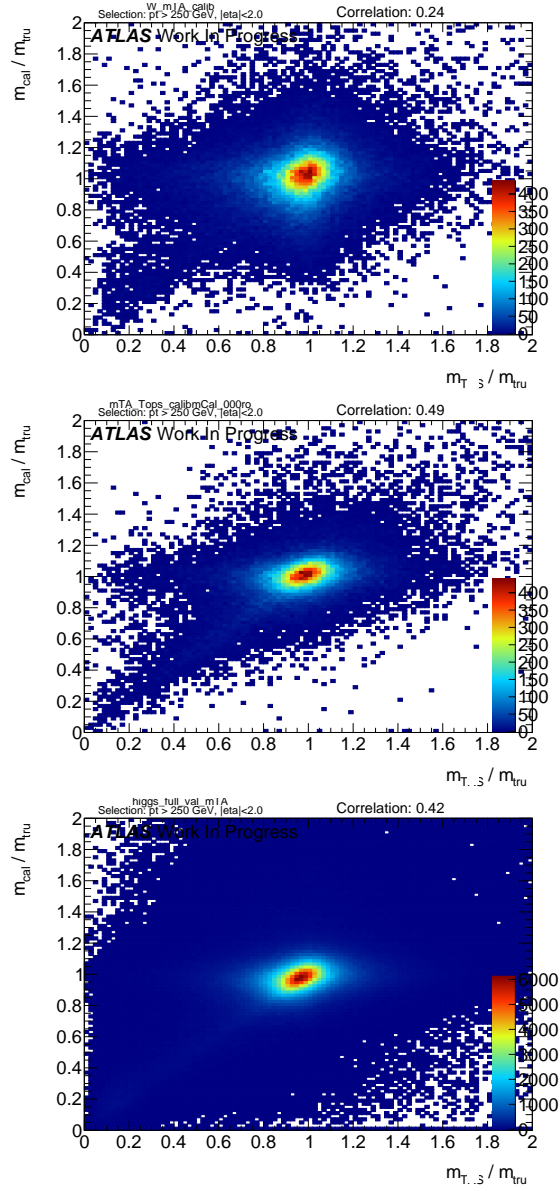


Figure H.9: Calorimeter based jet mass response vs the track-assisted mass response for the three signal samples. Correlation coefficient is indicated on the top right.

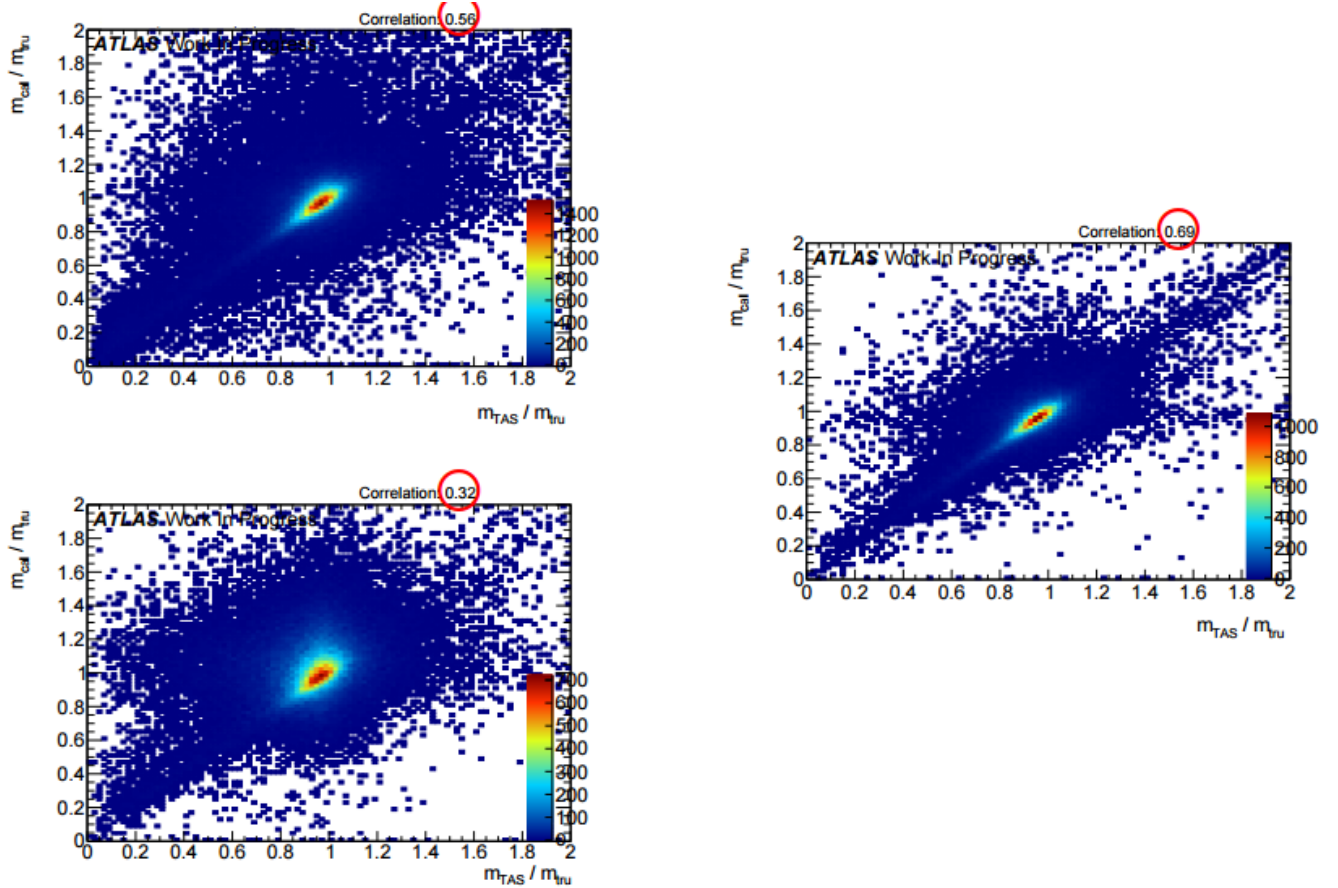


Figure H.10: Calorimeter based jet mass response vs the track-assisted sub-jet mass response for the three signal samples. Correlation coefficient is indicated on the top right and highlighted. On the left, top, the higgs sample, bottom, the W/Z ; on the right the top-quark sample.

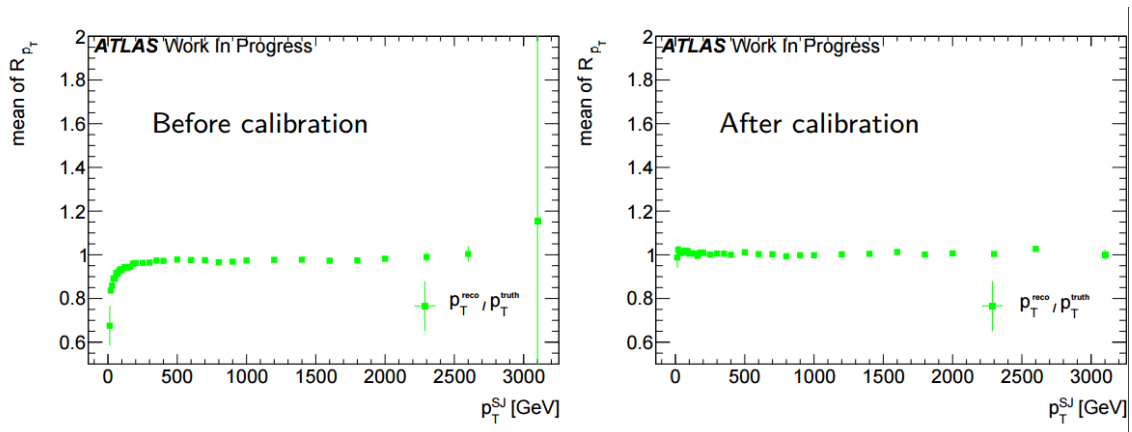


Figure H.11: Poor's man calibration effect on mean of transverse momentum's response of the sub-jet, before, left, and after, right, the procedure.

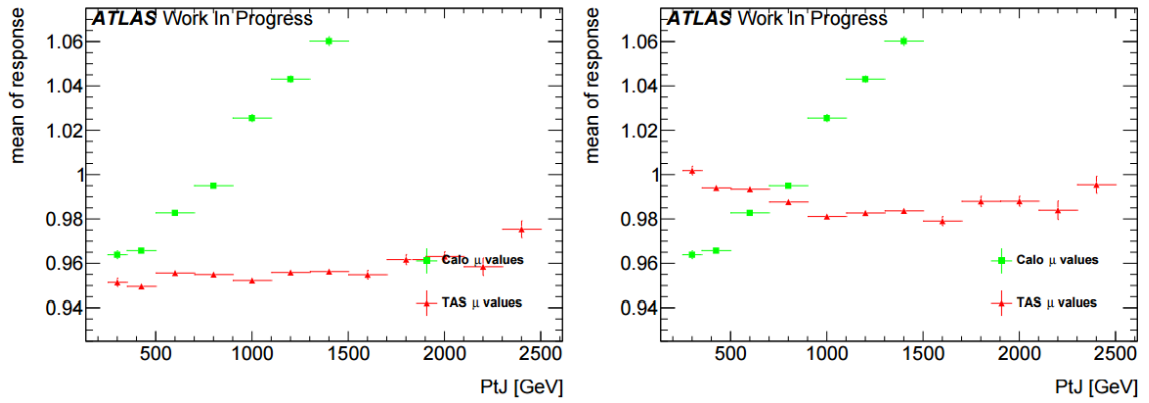


Figure H.12: Poor's man calibration effect on the mean of the mass response of the large-R jet, before, left, and after, right, the procedure.

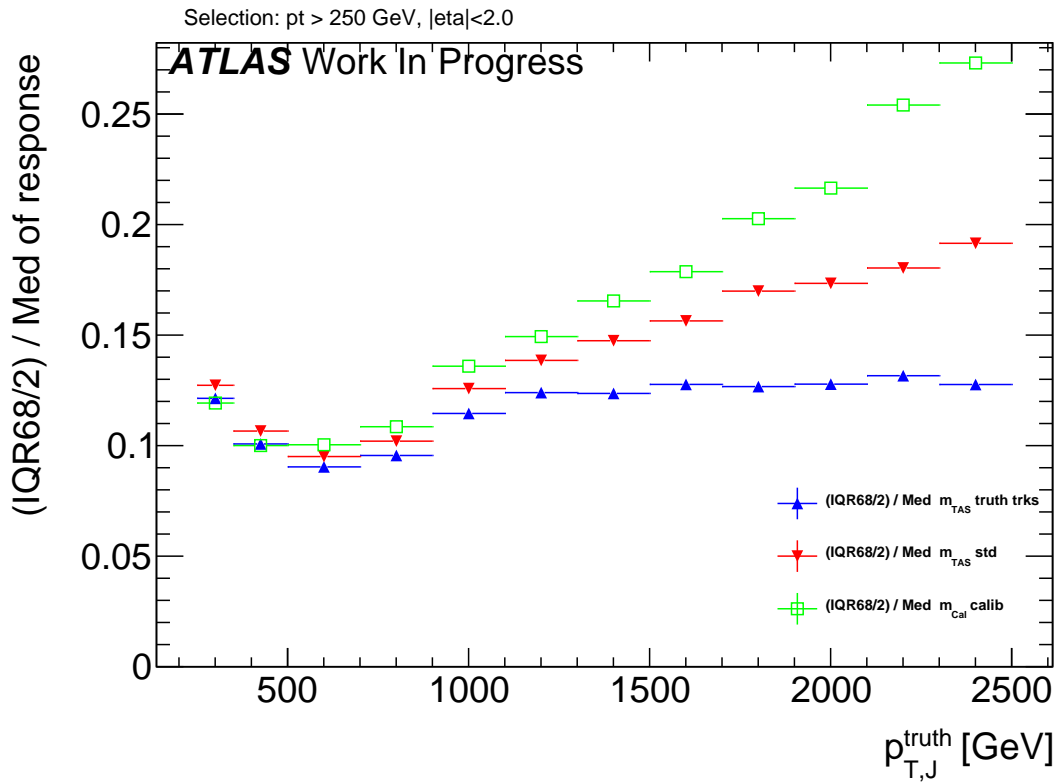


Figure H.13: Comparison of the m^{TAS} and the same variable using truth-level information for the tracks.

H.1. m^{TAS} distributions, boosted W/Z

APPENDIX H. JET MASS OBSERVABLE DISTRIBUTION

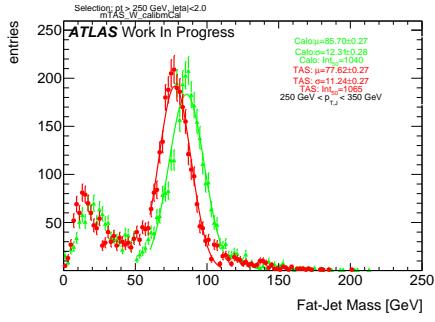


Figure H.14: m^{TAS} and m^{calo} for p_T^J bin (indicated on plot)

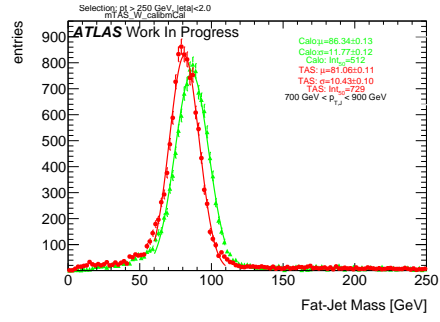


Figure H.17: m^{TAS} and m^{calo} for p_T^J bin (indicated on plot)

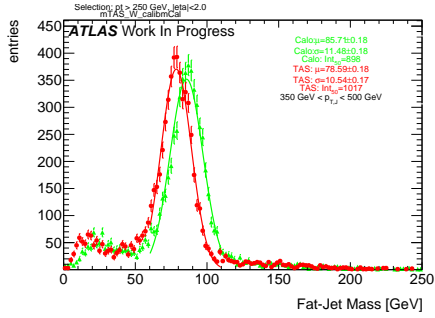


Figure H.15: m^{TAS} and m^{calo} for p_T^J bin (indicated on plot)

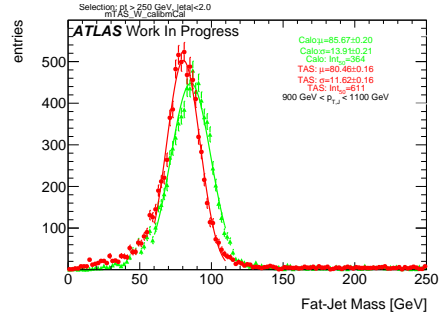


Figure H.18: m^{TAS} and m^{calo} for p_T^J bin (indicated on plot)

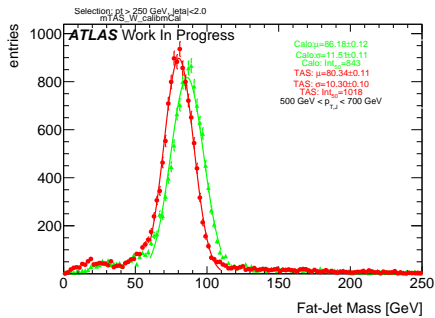


Figure H.16: m^{TAS} and m^{calo} for p_T^J bin (indicated on plot)

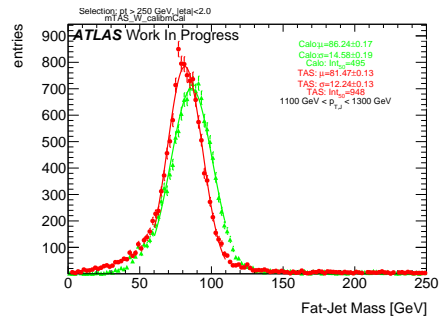


Figure H.19: m^{TAS} and m^{calo} for p_T^J bin (indicated on plot)

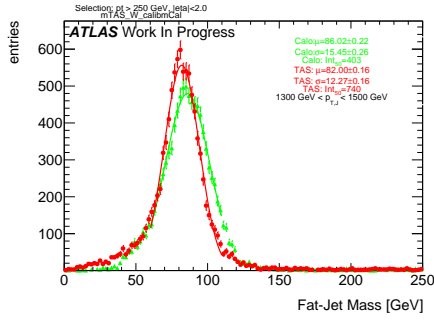


Figure H.20: m^{TAS} and m^{calo} for p_T^J bin (indicated on plot)

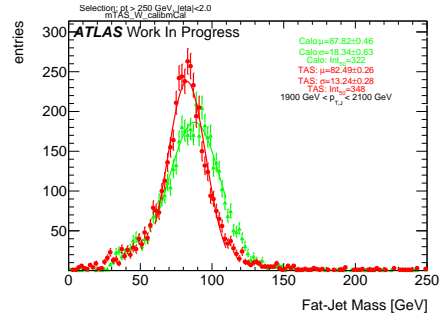


Figure H.23: m^{TAS} and m^{calo} for p_T^J bin (indicated on plot)

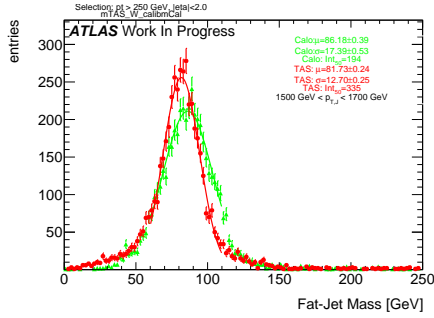


Figure H.21: m^{TAS} and m^{calo} for p_T^J bin (indicated on plot)

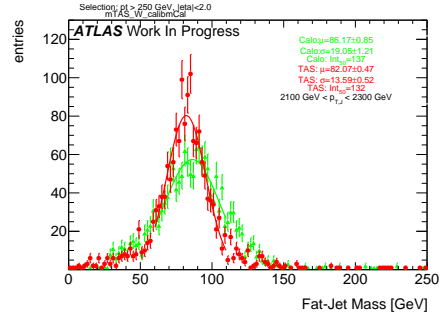


Figure H.24: m^{TAS} and m^{calo} for p_T^J bin (indicated on plot)

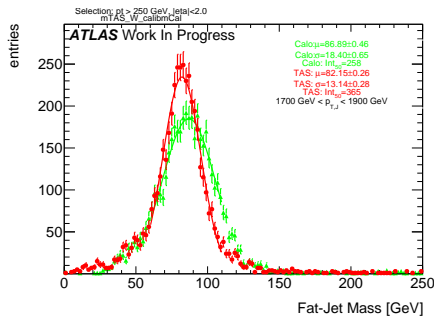


Figure H.22: m^{TAS} and m^{calo} for p_T^J bin (indicated on plot)

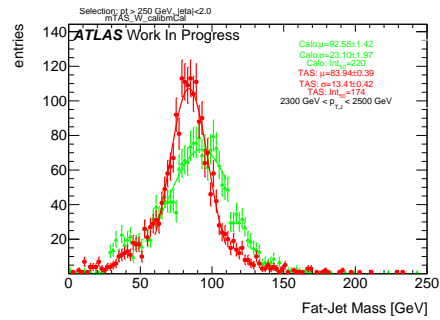


Figure H.25: m^{TAS} and m^{calo} for p_T^J bin (indicated on plot)

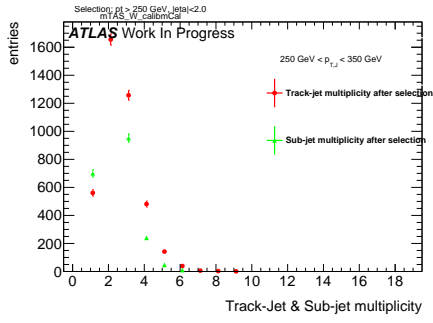


Figure H.26: Track-jet $R=0.2$ and sub-jet multiplicity for p_T^J bin (indicated on plot)

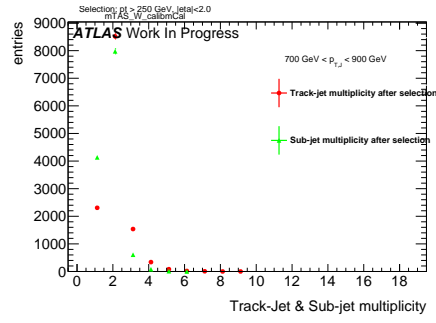


Figure H.29: Track-jet $R=0.2$ and sub-jet multiplicity for p_T^J bin (indicated on plot)

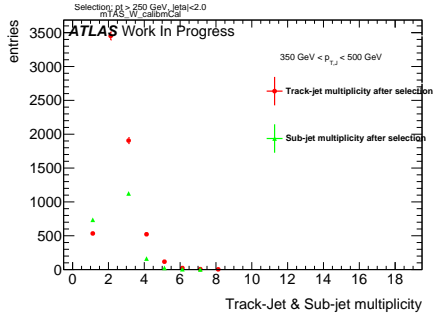


Figure H.27: Track-jet $R=0.2$ and sub-jet multiplicity for p_T^J bin (indicated on plot)

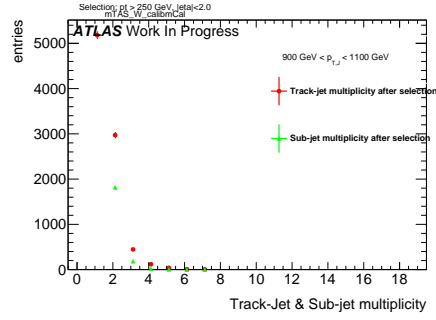


Figure H.30: Track-jet $R=0.2$ and sub-jet multiplicity for p_T^J bin (indicated on plot)

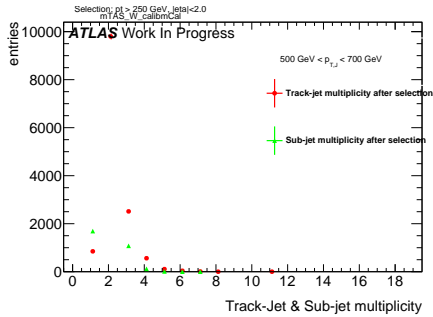


Figure H.28: Track-jet $R=0.2$ and sub-jet multiplicity for p_T^J bin (indicated on plot)

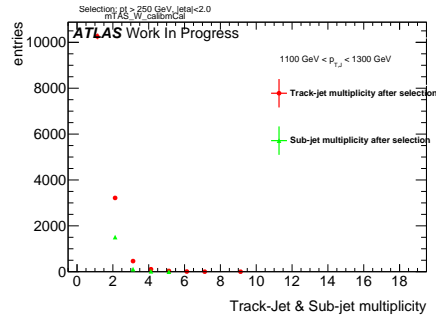


Figure H.31: Track-jet $R=0.2$ and sub-jet multiplicity for p_T^J bin (indicated on plot)

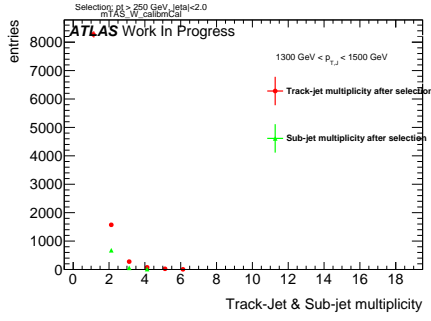


Figure H.32: Track-jet $R=0.2$ and sub-jet multiplicity for p_T^J bin (indicated on plot)

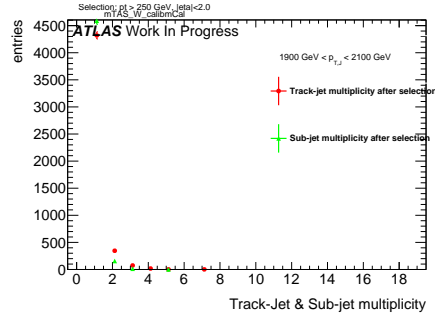


Figure H.35: Track-jet $R=0.2$ and sub-jet multiplicity for p_T^J bin (indicated on plot)

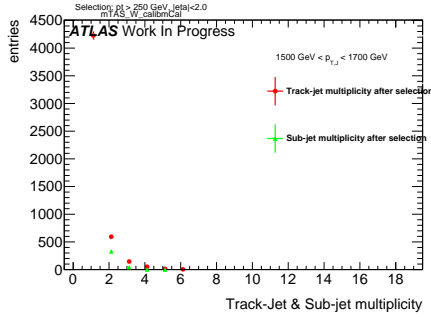


Figure H.33: Track-jet $R=0.2$ and sub-jet multiplicity for p_T^J bin (indicated on plot)

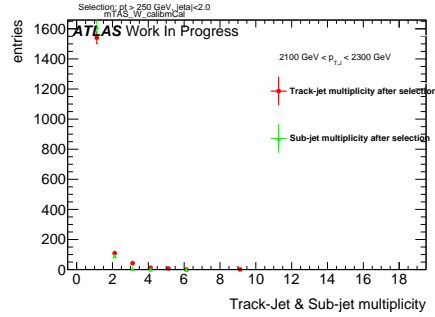


Figure H.36: Track-jet $R=0.2$ and sub-jet multiplicity for p_T^J bin (indicated on plot)

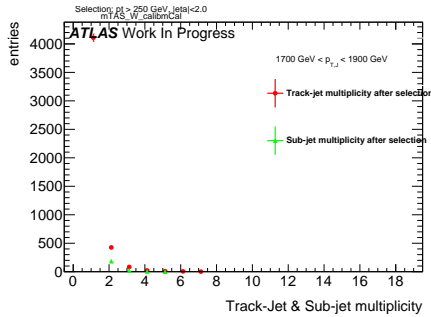


Figure H.34: Track-jet $R=0.2$ and sub-jet multiplicity for p_T^J bin (indicated on plot)

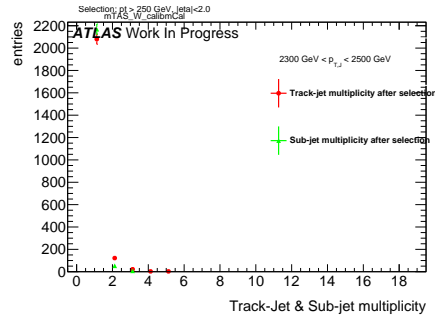


Figure H.37: Track-jet $R=0.2$ and sub-jet multiplicity for p_T^J bin (indicated on plot)

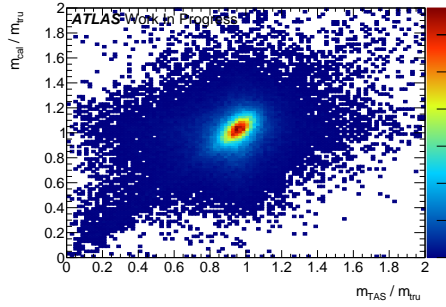


Figure H.38: Scatter plot m^{TAS} versus m^{calo} responses

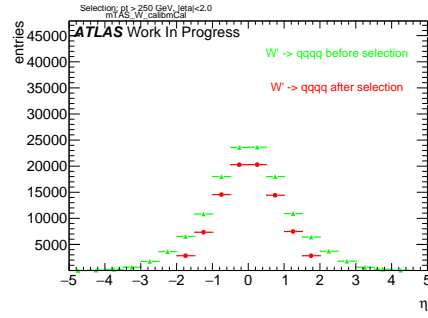


Figure H.41: η distribution of the large-R jet, before and after selection

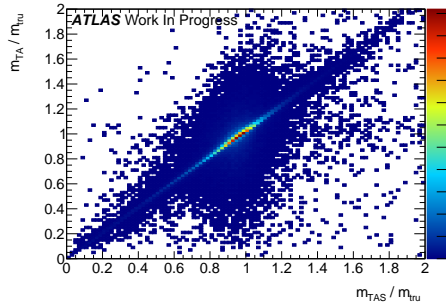


Figure H.39: Scatter plot m^{TAS} versus m^{TA} responses

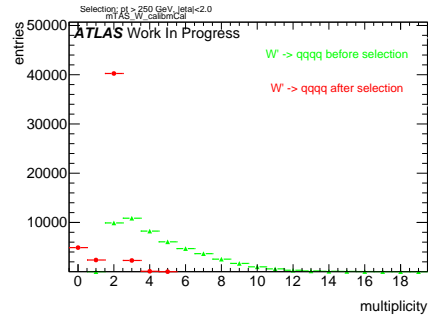


Figure H.42: large-R jet Multiplicity, before and after selection

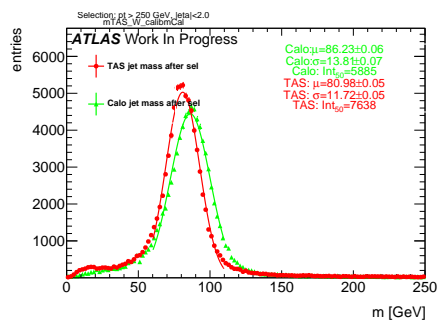


Figure H.40: m^{TAS} distribution in all the p_T bins

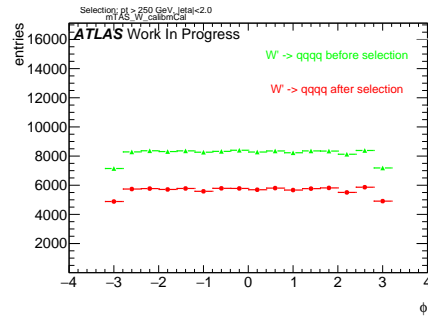


Figure H.43: ϕ distribution of the large-R jet, before and after selection

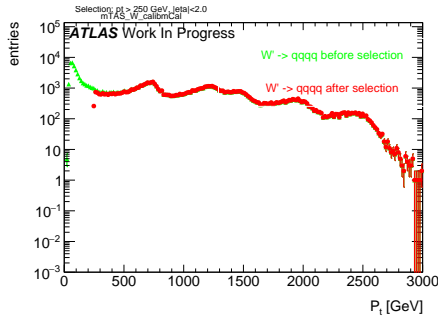


Figure H.44: p_T distribution of the large-R jet, before and after selection

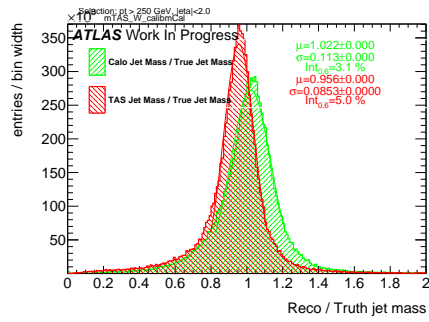


Figure H.47: Response m^{Reco}/m^{Truth} for all the p_T bins

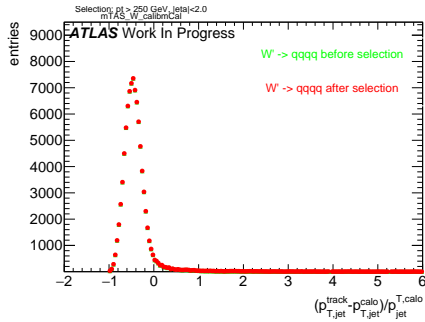


Figure H.45: p_T resolution: $\frac{p_{T,jet}^{track} - p_{T,jet}^{fat}}{p_{T,jet}^{fat}}$, before and after selection

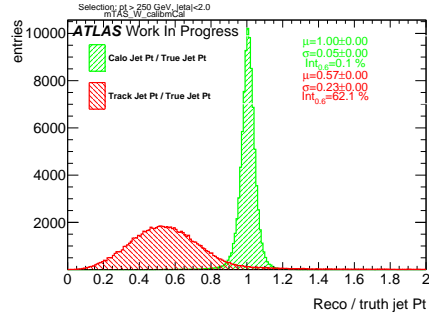


Figure H.48: Transverse momentum response p_T^{Reco}/p_T^{Truth} for calorimeter and tracks

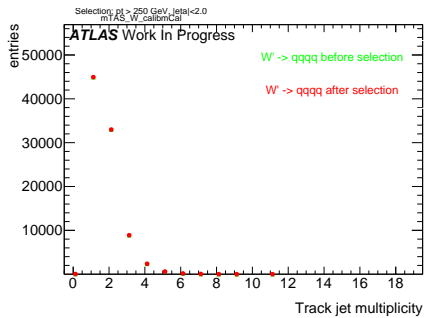


Figure H.46: Multiplicity of track-jets $R=0.2$ per large-R jet

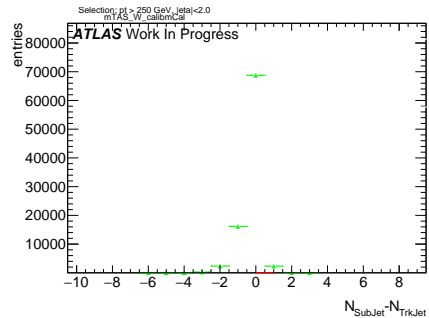


Figure H.49: sub-jet - track-jet multiplicity

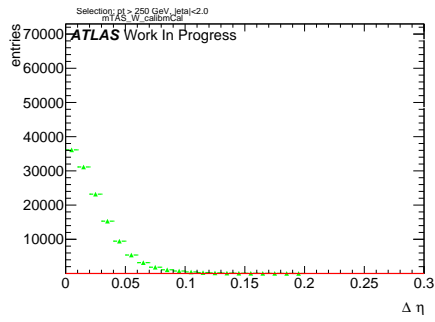


Figure H.50: $|\eta_{sub-jet} - \eta_{track-jet}|$ distribution, where sub-jet and track-jet are the closest

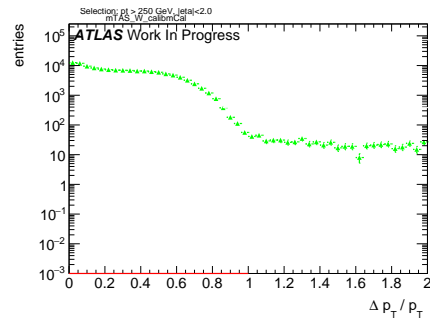


Figure H.53: $|p_{T,sub-jet} - p_{T,track-jet}|$ distribution, where sub-jet and track-jet are the closest

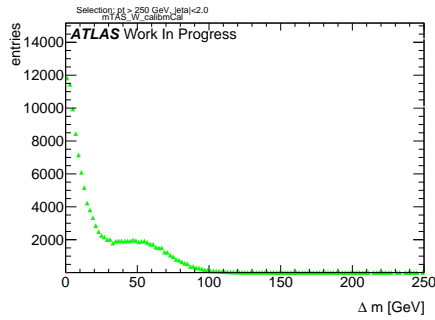


Figure H.51: $|m_{sub-jet} - m_{track-jet}|$ distribution, where sub-jet and track-jet are the closest

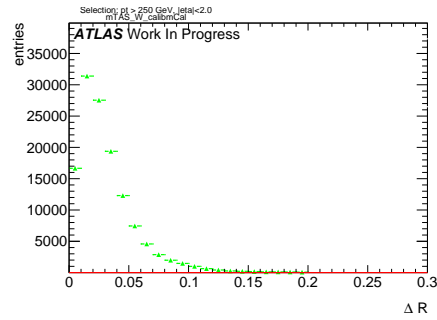


Figure H.54: $|R_{sub-jet} - R_{track-jet}|$ distribution, where sub-jet and track-jet are the closest

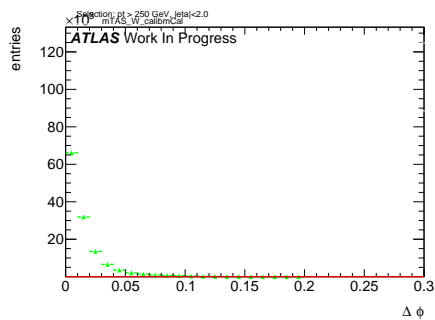


Figure H.52: $|\phi_{sub-jet} - \phi_{track-jet}|$ distribution, where sub-jet and track-jet are the closest

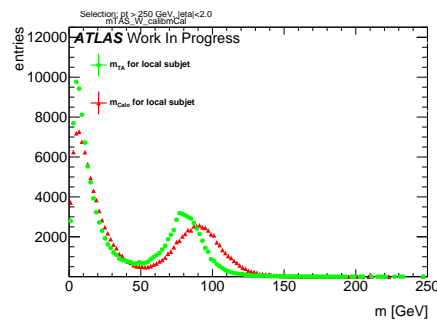


Figure H.55: Mass distribution of the sub-jet, calorimeter and track-assisted

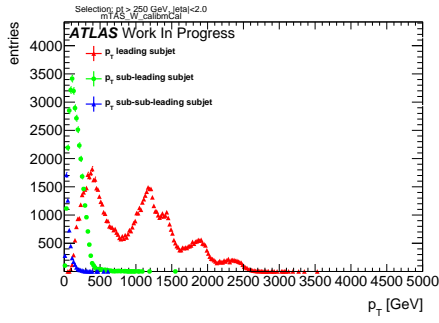


Figure H.56: p_T distribution for leading, sub-leading and sub-sub-leading sub-jets

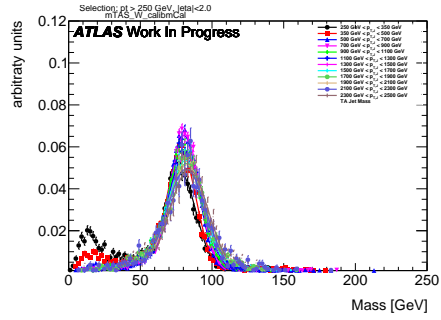


Figure H.59: m^{TAS} for p_T^J bin, superimposed

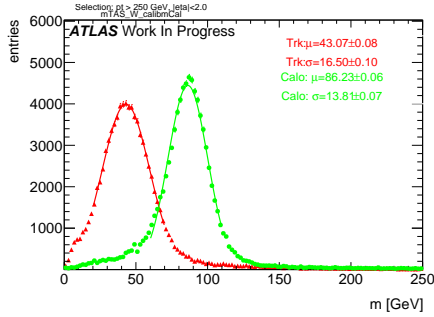


Figure H.57: Mass distribution for calorimeter and tracks associated to the large-R jet

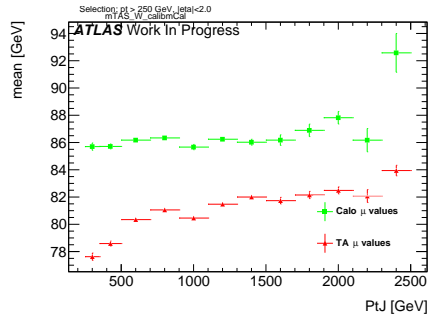


Figure H.60: μ from fit of the mass distribution vs bin of p_T^J

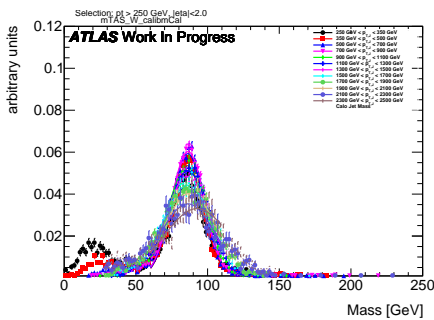


Figure H.58: m^{calo} for p_T^J bin, superimposed

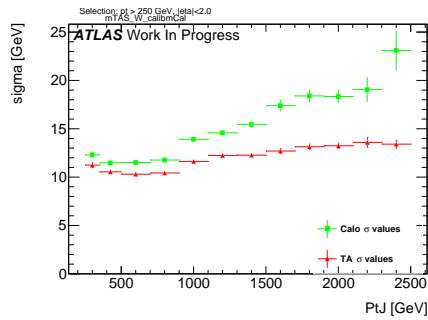


Figure H.61: σ from fit of the mass distribution vs bin of p_T^J

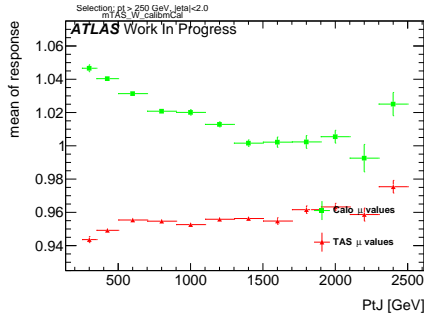


Figure H.62: μ from fit of the mass Response vs bin of p_T^J

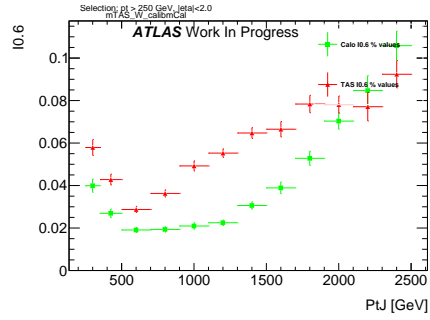


Figure H.65: Left integral normalized, $\int_0^{0.6}$ of the mass response, vs bin of p_T^J

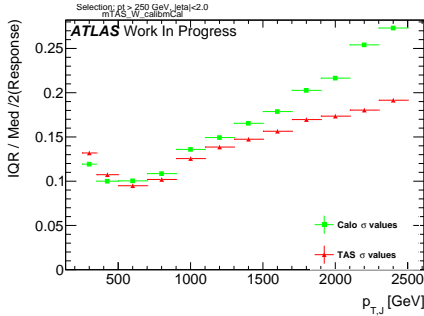


Figure H.63: σ from fit of the mass Response vs bin of p_T^J

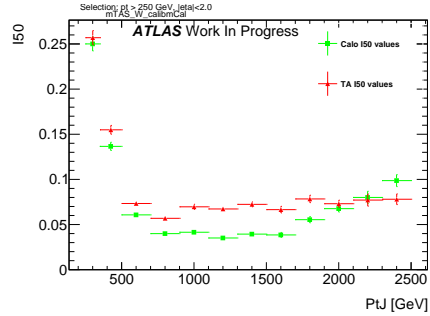


Figure H.66: $\int_0^{50 GeV}$ from fit of the mass distribution vs bin of p_T^J (normalized)

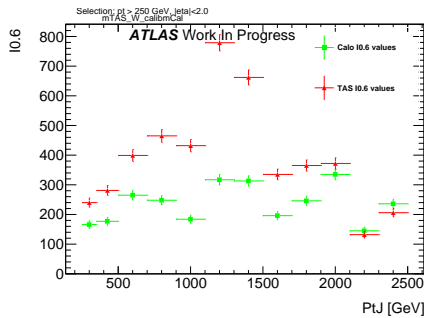


Figure H.64: Left integral, $\int_0^{0.6}$ of the mass response, vs bin of p_T^J

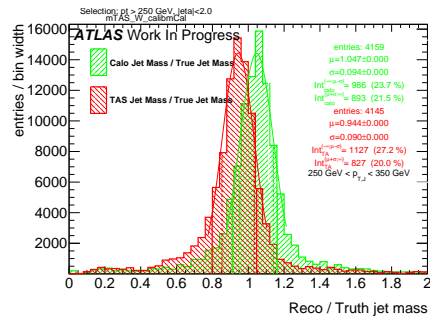


Figure H.67: Response in bin of p_T^J (indicated on plot)

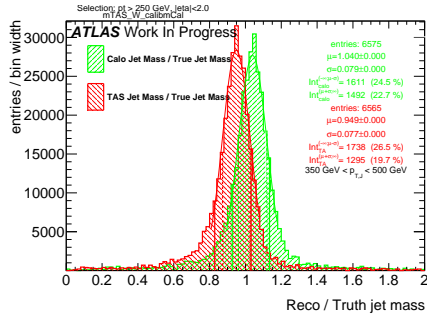


Figure H.68: Response in bin of p_T^J (indicated on plot)

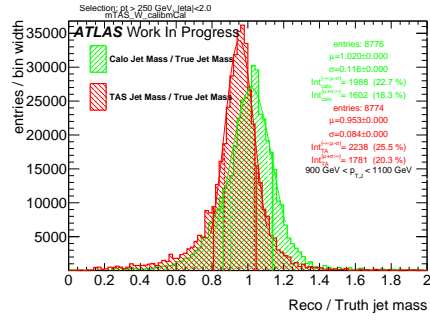


Figure H.71: Response in bin of p_T^J (indicated on plot)

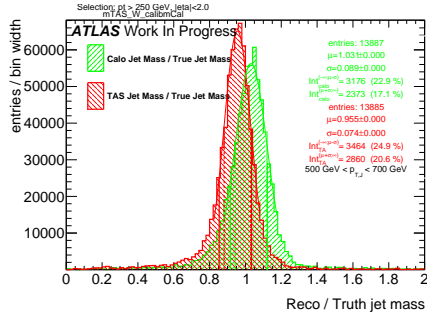


Figure H.69: Response in bin of p_T^J (indicated on plot)

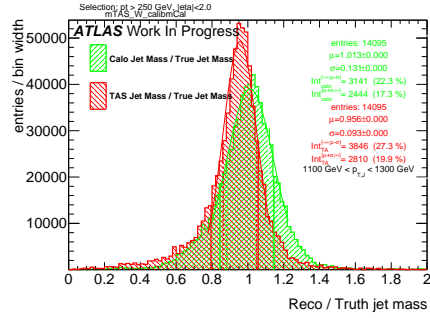


Figure H.72: Response in bin of p_T^J (indicated on plot)

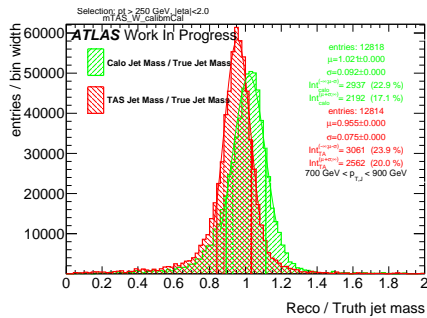


Figure H.70: Response in bin of p_T^J (indicated on plot)

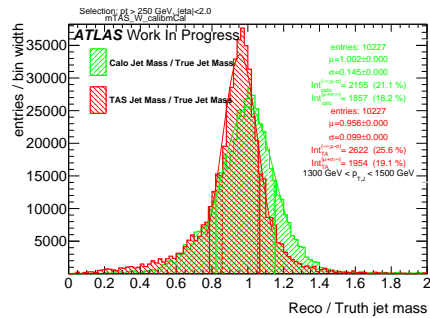


Figure H.73: Response in bin of p_T^J (indicated on plot)

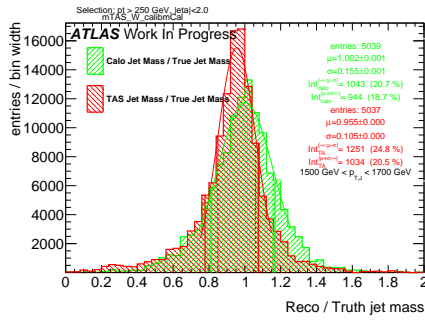


Figure H.74: Response in bin of p_T^J (indicated on plot)

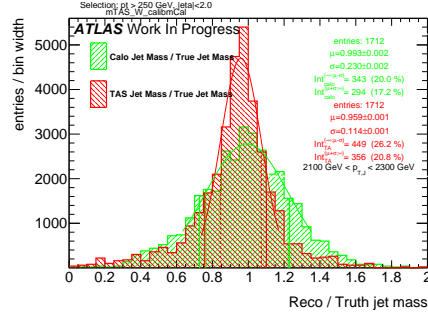


Figure H.77: Response in bin of p_T^J (indicated on plot)

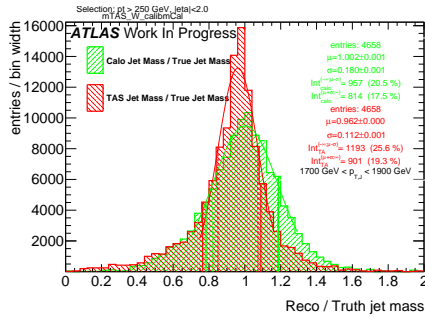


Figure H.75: Response in bin of p_T^J (indicated on plot)

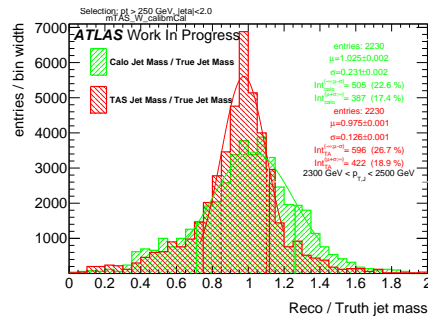


Figure H.78: Response in bin of p_T^J (indicated on plot)

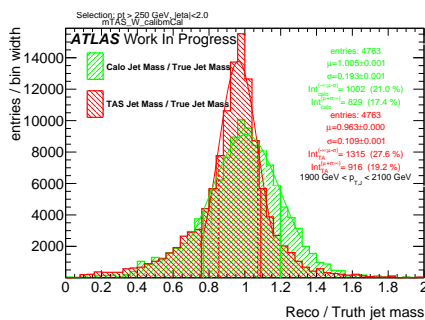


Figure H.76: Response in bin of p_T^J (indicated on plot)

H.2. m^{TAS} distributions, boosted tops

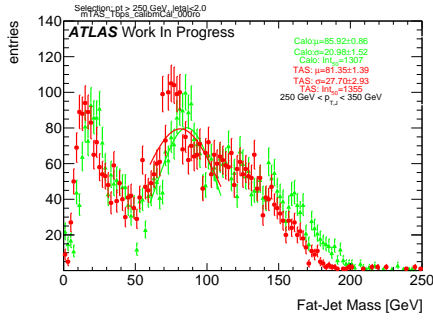


Figure H.79: m^{TAS} and m^{calo} for p_T^J bin (indicated on plot)

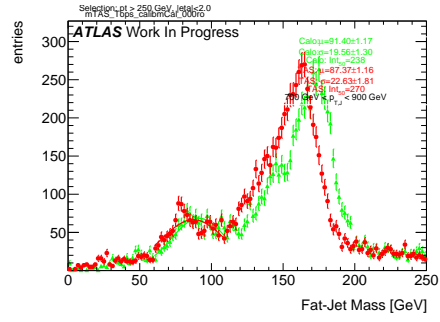


Figure H.82: m^{TAS} and m^{calo} for p_T^J bin (indicated on plot)

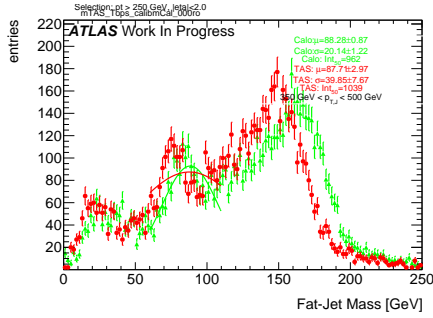


Figure H.80: m^{TAS} and m^{calo} for p_T^J bin (indicated on plot)

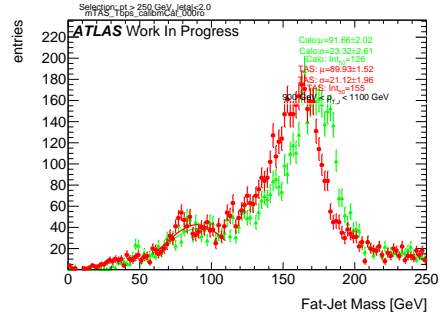


Figure H.83: m^{TAS} and m^{calo} for p_T^J bin (indicated on plot)

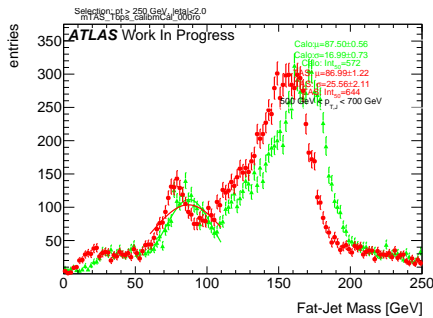


Figure H.81: m^{TAS} and m^{calo} for p_T^J bin (indicated on plot)

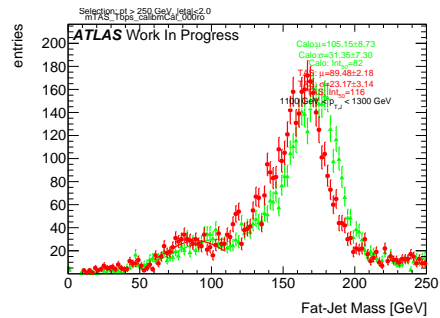


Figure H.84: m^{TAS} and m^{calo} for p_T^J bin (indicated on plot)

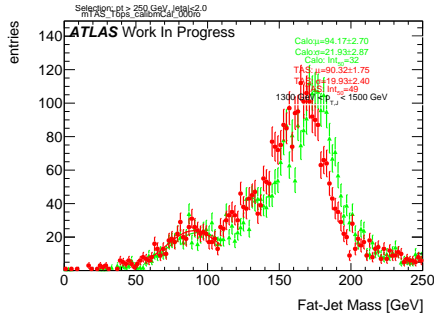


Figure H.85: m^{TAS} and m^{calo} for p_T^J bin (indicated on plot)

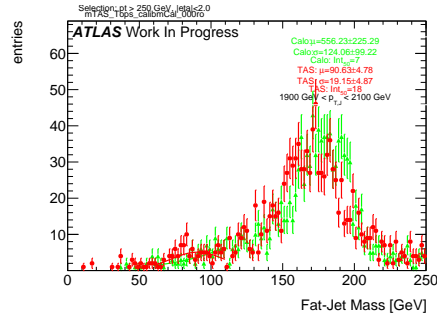


Figure H.88: m^{TAS} and m^{calo} for p_T^J bin (indicated on plot)

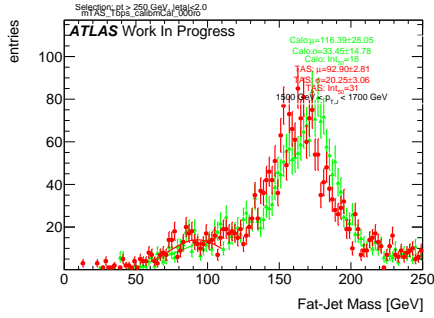


Figure H.86: m^{TAS} and m^{calo} for p_T^J bin (indicated on plot)

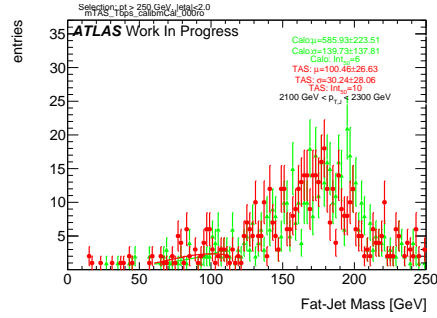


Figure H.89: m^{TAS} and m^{calo} for p_T^J bin (indicated on plot)

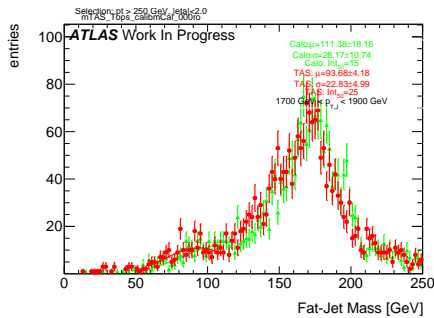


Figure H.87: m^{TAS} and m^{calo} for p_T^J bin (indicated on plot)

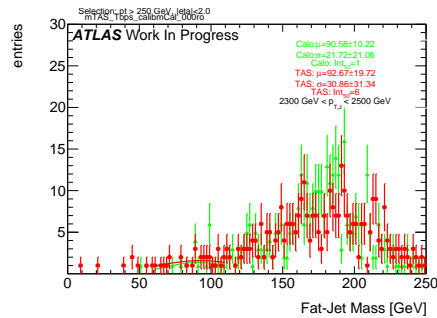


Figure H.90: m^{TAS} and m^{calo} for p_T^J bin (indicated on plot)

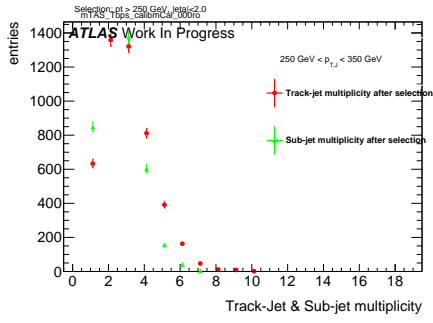


Figure H.91: Track-jet $R=0.2$ and sub-jet multiplicity for p_T^J bin (indicated on plot)

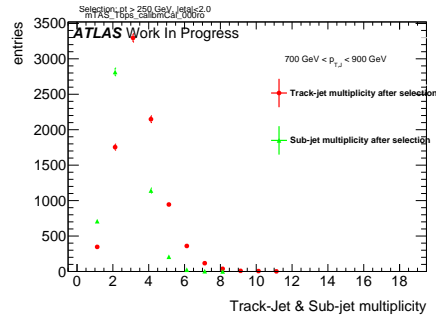


Figure H.94: Track-jet $R=0.2$ and sub-jet multiplicity for p_T^J bin (indicated on plot)

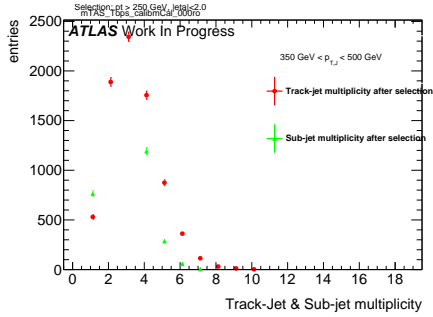


Figure H.92: Track-jet $R=0.2$ and sub-jet multiplicity for p_T^J bin (indicated on plot)

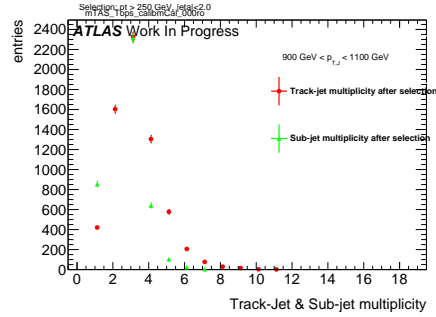


Figure H.95: Track-jet $R=0.2$ and sub-jet multiplicity for p_T^J bin (indicated on plot)

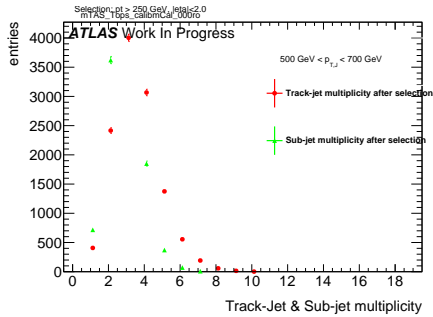


Figure H.93: Track-jet $R=0.2$ and sub-jet multiplicity for p_T^J bin (indicated on plot)

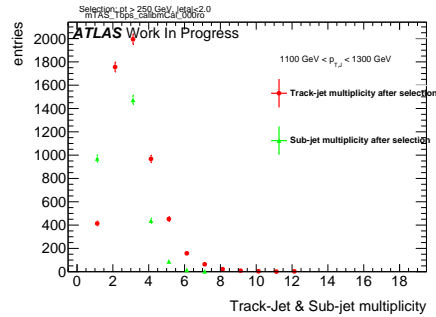


Figure H.96: Track-jet $R=0.2$ and sub-jet multiplicity for p_T^J bin (indicated on plot)

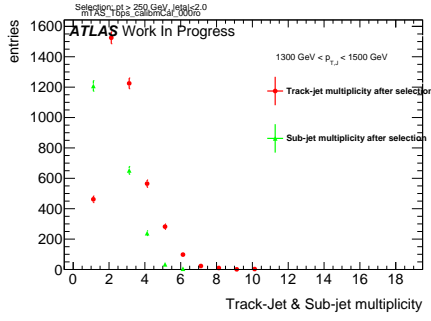


Figure H.97: Track-jet $R=0.2$ and sub-jet multiplicity for p_T^J bin (indicated on plot)

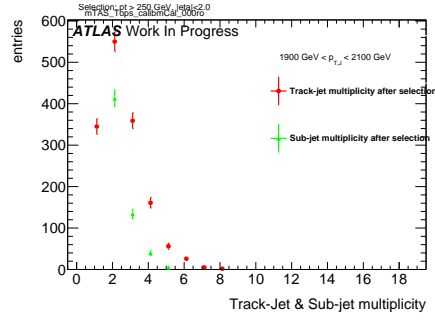


Figure H.100: Track-jet $R=0.2$ and sub-jet multiplicity for p_T^J bin (indicated on plot)

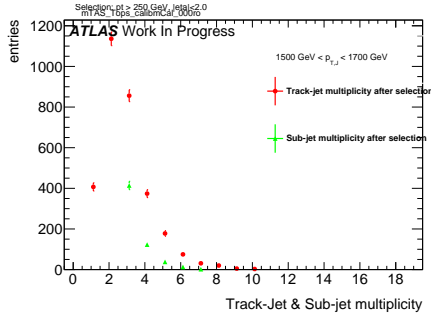


Figure H.98: Track-jet $R=0.2$ and sub-jet multiplicity for p_T^J bin (indicated on plot)

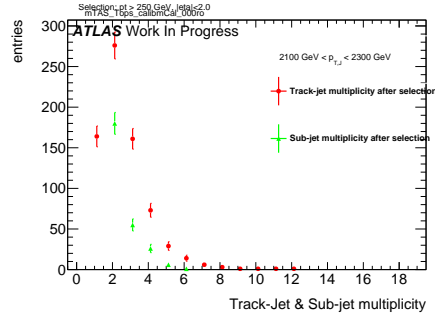


Figure H.101: Track-jet $R=0.2$ and sub-jet multiplicity for p_T^J bin (indicated on plot)

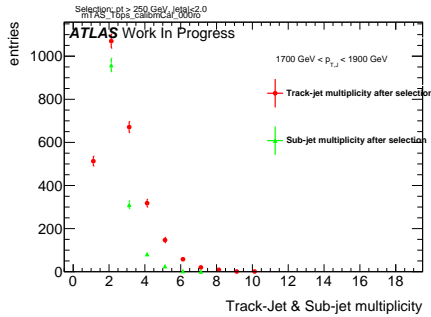


Figure H.99: Track-jet $R=0.2$ and sub-jet multiplicity for p_T^J bin (indicated on plot)

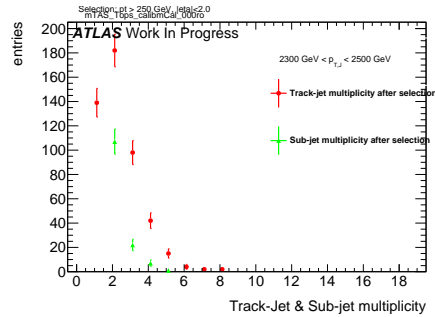


Figure H.102: Track-jet $R=0.2$ and sub-jet multiplicity for p_T^J bin (indicated on plot)

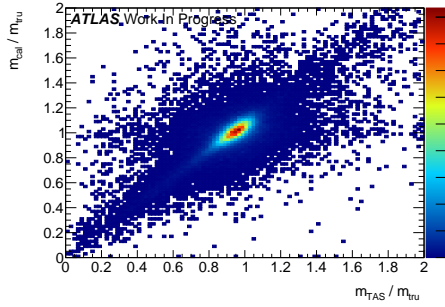


Figure H.103: Scatter plot m^{TAS} versus m^{calo} responses

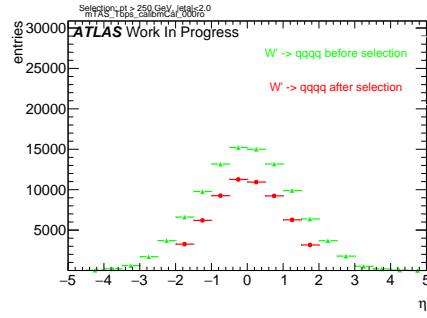


Figure H.106: η distribution of the large-R jet, before and after selection

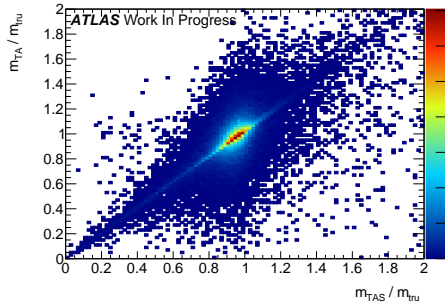


Figure H.104: Scatter plot m^{TAS} versus m^{TA} responses

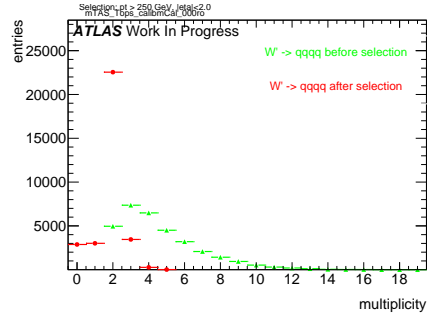


Figure H.107: large-R jet Multiplicity, before and after selection

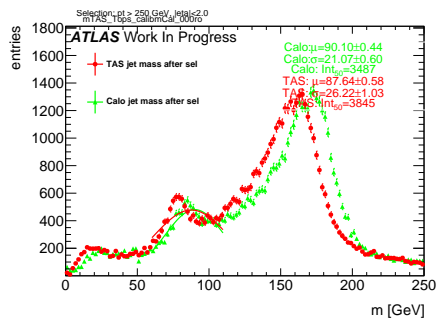


Figure H.105: m^{TAS} distribution in all the p_T bins

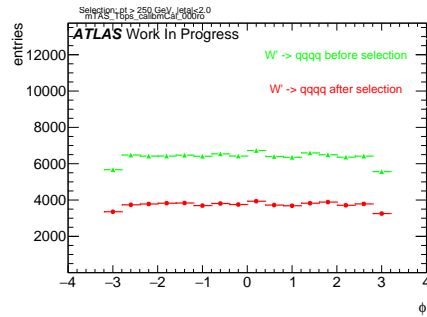


Figure H.108: ϕ distribution of the large-R jet, before and after selection

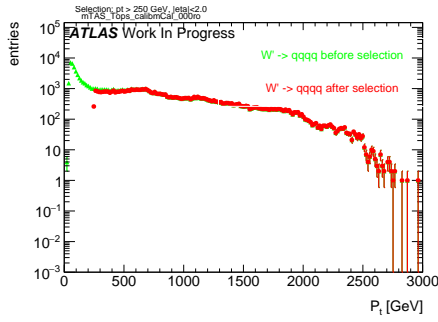


Figure H.109: p_T distribution of the large-R jet, before and after selection

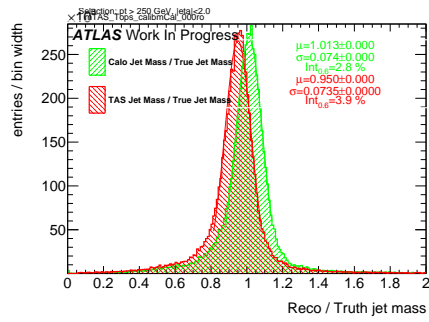


Figure H.112: Response m^{Reco}/m^{Truth} for all the p_T bins

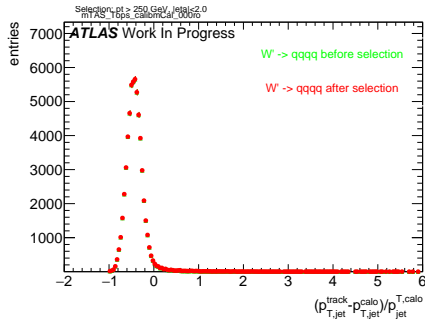


Figure H.110: p_T resolution: $\frac{p_{T,jet}^{track} - p_{T,jet}^{fat}}{p_{T,jet}^{fat}}$, before and after selection

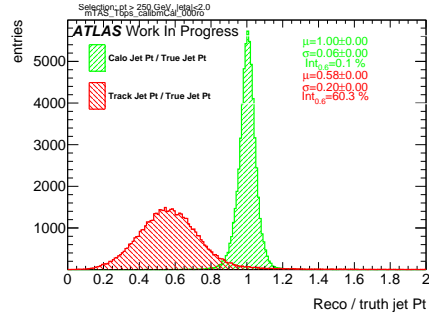


Figure H.113: Transverse momentum response p_T^{Reco}/p_T^{Truth} for calorimeter and tracks

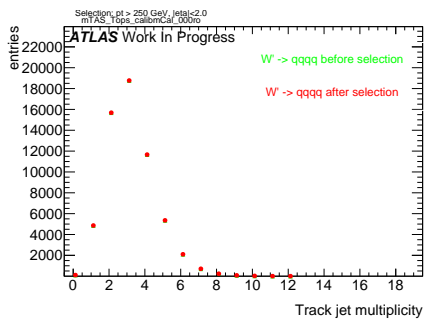


Figure H.111: Multiplicity of track-jets $R=0.2$ per large-R jet

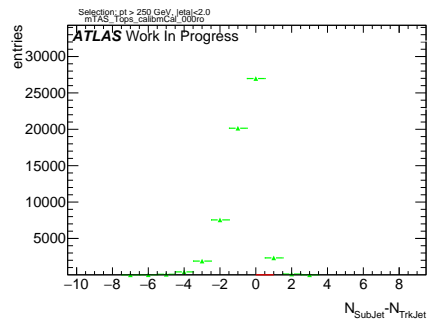


Figure H.114: sub-jet - track-jet Multiplicity

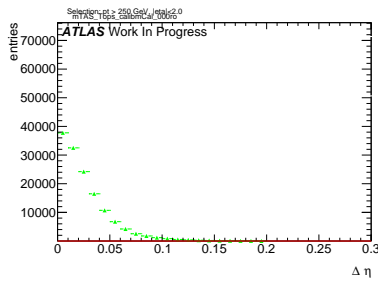


Figure H.115: $|\eta_{sub-jet} - \eta_{track-jet}|$ distribution, where sub-jet and track-jet are the closest

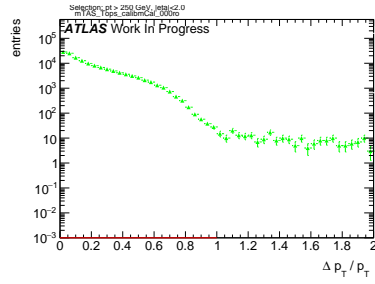


Figure H.118: $|p_{T,sub-jet} - p_{T,track-jet}|$ distribution, where sub-jet and track-jet are the closest

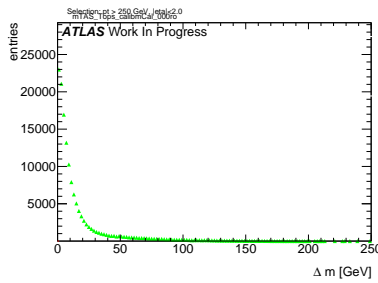


Figure H.116: $|m_{sub-jet} - m_{track-jet}|$ distribution, where sub-jet and track-jet are the closest

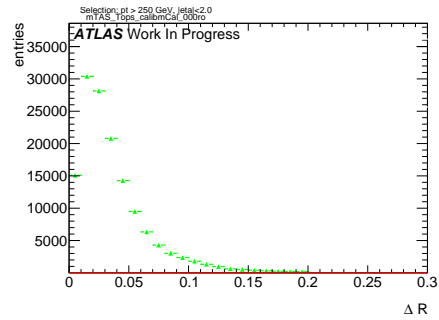


Figure H.119: $|R_{sub-jet} - R_{track-jet}|$ distribution, where sub-jet and track-jet are the closest

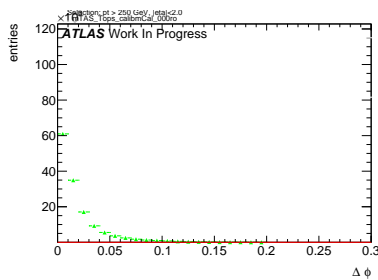


Figure H.117: $|\phi_{sub-jet} - \phi_{track-jet}|$ distribution, where sub-jet and track-jet are the closest

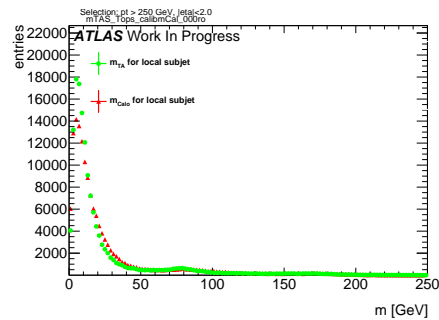


Figure H.120: Mass distribution of the sub-jet, calorimeter and track-assisted

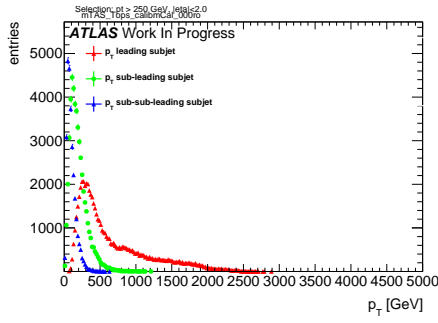


Figure H.121: p_T distribution for leading, sub-leading and sub-sub-leading sub-jets

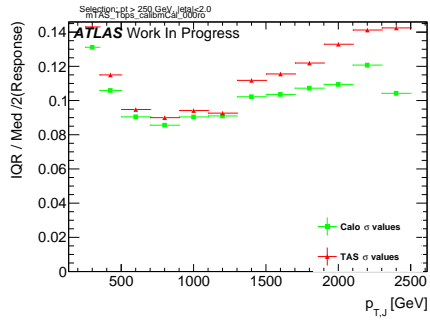


Figure H.124: σ from fit of the mass Response vs bin of p_T^J

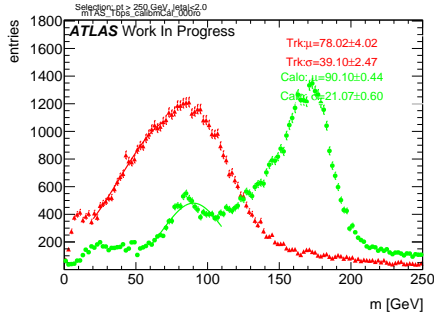


Figure H.122: Mass distribution for calorimeter and tracks associated to the large-R jet

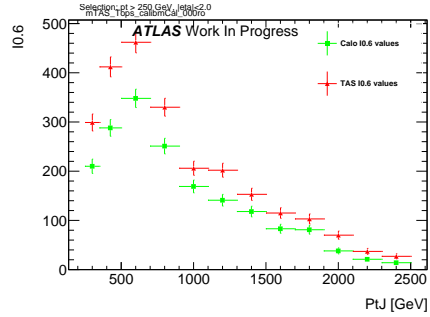


Figure H.125: Left integral, $\int_0^{0.6}$ of the mass response, vs bin of p_T^J

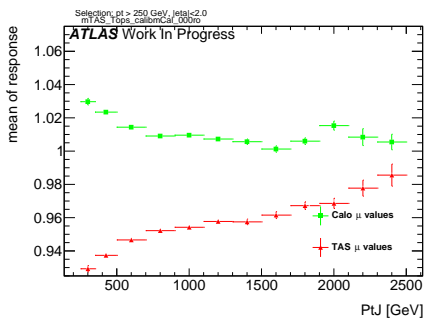


Figure H.123: μ from fit of the mass Response vs bin of p_T^J

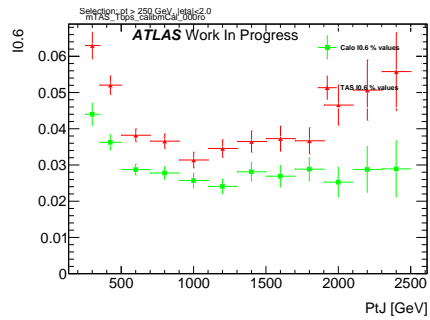


Figure H.126: Left integral normalized, $\int_0^{0.6}$ of the mass response, vs bin of p_T^J

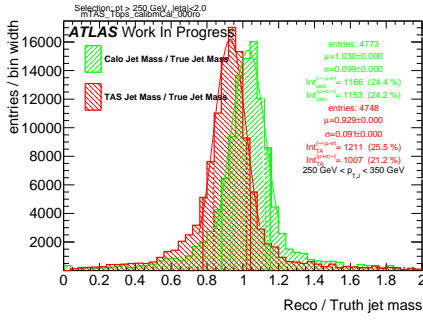


Figure H.127: Response in bin of p_T^J (indicated on plot)

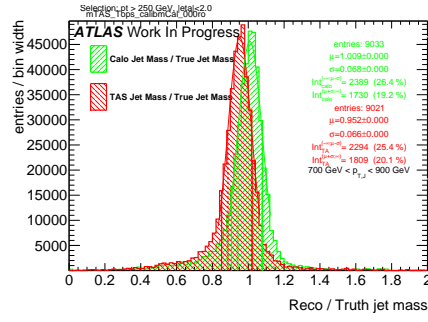


Figure H.130: Response in bin of p_T^J (indicated on plot)

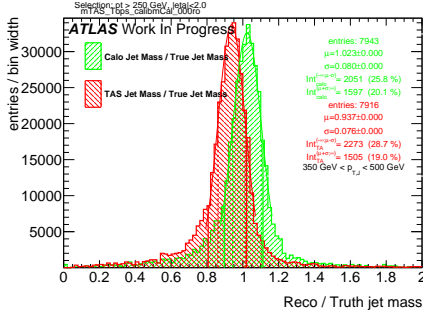


Figure H.128: Response in bin of p_T^J (indicated on plot)

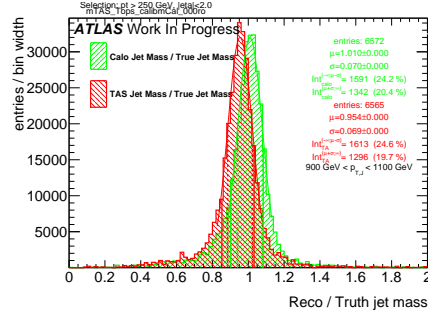


Figure H.131: Response in bin of p_T^J (indicated on plot)

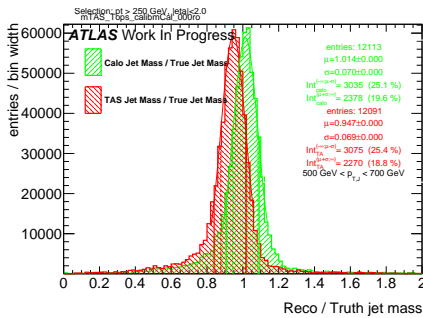


Figure H.129: Response in bin of p_T^J (indicated on plot)

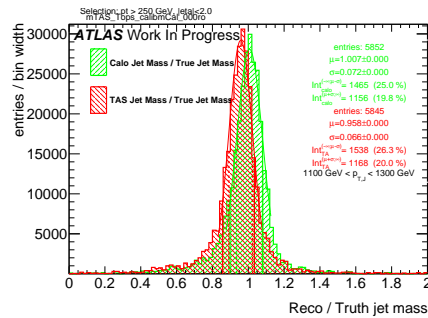


Figure H.132: Response in bin of p_T^J (indicated on plot)

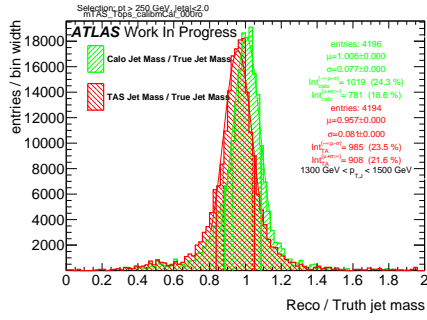


Figure H.133: Response in bin of p_T^J (indicated on plot)

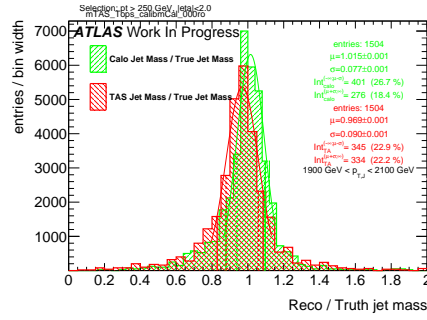


Figure H.136: Response in bin of p_T^J (indicated on plot)

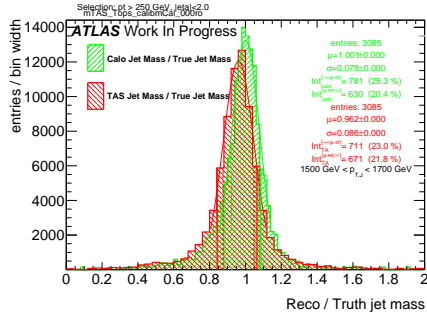


Figure H.134: Response in bin of p_T^J (indicated on plot)

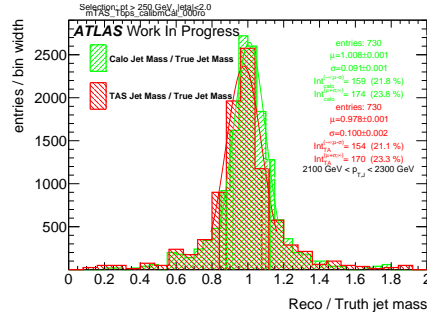


Figure H.137: Response in bin of p_T^J (indicated on plot)

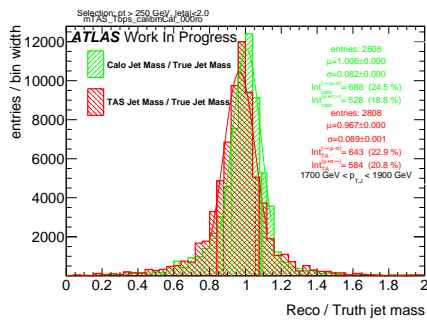


Figure H.135: Response in bin of p_T^J (indicated on plot)

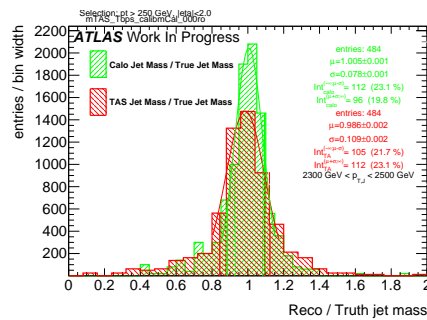


Figure H.138: Response in bin of p_T^J (indicated on plot)

H.3. m^{TAS} distributions, boosted higgs

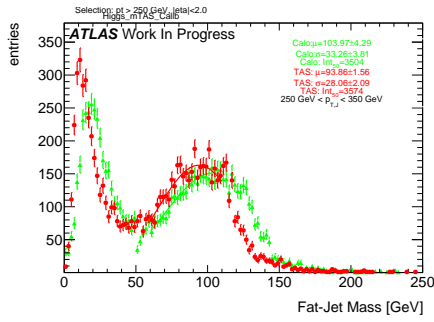


Figure H.139: m^{TAS} and m^{calo} for p_T^J bin (indicated on plot)

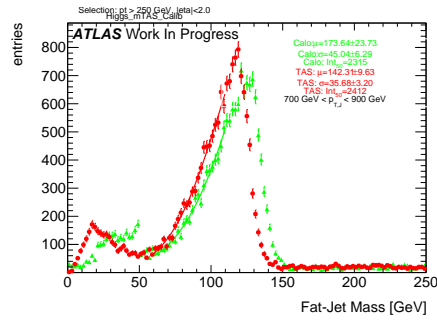


Figure H.142: m^{TAS} and m^{calo} for p_T^J bin (indicated on plot)

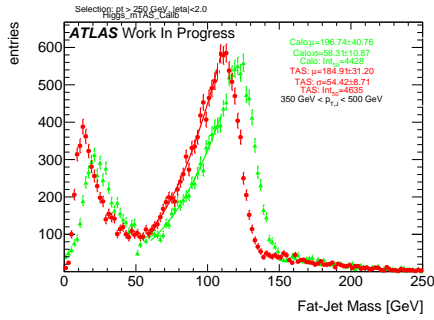


Figure H.140: m^{TAS} and m^{calo} for p_T^J bin (indicated on plot)

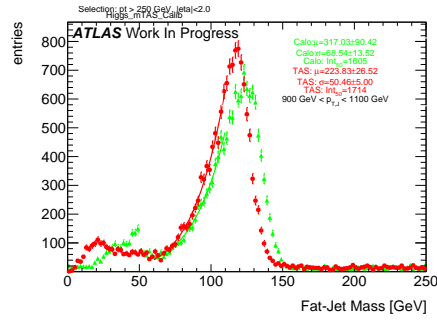


Figure H.143: m^{TAS} and m^{calo} for p_T^J bin (indicated on plot)

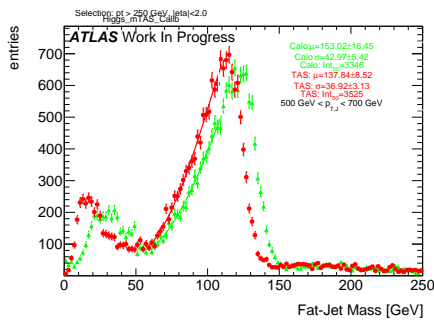


Figure H.141: m^{TAS} and m^{calo} for p_T^J bin (indicated on plot)

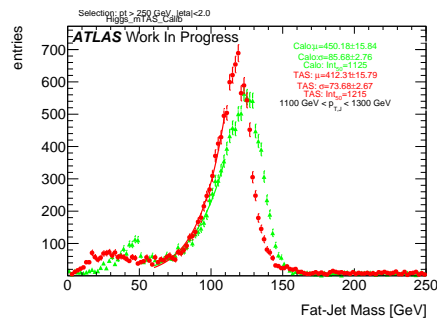


Figure H.144: m^{TAS} and m^{calo} for p_T^J bin (indicated on plot)

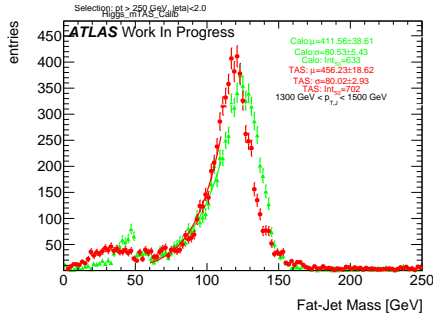


Figure H.145: m^{TAS} and m^{calo} for p_T^J bin (indicated on plot)

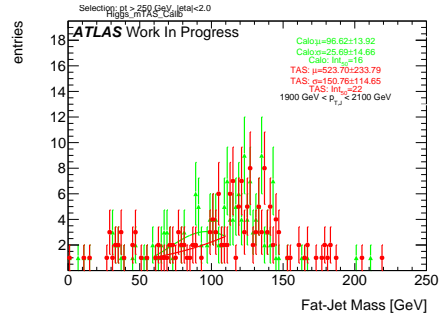


Figure H.148: m^{TAS} and m^{calo} for p_T^J bin (indicated on plot)

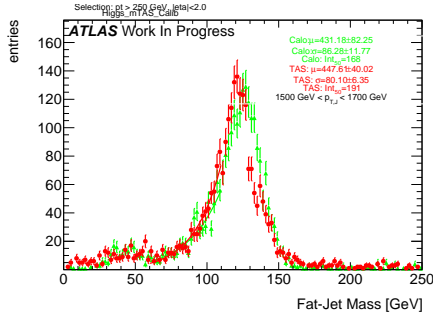


Figure H.146: m^{TAS} and m^{calo} for p_T^J bin (indicated on plot)

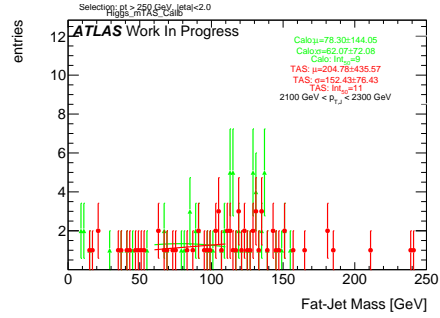


Figure H.149: m^{TAS} and m^{calo} for p_T^J bin (indicated on plot)

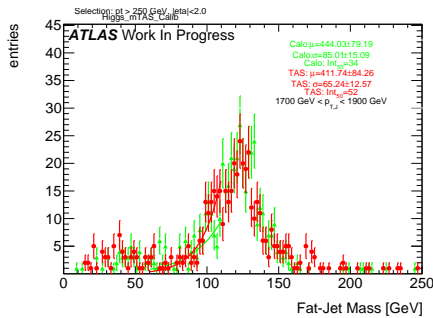


Figure H.147: m^{TAS} and m^{calo} for p_T^J bin (indicated on plot)

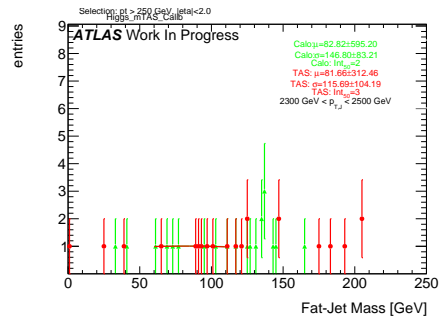


Figure H.150: m^{TAS} and m^{calo} for p_T^J bin (indicated on plot)

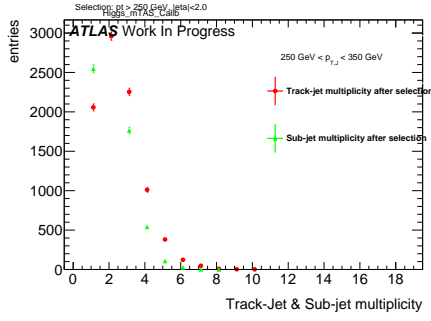


Figure H.151: Track-jet $R=0.2$ and sub-jet multiplicity for p_T^J bin (indicated on plot)

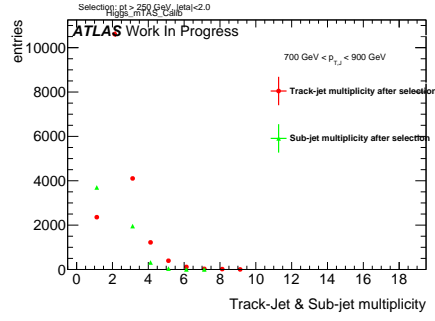


Figure H.154: Track-jet $R=0.2$ and sub-jet multiplicity for p_T^J bin (indicated on plot)

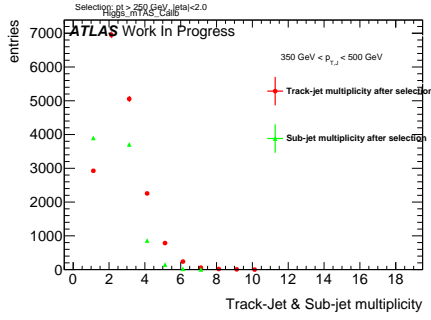


Figure H.152: Track-jet $R=0.2$ and sub-jet multiplicity for p_T^J bin (indicated on plot)

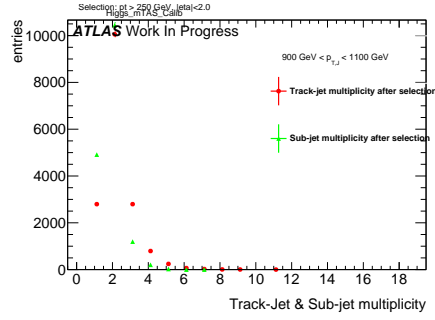


Figure H.155: Track-jet $R=0.2$ and sub-jet multiplicity for p_T^J bin (indicated on plot)

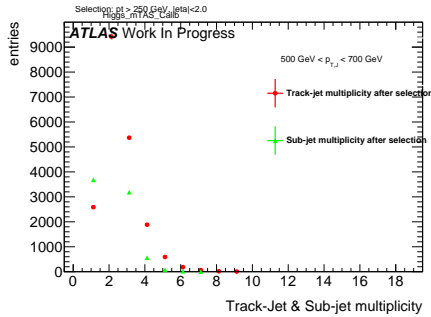


Figure H.153: Track-jet $R=0.2$ and sub-jet multiplicity for p_T^J bin (indicated on plot)

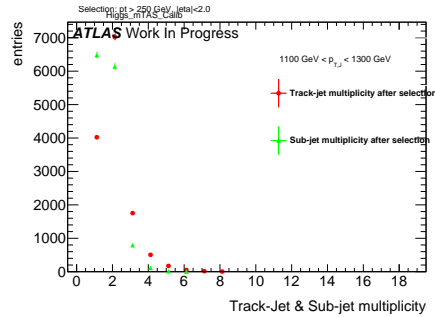


Figure H.156: Track-jet $R=0.2$ and sub-jet multiplicity for p_T^J bin (indicated on plot)

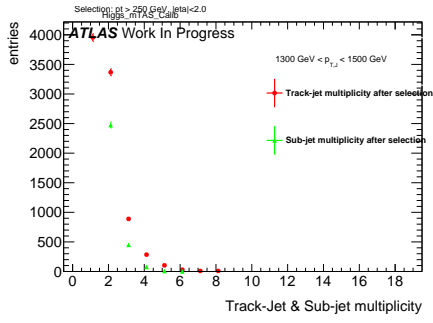


Figure H.157: Track-jet $R=0.2$ and sub-jet multiplicity for p_T^J bin (indicated on plot)

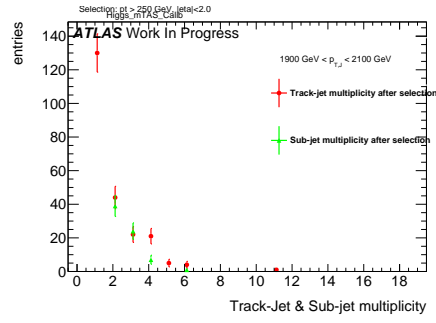


Figure H.160: Track-jet $R=0.2$ and sub-jet multiplicity for p_T^J bin (indicated on plot)

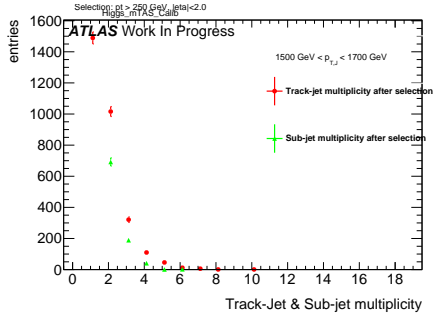


Figure H.158: Track-jet $R=0.2$ and sub-jet multiplicity for p_T^J bin (indicated on plot)

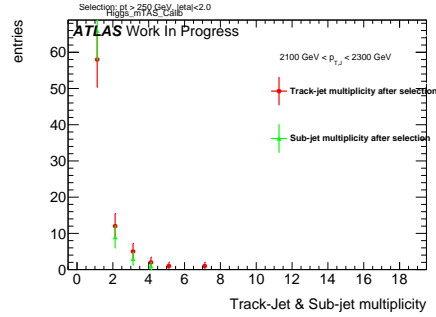


Figure H.161: Track-jet $R=0.2$ and sub-jet multiplicity for p_T^J bin (indicated on plot)

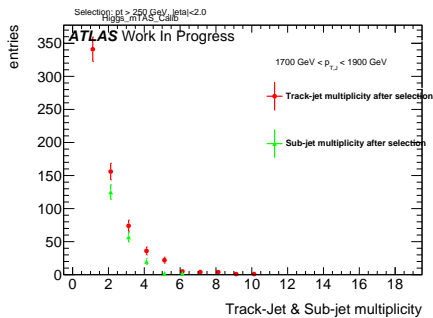


Figure H.159: Track-jet $R=0.2$ and sub-jet multiplicity for p_T^J bin (indicated on plot)

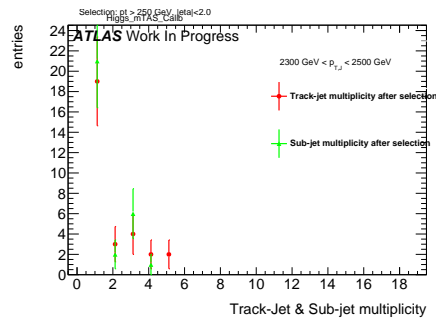


Figure H.162: Track-jet $R=0.2$ and sub-jet multiplicity for p_T^J bin (indicated on plot)

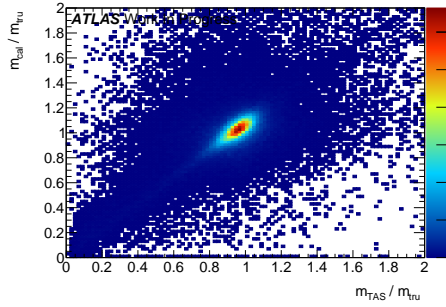


Figure H.163: Scatter plot m^{TAS} versus m^{calo} responses

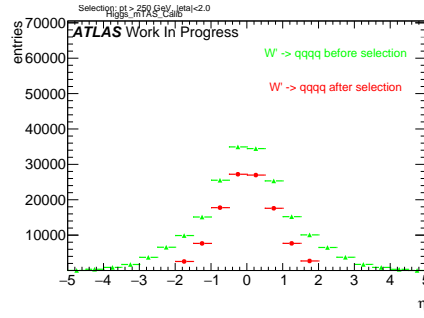


Figure H.166: η distribution of the large-R jet, before and after selection

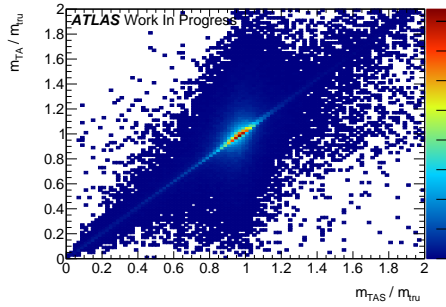


Figure H.164: Scatter plot m^{TAS} versus m^{TA} responses

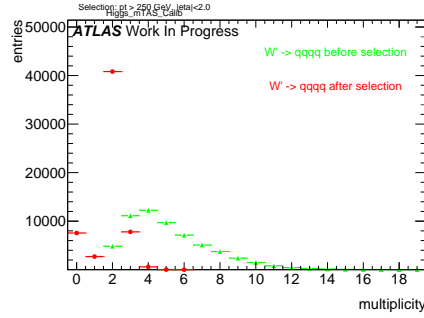


Figure H.167: large-R jet Multiplicity, before and after selection

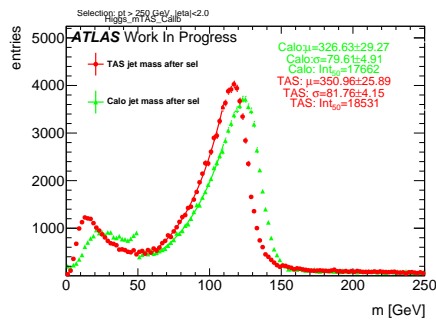


Figure H.165: m^{TAS} distribution in all the p_T bins

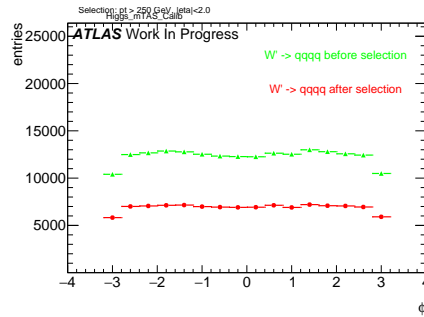


Figure H.168: ϕ distribution of the large-R jet, before and after selection

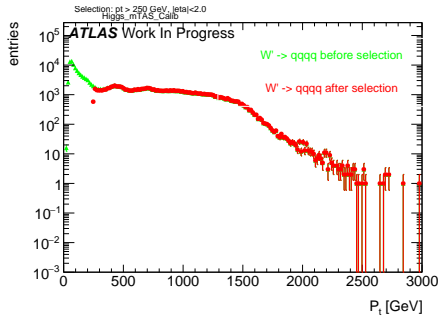


Figure H.169: p_T distribution of the large-R jet, before and after selection

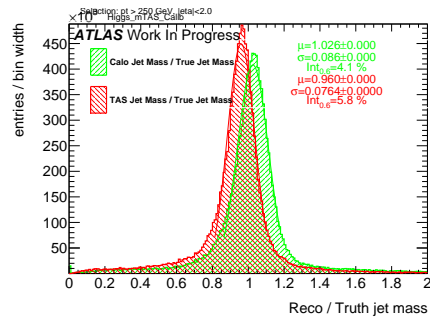


Figure H.172: Response m^{Reco}/m^{Truth} for all the p_T bins

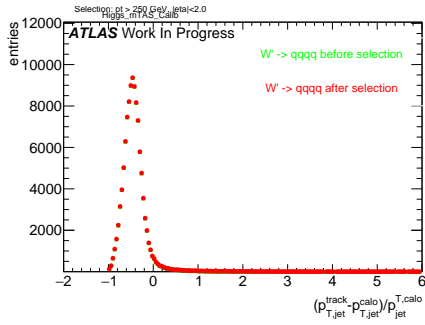


Figure H.170: p_T resolution: $\frac{p_{T,jet}^{track} - p_{T,jet}^{fat}}{p_{T,jet}^{calo}}$, before and after selection

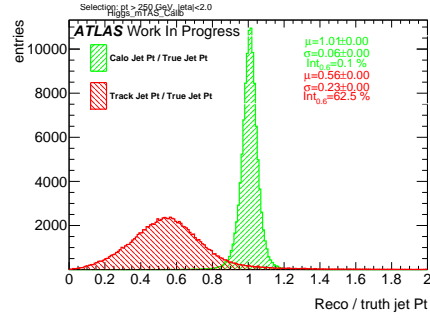


Figure H.173: Transverse momentum response p_T^{Reco}/p_T^{Truth} for calorimeter and tracks

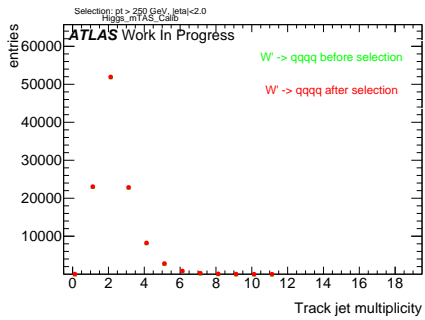


Figure H.171: Multiplicity of track-jets $R=0.2$ per large-R jet

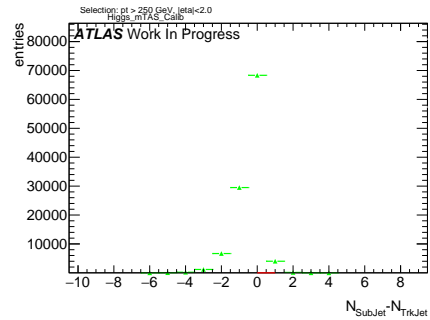


Figure H.174: sub-jet - track-jet Multiplicity

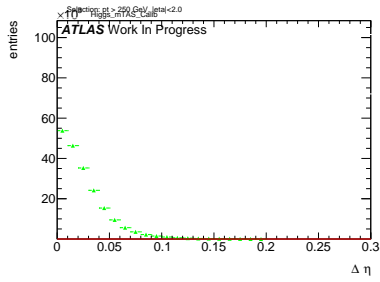


Figure H.175: $|\eta_{sub-jet} - \eta_{track-jet}|$ distribution, where sub-jet and track-jet are the closest

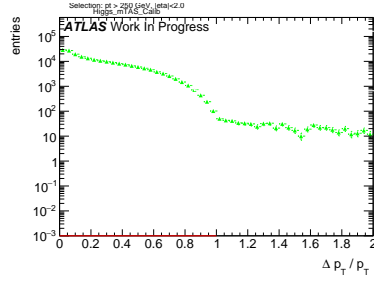


Figure H.178: $|p_{T,sub-jet} - p_{T,track-jet}|$ distribution, where sub-jet and track-jet are the closest

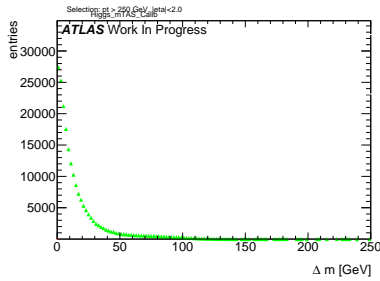


Figure H.176: $|m_{sub-jet} - m_{track-jet}|$ distribution, where sub-jet and track-jet are the closest

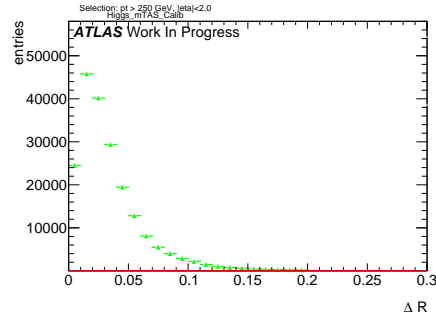


Figure H.179: $|R_{sub-jet} - R_{track-jet}|$ distribution, where sub-jet and track-jet are the closest

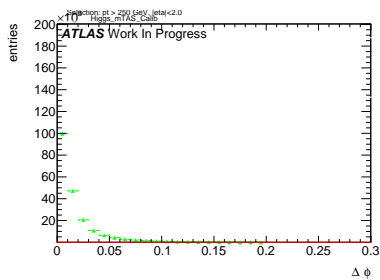


Figure H.177: $|\phi_{sub-jet} - \phi_{track-jet}|$ distribution, where sub-jet and track-jet are the closest

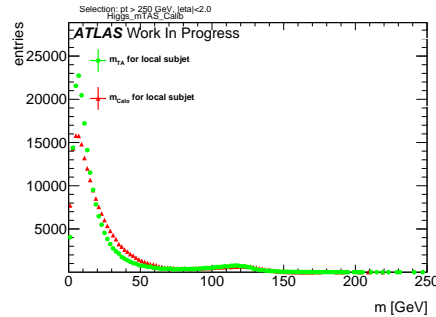


Figure H.180: Mass distribution of the sub-jet, calorimeter and track-assisted

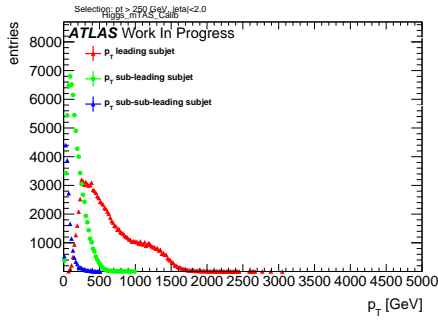


Figure H.181: p_T distribution for leading, sub-leading and sub-sub-leading sub-jets

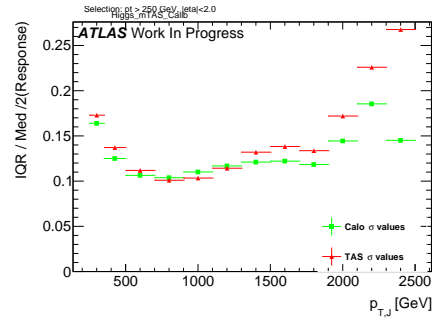


Figure H.184: σ from fit of the mass Response vs bin of p_T^J

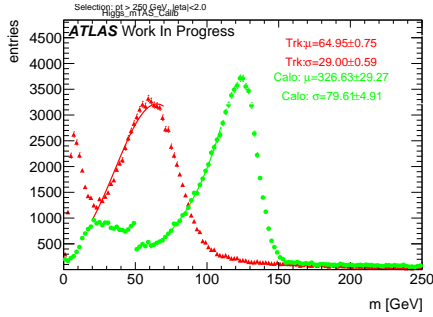


Figure H.182: Mass distribution for calorimeter and tracks associated to the large-R jet

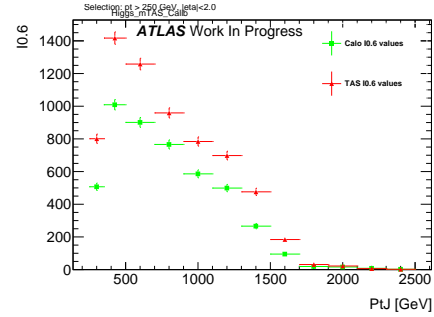


Figure H.185: Left integral, $\int_0^{0.6}$ of the mass response, vs bin of p_T^J

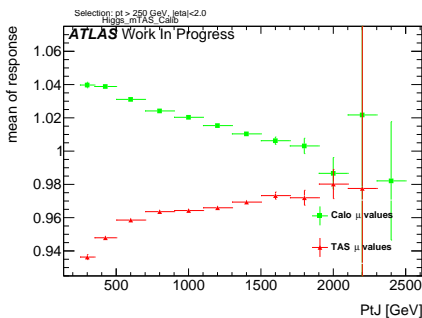


Figure H.183: μ from fit of the mass Response vs bin of p_T^J

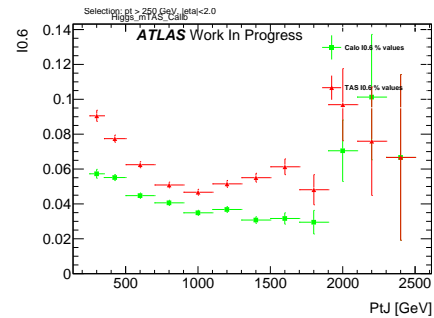


Figure H.186: Left integral normalized, $\int_0^{0.6}$ of the mass response, vs bin of p_T^J

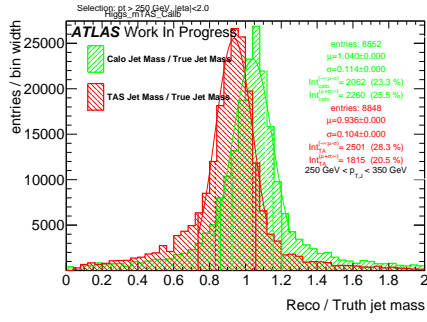


Figure H.187: Response in bin of p_T^J (indicated on plot)

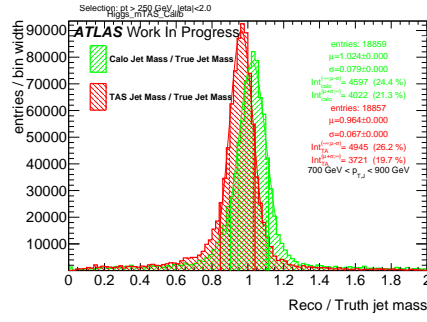


Figure H.190: Response in bin of p_T^J (indicated on plot)

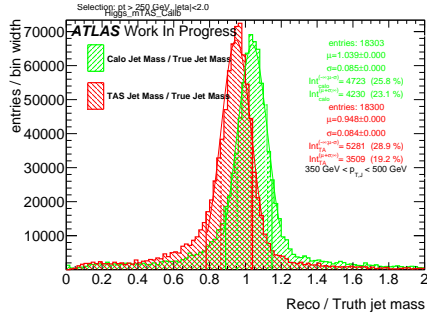


Figure H.188: Response in bin of p_T^J (indicated on plot)

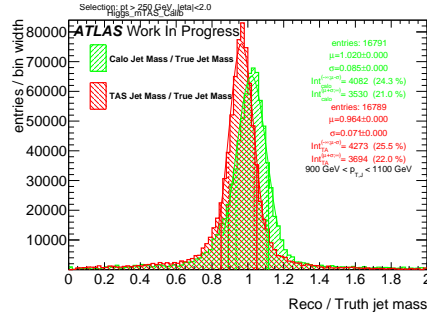


Figure H.191: Response in bin of p_T^J (indicated on plot)

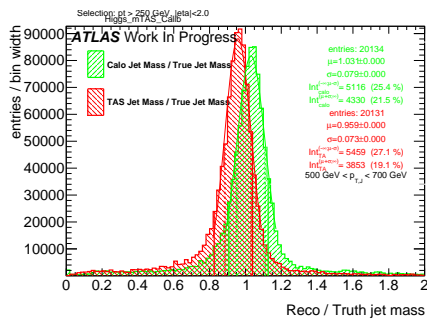


Figure H.189: Response in bin of p_T^J (indicated on plot)

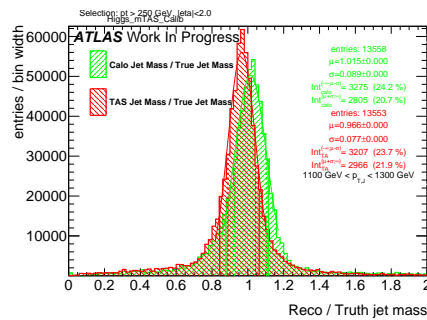


Figure H.192: Response in bin of p_T^J (indicated on plot)

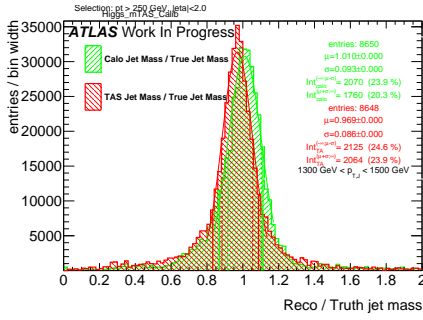


Figure H.193: Response in bin of p_T^J (indicated on plot)

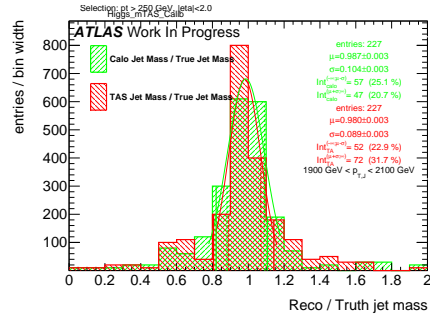


Figure H.196: Response in bin of p_T^J (indicated on plot)

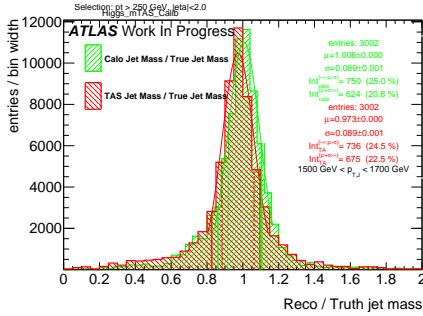


Figure H.194: Response in bin of p_T^J (indicated on plot)

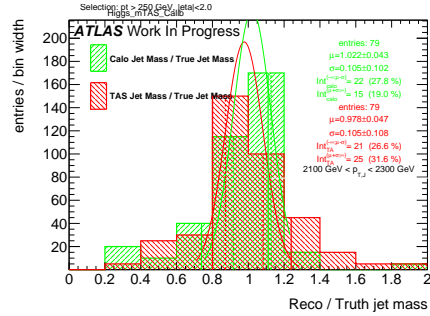


Figure H.197: Response in bin of p_T^J (indicated on plot)

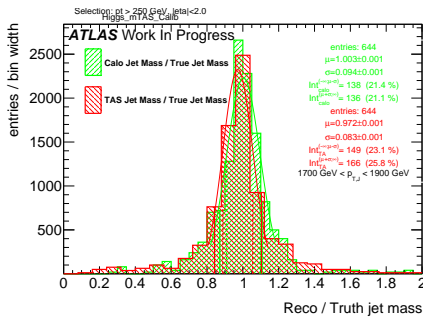


Figure H.195: Response in bin of p_T^J (indicated on plot)

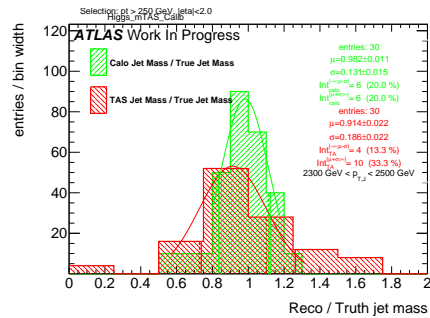


Figure H.198: Response in bin of p_T^J (indicated on plot)

H.4. m_{TAS}^{comb} response distributions, boosted W/Z

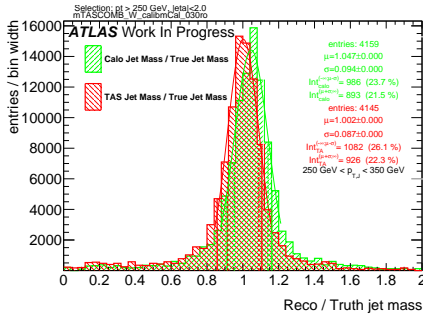


Figure H.199: Response in bin of p_T^J (indicated on plot)

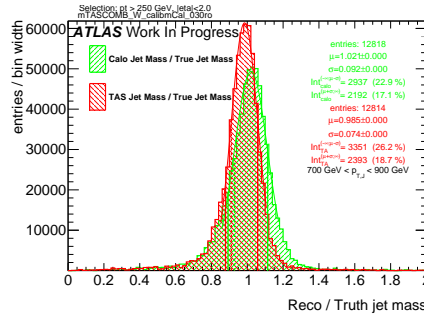


Figure H.202: Response in bin of p_T^J (indicated on plot)

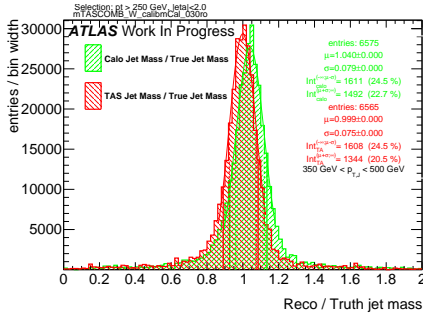


Figure H.200: Response in bin of p_T^J (indicated on plot)

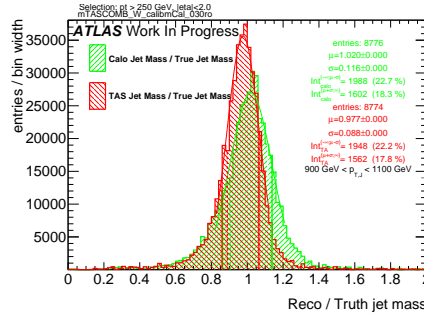


Figure H.203: Response in bin of p_T^J (indicated on plot)

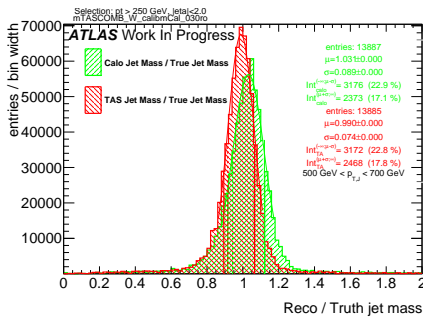


Figure H.201: Response in bin of p_T^J (indicated on plot)

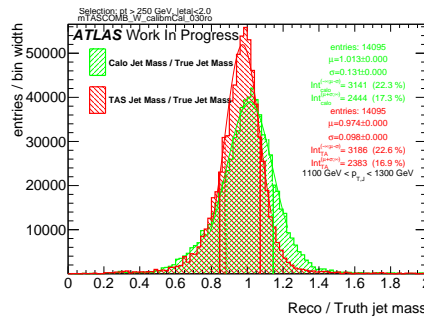


Figure H.204: Response in bin of p_T^J (indicated on plot)

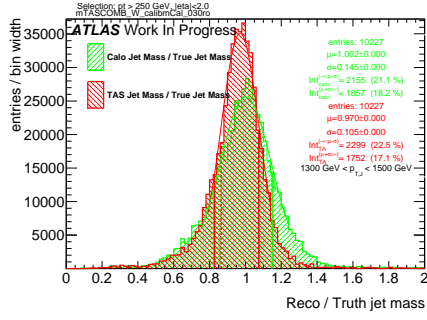


Figure H.205: Response in bin of p_T^J (indicated on plot)

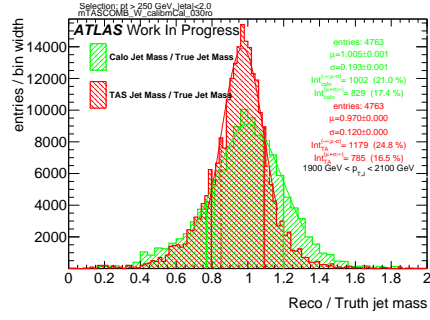


Figure H.208: Response in bin of p_T^J (indicated on plot)

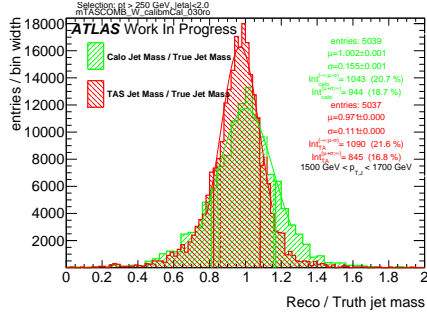


Figure H.206: Response in bin of p_T^J (indicated on plot)

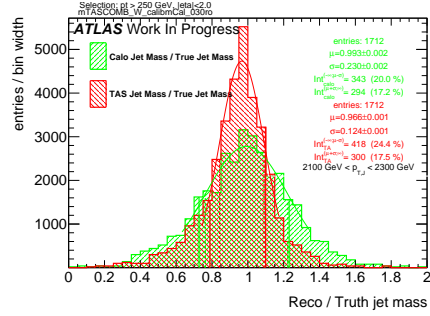


Figure H.209: Response in bin of p_T^J (indicated on plot)

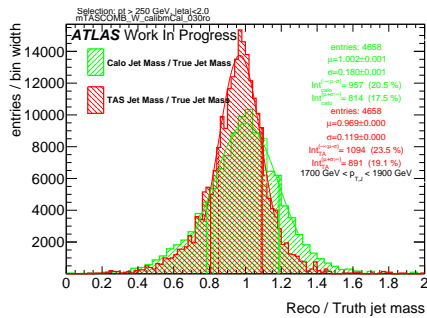


Figure H.207: Response in bin of p_T^J (indicated on plot)

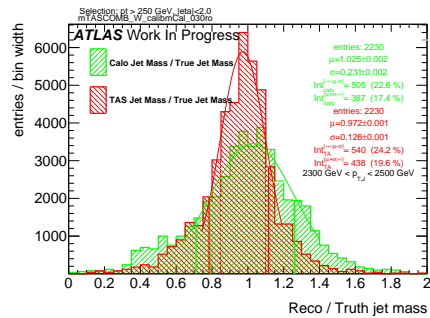


Figure H.210: Response in bin of p_T^J (indicated on plot)

H.5. m_{TAS}^{comb} response distributions, boosted tops

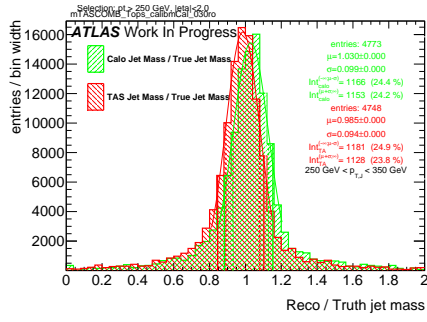


Figure H.211: Response in bin of p_T^J (indicated on plot)

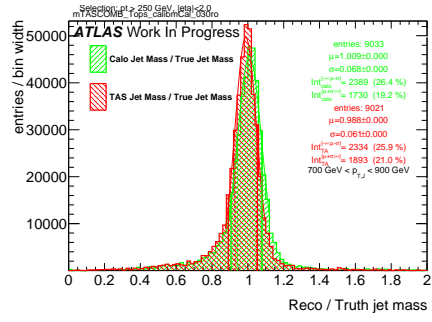


Figure H.214: Response in bin of p_T^J (indicated on plot)

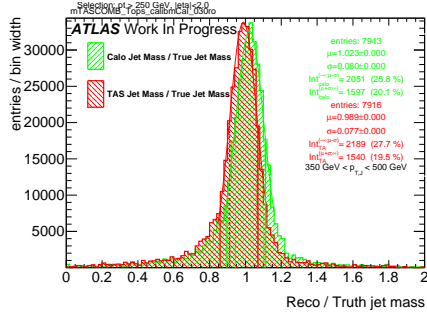


Figure H.212: Response in bin of p_T^J (indicated on plot)

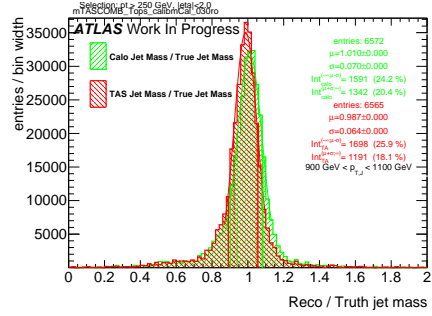


Figure H.215: Response in bin of p_T^J (indicated on plot)

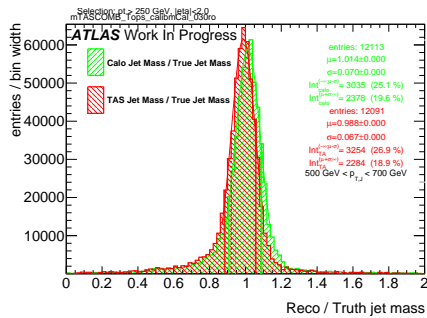


Figure H.213: Response in bin of p_T^J (indicated on plot)

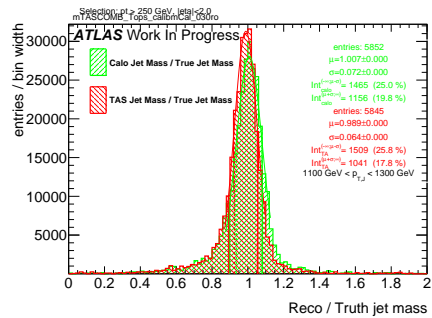


Figure H.216: Response in bin of p_T^J (indicated on plot)

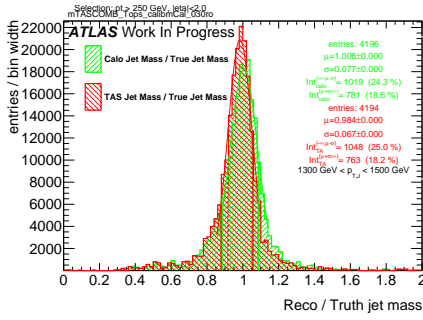


Figure H.217: Response in bin of p_T^J (indicated on plot)

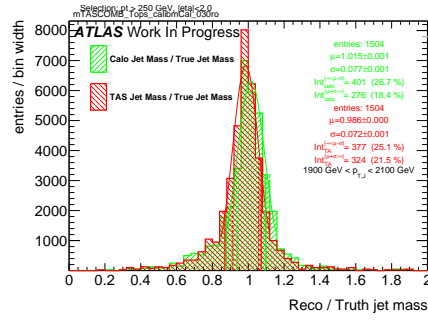


Figure H.220: Response in bin of p_T^J (indicated on plot)

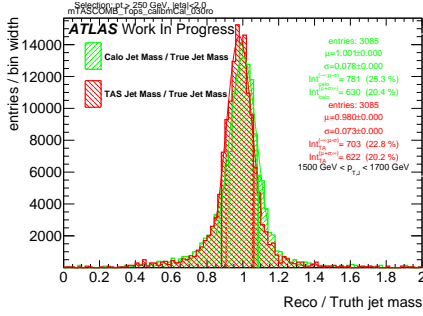


Figure H.218: Response in bin of p_T^J (indicated on plot)

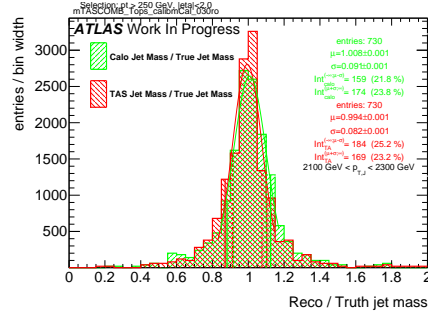


Figure H.221: Response in bin of p_T^J (indicated on plot)

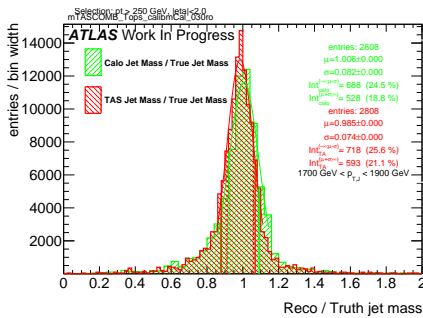


Figure H.219: Response in bin of p_T^J (indicated on plot)

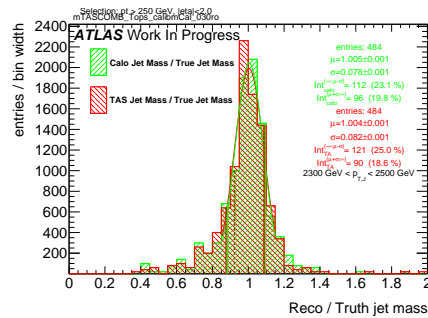


Figure H.222: Response in bin of p_T^J (indicated on plot)

H.6. m_{TAS}^{comb} response distributions, Higgs

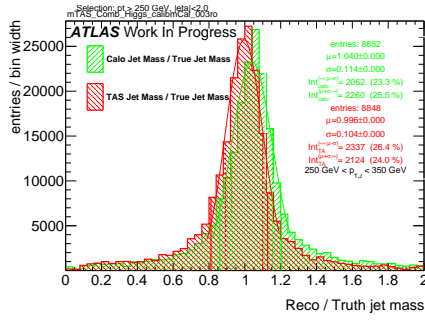


Figure H.223: Response in bin of p_T^J (indicated on plot)

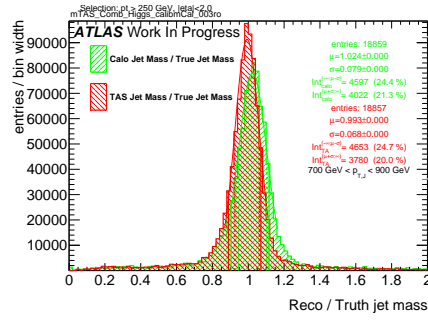


Figure H.226: Response in bin of p_T^J (indicated on plot)

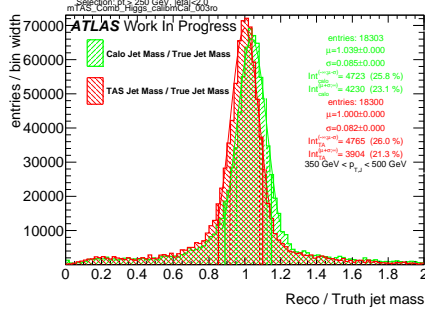


Figure H.224: Response in bin of p_T^J (indicated on plot)

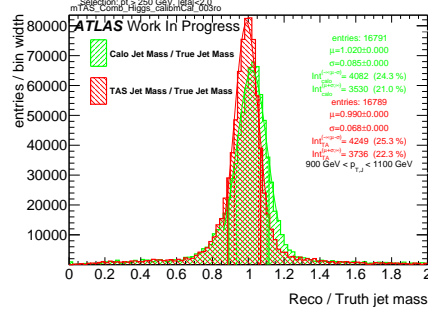


Figure H.227: Response in bin of p_T^J (indicated on plot)

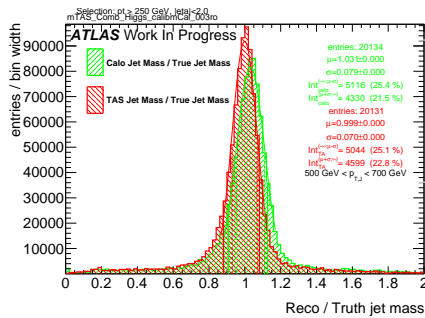


Figure H.225: Response in bin of p_T^J (indicated on plot)

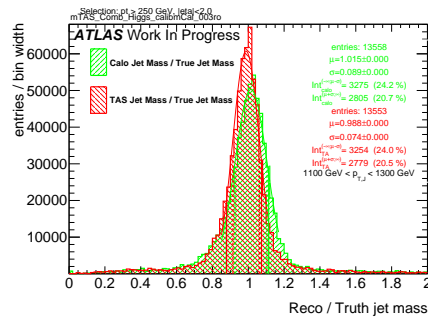


Figure H.228: Response in bin of p_T^J (indicated on plot)

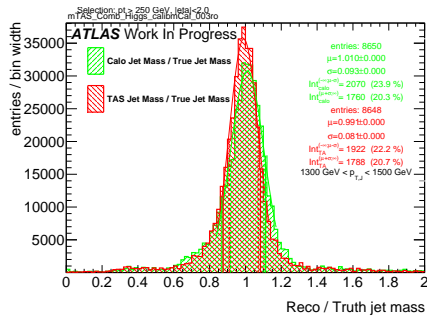


Figure H.229: Response in bin of p_T^J (indicated on plot)

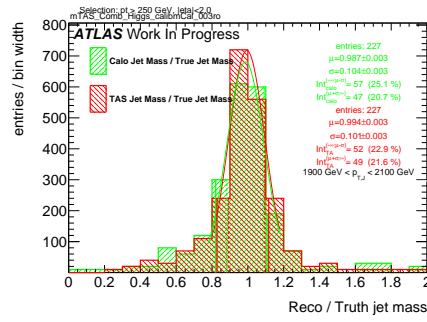


Figure H.232: Response in bin of p_T^J (indicated on plot)

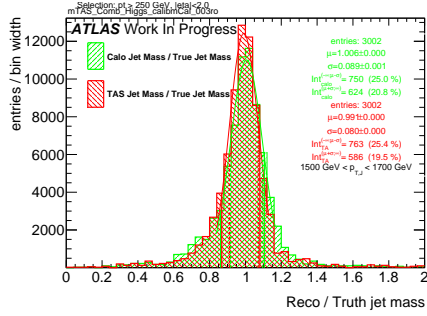


Figure H.230: Response in bin of p_T^J (indicated on plot)

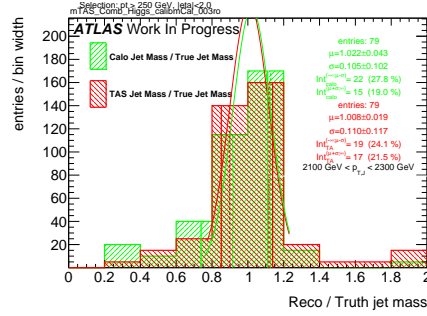


Figure H.233: Response in bin of p_T^J (indicated on plot)

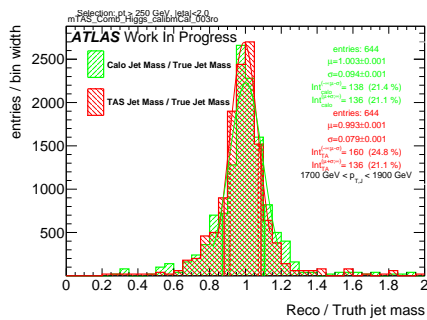


Figure H.231: Response in bin of p_T^J (indicated on plot)

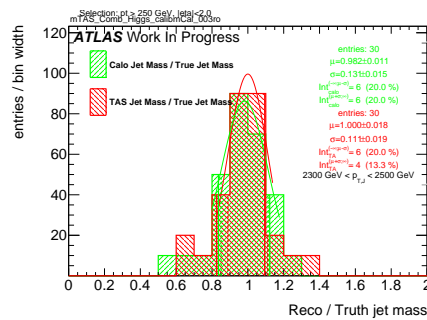


Figure H.234: Response in bin of p_T^J (indicated on plot)

I. Erklärung:

Ich versichere, dass ich diese Arbeit selbstständig verfasst habe und keine anderen als die angegebenen Quellen und Hilfsmittel benutzt habe.

Heidelberg, den 15.11.2016

.....